



ΕΘΝΙΚΟ ΜΕΤΣΟΒΙΟ ΠΟΛΥΤΕΧΝΕΙΟ

Εργαστήριο Ατμοκινητήρων & Λεβήτων

Τομέας Θερμότητας της Σχολής Μηχανολόγων Μηχανικών

ΔΙΠΛΩΜΑΤΙΚΗ ΕΡΓΑΣΙΑ

*Ενεργειακή, εξεργειακή και οικονομική
μελέτη συστήματος σύζευξης
φωτοβολταϊκών/θερμικών συλλεκτών –
οργανικού κύκλου Rankine (ORC)*

*Energetic, exergetic and economic analysis of
a coupled photovoltaic/thermal – Organic
Rankine Cycle (ORC) system*

Του Φοιτητή

Ρέππα Αποστόλου

Επιβλέπων

*Καρέλλας Σωτήριος, Αναπληρωτής Καθηγητής,
Σχολή Μηχανολόγων Μηχανικών, ΕΜΠ*

Abstract

Since the industrial revolution, the energy demands of society have grown rapidly. Due to the depletion of the fossil fuel reserves combined with the environmental issues arising from their consumption, innovative sustainable technologies have been proposed utilizing renewable forms of energy. Towards this trend, the coupling of photovoltaic/thermal (PVT) collectors with an Organic Rankine Cycle (ORC) emerges as a promising solution with zero CO_2 emissions.

PVT collectors have been studied extensively as a method of increasing the efficiency of the PV modules by reducing their cells' temperature and producing heat for further use. An innovative approach is the utilization of this energy content as the heat input of an ORC. In this thesis, this concept is implemented for various working fluids in 5 different Mediterranean locations. The modeling of the PV and thermal collectors and the solar storage tank are prerequisites for the coupling of the system. The on-design simulation of the ORC includes the sizing of the evaporator, the expander, the generator, the condenser, the pump and the motor for each examined working fluid. The total cost of the ORC is calculated after the completion of the sizing of its components. Since, the heat input of the cycle derives from varying solar radiation, the computation of the cycle's performance in off-design conditions is essential. The annual electricity production by the coupling of the PVT-ORC system is then calculated for a wide range of PVT collectors' surface as well as solar storage tank's volume capacity as part of the system's optimization.

In all locations, R152a is proven to be the most efficient and economically viable choice as the working fluid of the ORC, with a net electric efficiency of 6.931% in on-design conditions. The most viable combination is the maximization of the collectors' surface and a small solar storage tank. In the city of Athens, with R152a as the working fluid, the lowest Levelized Cost of Energy is equal to 0.153 €/kWh, the highest Net Present Value is equal to 2244.22 € and the minimum Payback Period is equal to 17.05 years.

Περίληψη

Μετά την εποχή της βιομηχανικής επανάστασης, οι ενεργειακές ανάγκες της κοινωνίας έχουν αναπτυχθεί δραματικά. Εξαιτίας της ελάττωσης των αποθεμάτων των ορυκτών καυσίμων σε συνδυασμό με τα περιβαλλοντικά προβλήματα που εγείρονται από την κατανάλωση τους, καινοτόμες βιώσιμες τεχνολογίες έχουν προταθεί, οι οποίες αξιοποιούν ανανεώσιμες μορφές ενέργειας. Προς αυτή την κατεύθυνση, η σύζευξη φωτοβολταϊκών/θερμικών (PVT) συλλεκτών με έναν Οργανικό Κύκλο Rankine (ORC) αναδύεται ως μία υποσχόμενη λύση μηδενικών εκπομπών CO_2 .

Οι PVT συλλέκτες έχουν μελετηθεί εκτενώς ως μία μέθοδος αύξησης του βαθμού απόδοσης των φωτοβολταϊκών μειώνοντας τη θερμοκρασία των κελιών τους και παραγωγής θερμότητας για περαιτέρω χρήση. Μια καινοτόμος προσέγγιση είναι η αξιοποίηση αυτού του ενεργειακού περιεχομένου ως θερμότητα εισόδου ενός ORC. Σε αυτή την εργασία, αυτή η ιδέα υλοποιείται για ποικίλα εργαζόμενα μέσα σε 5 διαφορετικές Μεσογειακές τοποθεσίες. Η μοντελοποίηση των φωτοβολταϊκών και θερμικών συλλεκτών καθώς και του ηλιακού τροφοδοτικού δοχείου είναι προαπαιτούμενα για τη σύζευξη του συστήματος. Η προσομοίωση του ORC σε συνθήκες λειτουργίας περιλαμβάνει την διαστασιοποίηση του ατμοποιητή, του εκτονωτή, της γεννήτριας, του συμπυκνωτή, της αντλίας και του κινητήρα για κάθε εργαζόμενο μέσο. Το συνολικό κόστος του ORC υπολογίζεται μετά την ολοκλήρωση της διαστασιοποίησης των εξαρτημάτων του. Επειδή η πηγή θερμότητας του κύκλου προέρχεται από μία μεταβαλλόμενη ηλιακή ακτινοβολία, ο υπολογισμός της λειτουργίας του κύκλου σε συνθήκες εκτός των ονομαστικών είναι απαραίτητος. Η ετήσια παραγωγή ηλεκτρισμού από τη σύζευξη του συστήματος PVT-ORC υπολογίζεται στη συνέχεια για ένα μεγάλο εύρος επιφάνειας PVT συλλεκτών καθώς και όγκου ηλιακού τροφοδοτικού δοχείου ως μέρος της βελτιστοποίησης του συστήματος.

Σε όλες τις τοποθεσίες, το R152a αποδεικνύεται ότι είναι η πιο αποδοτική και οικονομικά βιώσιμη επιλογή ως εργαζόμενο μέσο για τον κύκλο, με καθαρό ηλεκτρικό βαθμό απόδοσης ίσο με 6.931% σε συνθήκες λειτουργίας. Η μεγιστοποίηση της επιφάνειας των συλλεκτών και ένα μικρό ηλιακό τροφοδοτικό δοχείο αποτελούν τον πιο βιώσιμο συνδυασμό. Στην πόλη της Αθήνας, με το R152a ως εργαζόμενο μέσο, το μικρότερο κόστος παραγόμενης ενέργειας είναι ίσο με 0.153 €/kWh, η υψηλότερη καθαρή παρούσα αξία είναι ίση με 2244.22 € και η μικρότερη περίοδος αποπληρωμής είναι ίση με 17.05 χρόνια.

Preface

I would like to kindly thank Associate Professor Sotirios Karellas for offering me the opportunity to work on such an innovating technology for my diploma thesis.

I would also like to express my gratitude towards PhD Candidate Tryfon Roumpedakis who helped me with his guidance throughout the completion of this thesis despite his busy schedule.

Finally, I would like to thank my family for their support during my studies.

Table of Contents

ABSTRACT	I
ΠΕΡΙΛΗΨΗ	II
PREFACE	III
TABLE OF CONTENTS	V
LIST OF FIGURES	VII
LIST OF TABLES	IX
CHAPTER 1.INTRODUCTION.....	1
1.1 CONVENTIONAL RANKINE CYCLE	1
1.2 ORGANIC RANKINE CYCLE.....	3
1.3 PHOTOVOLTAIC SYSTEMS	6
1.4 PHOTOVOLTAIC THERMAL SYSTEMS.....	7
1.5 LITERATURE REVIEW	11
1.6 THESIS SCOPE	15
CHAPTER 2.PVT MODELING	17
2.1 PHOTOVOLTAIC MODULE MODELING.....	17
2.2 THERMAL COLLECTOR MODELING.....	27
2.3 STORAGE TANK MODELING	28
CHAPTER 3.ORGANIC RANKINE CYCLE.....	31
3.1 ORC MODELING	31
3.1.1 Evaporator Modeling	32
I. Preheating Zone	35
II. Evaporation Zone.....	36
III. Superheating Zone	38
IV. Overall Calculations.....	39
3.1.2 Expander Modeling.....	40
3.1.3 Generator Modeling	41
3.1.4 Condenser Modeling	42
I. Desuperheating Zone	44
II. Condensation Zone	45
III. Subcooling Zone	46
IV. Overall Calculations.....	47
3.1.5 Pump Modeling	48
3.1.6 Motor Modeling	49
3.2 WORKING FLUID SELECTION.....	50
3.3 ON-DESIGN SIMULATION OF ORC.....	51
3.4 COST OF ORC	61
3.5 OFF-DESIGN SIMULATION OF ORC.....	64
CHAPTER 4.COUPLING OF PVT-ORC SYSTEM.....	69
4.1 MODELING OF THE CONFIGURATION	69
4.2 ENERGETIC AND EXERGETIC RESULTS	71

CHAPTER 5.ECONOMIC ANALYSIS	79
5.1 LEVELIZED COST OF ENERGY.....	83
5.2 NET PRESENT VALUE.....	86
5.3 PAYBACK PERIOD	91
CHAPTER 6.CONCLUSION	95
REFERENCES.....	97

List of Figures

FIGURE 1.1 SCHEMATIC OF A CONVENTIONAL RANKINE CYCLE CONFIGURATION AND T-S DIAGRAM [3]	2
FIGURE 1.2 SCHEMATIC PROCESS SCHEME OF A TYPICAL ORC CONFIGURATION [5]	3
FIGURE 1.3 T-S DIAGRAMS OF (A) A WET FLUID (B) AN ISENTROPIC FLUID AND (C) A DRY FLUID	4
FIGURE 1.4 PV SYSTEM POWERING AC LOADS WITH BATTERY BANK [13]	6
FIGURE 1.5 SCHEMATIC OF (A) FLAT PLATE PVT (B) FLEXIBLE PVT (C) CONCENTRATED PVT [26]	8
FIGURE 1.6 THE CFOH-IHE ORC INVESTIGATED BY TOURKOV AND SCHAEFER [37].....	11
FIGURE 1.7 SCHEMATIC OF THE TRIPLE JUNCTION PV CELL CONSIDERED AT THE STUDY OF RAHBAR ET AL. [39]	13
FIGURE 2.1 I-VOLT CHARACTERISTIC CURVE AT STC	20
FIGURE 2.2 P-VOLT CHARACTERISTIC CURVE AT STC	21
FIGURE 2.3 PV CELL AND AMBIENT TEMPERATURE IN ATHENS	22
FIGURE 2.4 PV POWER PRODUCTION IN ATHENS	22
FIGURE 2.5 PV CELL AND AMBIENT TEMPERATURE IN NAPLES	23
FIGURE 2.6 PV POWER PRODUCTION IN NAPLES.....	23
FIGURE 2.7 PV CELL AND AMBIENT TEMPERATURE IN LARNACA	24
FIGURE 2.8 PV POWER PRODUCTION IN LARNACA	24
FIGURE 2.9 PV CELL AND AMBIENT TEMPERATURE IN MADRID.....	25
FIGURE 2.10 PV POWER PRODUCTION IN MADRID.....	25
FIGURE 2.11 PV CELL AND AMBIENT TEMPERATURE IN LISBON	26
FIGURE 2.12 PV POWER PRODUCTION IN LISBON	26
FIGURE 2.13 EFFICIENCY OF THE THERMAL COMPONENT OF THE PVT AS A FUNCTION OF ITS TEMPERATURE	27
FIGURE 2.14 SCHEMATIC OF THE STORAGE TANK'S MIXING ZONES [48]	29
FIGURE 3.1 SKETCH OF ALFA LAVAL'S MODEL AC30EQ [60]	33
FIGURE 3.2 SCHEMATIC DIAGRAM OF THE DISCRETIZED EVAPORATION ZONE [48]	37
FIGURE 3.3 SKETCH OF ALFA LAVAL'S MODEL CB30 [64]	43
FIGURE 3.4 EVAPORATOR'S SURFACE OF VARIOUS WORKING FLUIDS	58
FIGURE 3.5 CONDENSER'S SURFACE OF VARIOUS WORKING FLUIDS.....	58
FIGURE 3.6 THERMAL EFFICIENCY OF VARIOUS WORKING FLUIDS	59
FIGURE 3.7 NET ELECTRIC EFFICIENCY OF VARIOUS WORKING FLUIDS.....	59
FIGURE 3.8 EXPANDER'S ISENTROPIC EFFICIENCY OF VARIOUS WORKING FLUIDS	60
FIGURE 3.9 PUMP'S ISENTROPIC EFFICIENCY OF VARIOUS WORKING FLUIDS	60
FIGURE 3.10 TOTAL COST OF ORC OF VARIOUS WORKING FLUIDS.....	63
FIGURE 3.11 NET ELECTRIC PRODUCTION AS A FUNCTION OF HEAT INPUT TEMPERATURE.....	66
FIGURE 3.12 NET ELECTRIC EFFICIENCY AS A FUNCTION OF HEAT INPUT TEMPERATURE.....	67
FIGURE 4.1 ORC'S NET ELECTRICITY PRODUCTION AS A FUNCTION OF THE NUMBER OF PVT MODULES AND THE VOLUME OF STORAGE TANK IN ATHENS	71
FIGURE 4.2 ORC'S NET ELECTRICITY PRODUCTION AS A FUNCTION OF THE NUMBER OF PVT MODULES AND THE VOLUME OF STORAGE TANK IN NAPLES	72
FIGURE 4.3 ORC'S NET ELECTRICITY PRODUCTION AS A FUNCTION OF THE NUMBER OF PVT MODULES AND THE VOLUME OF STORAGE TANK IN LARNACA	72
FIGURE 4.4 ORC'S NET ELECTRICITY PRODUCTION AS A FUNCTION OF THE NUMBER OF PVT MODULES AND THE VOLUME OF STORAGE TANK IN MADRID.....	73
FIGURE 4.5 ORC'S NET ELECTRICITY PRODUCTION AS A FUNCTION OF THE NUMBER OF PVT MODULES AND THE VOLUME OF STORAGE TANK IN LISBON	73
FIGURE 4.6 ORC'S MAXIMUM NET ELECTRICITY PRODUCTION FOR THE EXAMINED WORKING FLUIDS IN ATHENS.....	75
FIGURE 4.7 ORC'S MAXIMUM NET ELECTRICITY PRODUCTION FOR THE EXAMINED WORKING FLUIDS IN NAPLES.....	75
FIGURE 4.8 ORC'S MAXIMUM NET ELECTRICITY PRODUCTION FOR THE EXAMINED WORKING FLUIDS IN LARNACA.....	76

FIGURE 4.9 ORC'S MAXIMUM NET ELECTRICITY PRODUCTION FOR THE EXAMINED WORKING FLUIDS IN MADRID	76
FIGURE 4.10 ORC'S MAXIMUM NET ELECTRICITY PRODUCTION FOR THE EXAMINED WORKING FLUIDS IN LISBON	77
FIGURE 5.1 INVESTMENT COST OF THE EXAMINED WORKING FLUIDS FOR THE BEST CASE SCENARIO	80
FIGURE 5.2 ANALYSIS OF THE COST OF EACH COMPONENT OF THE SYSTEM FOR THE CASE OF R152A	81
FIGURE 5.3 ANALYSIS OF THE COST OF EACH COMPONENT OF THE ORC FOR THE CASE OF R152A	82
FIGURE 5.4 LCOE OF THE EXAMINED WORKING FLUIDS AND PV STANDALONE OPERATION IN ATHENS	84
FIGURE 5.5 LCOE OF THE EXAMINED WORKING FLUIDS AND PV STANDALONE OPERATION IN NAPLES.....	84
FIGURE 5.6 LCOE OF THE EXAMINED WORKING FLUIDS AND PV STANDALONE OPERATION IN LARNACA	85
FIGURE 5.7 LCOE OF THE EXAMINED WORKING FLUIDS AND PV STANDALONE OPERATION IN MADRID.....	85
FIGURE 5.8 LCOE OF THE EXAMINED WORKING FLUIDS AND PV STANDALONE OPERATION IN LISBON	86
FIGURE 5.9 NPV OF THE EXAMINED WORKING FLUIDS AND PV STANDALONE OPERATION IN ATHENS	87
FIGURE 5.10 NPV OF THE EXAMINED WORKING FLUIDS AND PV STANDALONE OPERATION IN NAPLES	88
FIGURE 5.11 NPV OF THE EXAMINED WORKING FLUIDS AND PV STANDALONE OPERATION IN LARNACA	88
FIGURE 5.12 NPV OF THE EXAMINED WORKING FLUIDS AND PV STANDALONE OPERATION IN MADRID	89
FIGURE 5.13 NPV OF THE EXAMINED WORKING FLUIDS AND PV STANDALONE OPERATION IN LISBON	89
FIGURE 5.14 NPV OF R152A IN EACH EXAMINED CITY FOR NON-HOUSEHOLD CONSUMERS.....	90
FIGURE 5.15 PBP OF THE EXAMINED WORKING FLUIDS AND PV STANDALONE OPERATION IN ATHENS	92
FIGURE 5.16 PBP OF THE EXAMINED WORKING FLUIDS AND PV STANDALONE OPERATION IN NAPLES	92
FIGURE 5.17 PBP OF THE EXAMINED WORKING FLUIDS AND PV STANDALONE OPERATION IN LARNACA	93
FIGURE 5.18 PBP OF THE EXAMINED WORKING FLUIDS AND PV STANDALONE OPERATION IN MADRID	93
FIGURE 5.19 PBP OF THE EXAMINED WORKING FLUIDS AND PV STANDALONE OPERATION IN LISBON	94
FIGURE 5.20 PBP OF R152A IN EACH EXAMINED CITY FOR NON-HOUSEHOLD CONSUMERS.....	94

List of Tables

TABLE 1.1 <i>NON-EXHAUSTIVE REVIEW OF ORGANIC RANKINE CYCLES DRIVEN BY LOW TEMPERATURE HEAT SOURCES</i>	14
TABLE 2.1 <i>OPTIMAL TILT ANGLES FOR EACH LOCATION</i>	18
TABLE 2.2 <i>DUALSUN CHARACTERISTIC CONSTANTS [47]</i>	20
TABLE 3.1 <i>TECHNICAL CHARACTERISTICS OF EXAMINED FLAT PLATE HEAT EXCHANGERS FOR THE EVAPORATOR</i>	33
TABLE 3.2 <i>TYPICAL FLAT PLATE HEAT EXCHANGERS' DIMENSIONS</i>	33
TABLE 3.3 <i>VALUE OF THE GENERATOR'S COEFFICIENTS</i>	41
TABLE 3.4 <i>TECHNICAL CHARACTERISTICS OF EXAMINED FLAT PLATE HEAT EXCHANGERS FOR THE CONDENSER</i>	42
TABLE 3.5 <i>VALUE OF THE MOTOR'S COEFFICIENTS</i>	49
TABLE 3.6 <i>EXAMINED WORKING FLUIDS AND THEIR PROPERTIES</i>	50
TABLE 3.7 <i>ON-DESIGN PROPERTIES OF PROPYLENE</i>	52
TABLE 3.8 <i>ON-DESIGN PROPERTIES OF PROPANE</i>	53
TABLE 3.9 <i>ON-DESIGN PROPERTIES OF R32</i>	53
TABLE 3.10 <i>ON-DESIGN PROPERTIES OF R134A</i>	54
TABLE 3.11 <i>ON-DESIGN PROPERTIES OF R152A</i>	54
TABLE 3.12 <i>ON-DESIGN PROPERTIES OF R227EA</i>	55
TABLE 3.13 <i>ON-DESIGN PROPERTIES OF R410A</i>	55
TABLE 3.14 <i>ON-DESIGN PROPERTIES OF R-C318</i>	56
TABLE 3.15 <i>ON-DESIGN PROPERTIES OF R1234YF</i>	56
TABLE 3.16 <i>ON-DESIGN PROPERTIES OF R1234ZE</i>	57
TABLE 3.17 <i>TOTAL COST OF THE ORC OF THE EXAMINED WORKING FLUIDS</i>	63
TABLE 3.18 <i>OFF-DESIGN PROPERTIES OF THE EXAMINED WORKING FLUIDS</i>	65
TABLE 4.1 <i>DIMENSIONS OF EXAMINED STORAGE TANKS</i>	71
TABLE 4.2 <i>MAXIMUM NET ELECTRICITY PRODUCTION IN EVERY CITY WITH R152A AS THE WORKING FLUID OF THE ORC</i>	74
TABLE 4.3 <i>ANNUAL PV ELECTRICITY PRODUCTION PER SQUARE METER IN EACH CITY</i>	78
TABLE 4.4 <i>MAXIMUM AND MINIMUM EXERGETIC AND NET ELECTRIC EFFICIENCIES OF THE SYSTEM FOR EACH CITY</i>	78
TABLE 5.1 <i>INVESTMENT COST OF THE EXAMINED WORKING FLUIDS</i>	80
TABLE 5.2 <i>ELECTRICITY PRICES IN THE EXAMINED COUNTRIES ON THE SECOND SEMESTER OF 2018</i>	82

Nomenclature

A	Surface	$[m^2]$
a_{pl}	Plate Amplitude	$[m]$
B	Variable for the calculation of the hour angle	$[^\circ]$
Bo	Boiling Number	–
B_p	Horizontal Distance between nozzles	$[m]$
C	Cost	$[€]$
c_0	Constant of site location	$[W/Km^2]$
c_1	Constant of site location	$[Ws/Km^3]$
c_{ideal}	Ideality Factor	–
c_p	Specific Heat Capacity	$[J/kgK]$
D	Diameter	$[m]$
D_h	Hydraulic Diameter	$[m]$
D_p	Port Diameter	$[m]$
E	Energy	$[J]$
EE	Function of Time	$[min]$
Ex	Exergy	$[J]$
f	Friction Factor	–
ff	Filling Factor	–
G	Mass Velocity	$[kg/sm^2]$
G_T	Total Incline Solar Irradiance	$[W/m^2]$
H	Height	$[m]$
h	Enthalpy	$[J/kg]$
I	Global Horizontal Radiation	$[Wh/m^2]$
i	Discount Rate	–
I_{bn}	Direct Normal Radiation	$[Wh/m^2]$
I_{bT}	Direct Incline Solar Irradiance	$[Wh/m^2]$
IC	Investment Cost	$[€]$
I_d	Diffuse Horizontal Radiation	$[Wh/m^2]$
I_o	Reverse Saturation Current	$[A]$
I_{ph}	Photocurrent	$[A]$
$I_{PV,mod}$	Output Current of a single PV module	$[A]$
I_{sc}	Short Circuit Current	$[A]$
I_T	Total Incline Solar Irradiance	$[Wh/m^2]$
k	Boltzmann Constant	$[J/K]$
L	Length	$[m]$
$LCOE$	Levelized Cost of Energy	$[€/kWh]$
L_{loc}	Location's Longitude	$[^\circ]$

L_p	Vertical Plate Length	[m]
L_{st}	Time Zone's Meridian	[°]
M	Molecular Mass	[kg/kmol]
\dot{m}	Mass Flow Rate	[kg/s]
$Mass$	Total Mass	[kg]
n	Day of the year	–
N_{exp}	Expander's Rotational Speed	[rpm]
N_{pump}	Pump's Rotational Speed	[rpm]
NPV	Net Present Value	[€]
$N_{PV,p}$	Number of parallel modules in an array	–
$N_{PV,s}$	Number of in series modules in an array	–
N_s	Number of cells in the PV module	–
OMC	Operational and Maintenance Cost	[€/y]
P	Power Output	[W]
p	Pressure	[bar]
PBP	Payback Period	[y]
pit	Pitch	[m]
PP	Pinch Point	[K]
pr_{el}	Electricity Price	[€/kWh]
\dot{Q}	Heating Load	[W]
q	Electron Charge	[C]
R	LCOE Coefficient	[y ⁻¹]
R_f	Fouling Resistance	[Km ² /W]
R_p	Shunt Resistance	[Ω]
R_s	Series Resistance	[Ω]
T	Temperature	[°C]
t	Torque	[Nm]
t_{pl}	Plate Thickness	[m]
U	Overall Heat Transfer Coefficient	[W/m ² K]
u_w	Wind Speed	[m/s]
$Volt$	Voltage	[V]
\dot{V}_{exp}	Volumetric Displacement of expander	[m ³ /rev]
V	Volume	[m ³]
\dot{V}_{pump}	Volumetric Flow Rate of pump	[m ³ /s]
v	Velocity	[m/s]
W	Mechanical Work	[W]
x	Liquid's Quality	–

Greek symbols

α	Heat Transfer Coefficient	$[W/m^2K]$
α_v	Corrected Thermal Voltage	$[V]$
β	Tilt Angle of the PV module	$[^\circ]$
δ	Sun Declination	$[^\circ]$
ε_g	Material Band Energy	$[J]$
η	Efficiency	–
θ	Incidence Angle	$[^\circ]$
Λ	Corrugation Pitch	$[m]$
λ	Thermal Conductivity	$[W/mK]$
μ	Dynamic Viscosity	$[kg/ms]$
μ_{sc}	Temperature Coefficient of short circuit current	$[A/K]$
ρ	Density	$[kg/m^3]$
ρ'	Ground's Reflectance	–
Φ	Enlargement Factor	–
φ	Location's Latitude	$[^\circ]$
φ'	Chevron Angle	$[^\circ]$
ω	Hour Angle	$[^\circ]$

Subscripts/superscripts

amb	Ambient
ann	Annual
$array$	PV modules array
ch	Channel
col	Collector
$cond$	Condenser
$cont$	Control
cp	Channels per pass
$crit$	Critical
cs	Cold side
$desup$	Desuperheating Zone
dis	Discharge
el	Electric
eq	Equivalent
$evap$	Evaporator
ex	Exergy
exp	Expander
G	Gas
gen	Generator
hs	Hot Stream
in	Inlet
inv	Inverter

<i>iorc</i>	Hot stream of the evaporator of the ORC
<i>is</i>	Isentropic
<i>L</i>	Liquid
<i>lm</i>	Logarithmic Mean
<i>max</i>	Maximum
<i>mech</i>	Mechanical
<i>min</i>	Minimum
<i>mot</i>	Motor
<i>mp</i>	Maximum Power
<i>nom</i>	Nominal
<i>op</i>	Open Circuit
<i>ORC</i>	Organic Rankine Cycle
<i>out</i>	Outlet
<i>panel</i>	Thermal Collector Panel
<i>pip</i>	Piping
<i>pl</i>	Plate
<i>port</i>	Port
<i>pre</i>	Preheating Zone
<i>pump</i>	Pump
<i>PV, cell</i>	Photovoltaic Module Cell
<i>PV, mod</i>	Photovoltaic Module
<i>PVT</i>	Photovoltaic/Thermal Collectors
<i>ref</i>	Reference
<i>req</i>	Required
<i>sol</i>	Solar
<i>st</i>	Storage Tank
<i>STC</i>	Standard Test Conditions
<i>stream</i>	Stream
<i>subcool</i>	Subcooling Zone
<i>superheat</i>	Superheating Zone
<i>sys</i>	System
<i>tank</i>	Feeding Tank
<i>th</i>	Thermal
<i>tot</i>	Total
<i>wall</i>	Wall of flat plate heat exchanger
<i>wf</i>	Working Fluid

Abbreviations

<i>AC</i>	Alternating Current
<i>ASHRAE</i>	American Society of Heating, Refrigerating and Air-Conditioning Engineers
<i>CFOH</i>	Closed Feed Organic Fluid Heater

<i>CO₂</i>	Carbon Dioxide
<i>CPV</i>	Concentrated Photovoltaic
<i>DC</i>	Direct Current
<i>DSSC</i>	Dye-sensitized Solar Cell
<i>EVA</i>	Ethylene Vinyl Acetane
<i>GWP</i>	Global Warming Potential
<i>HCS</i>	Hydrocarbons
<i>HCFCs</i>	Hydrochlorofluorocarbons
<i>HFCs</i>	Hydrofluorocarbons
<i>HFEs</i>	Hydrofluoroethers
<i>HFOs</i>	Hydrofluoroolefins
<i>IHE</i>	Internal Heat Exchanger
<i>LCOE</i>	Levelized Cost of Energy
<i>NFCPV/T</i>	Nano-fluid based Concentrating Photovoltaic Thermal Collector
<i>NPV</i>	Net Present Value
<i>ODP</i>	Ozone Depletion Potential
<i>OFOH</i>	Open Feed Organic Fluid Heater
<i>ORC</i>	Organic Rankine Cycle
<i>PBP</i>	Payback Period
<i>PCM</i>	Phase Change Materials
<i>PFCs</i>	Perfluorocarbons
<i>PV</i>	Photovoltaic
<i>PVT</i>	Photovoltaic Thermal
<i>VCC</i>	Vapor Compression Cycle

Chapter 1. Introduction

1.1 Conventional Rankine Cycle

Since the industrial revolution, the energy demands of society have grown rapidly. According to International Energy Agency [1], a great percentage of heat and electricity, which are indispensable for industrial processes, public services and households, has been produced for many decades by the combustion of fossil fuels, such as coal, oil and natural gas, in burners of conventional thermal power plants or by nuclear fission in nuclear power plants. The heat produced in both cases is supplied externally to a closed loop of which water is the working fluid. The cycle describing the aforementioned closed loop processes is known as water-steam Rankine Cycle.

Ideal Rankine Cycle is comprised of four consecutive processes (Figure 1.1) as follows:

- Water in saturated liquid phase flows through an isentropic circulating pump so that its pressure is increased.
- High pressure subcooled water enters the boiler through pipes where it is heated externally by the combustion of fossil fuels or by the nuclear fission without pressure losses. This heat is provided in two or three stages. In the first stage of the boiler, called Economizer, water moves from subcooled liquid to saturated liquid phase while in the second stage, called Evaporator, it is fully converted into saturated vapor. In order to achieve higher efficiency, in most of the cases there is a third stage, called Superheater, where saturated vapor turns into superheated steam which has the potential of generating more power and reducing the amount of condensation occurring in the last stages of the steam turbine.
- Superheated or saturated steam expands isentropically through a steam turbine which is coupled with a generator and the produced electricity is supplied to the grid. The pressure in which the working fluid exits the turbine is determined by the operating pressure of the condenser.
- Wet vapor flows through the condenser and it is converted into saturated liquid with an isobaric process. The latent heat of vaporization of water is rejected in cooling towers which can be modeled as large dimensioned heat exchangers. Following this process, the saturated water is stored in the storage tank from which the required quantity of water is extracted so as to restart the closed loop.

In actual power plants, Ideal Rankine Cycle is not feasible. The compression of the subcooled water by the feeding pump and the expansion of the superheated steam by the steam turbine are not isentropic thus leading to an increased power demand for the operation of the pump and a decreased power generation provided to the grid. Furthermore, friction losses due to the flow of the working fluid lead to pressure drops in the boiler, the condenser and the piping system. Moreover, inevitable heat losses occur throughout the closed loop resulting in diminished work output.

A wide variety of methods to enhance the efficiency of the conventional Rankine Cycle have been proposed in literature. First and foremost, according to Carnot's theorem, the cycle's efficiency is proportional to the input temperature of the steam turbine and inversely proportional to the operating temperature of the condenser. The value of the inlet temperature is restricted by the cost and the durability of the materials of the piping system and the blades of the steam turbine. A typical value of steam turbine's inlet temperature is 535°C [2]. Moreover increasing the steam pressure will lead to higher efficiency but also to higher condensation in the last stages of the turbine. Thus a pressure value of 150 bar exiting the feeding pump is standard for a thermal power plant [2]. In order to lower the exiting temperature of the turbine, the condenser's pressure needs to be diminished. A typical condenser's pressure value is 0.03 bar [2].

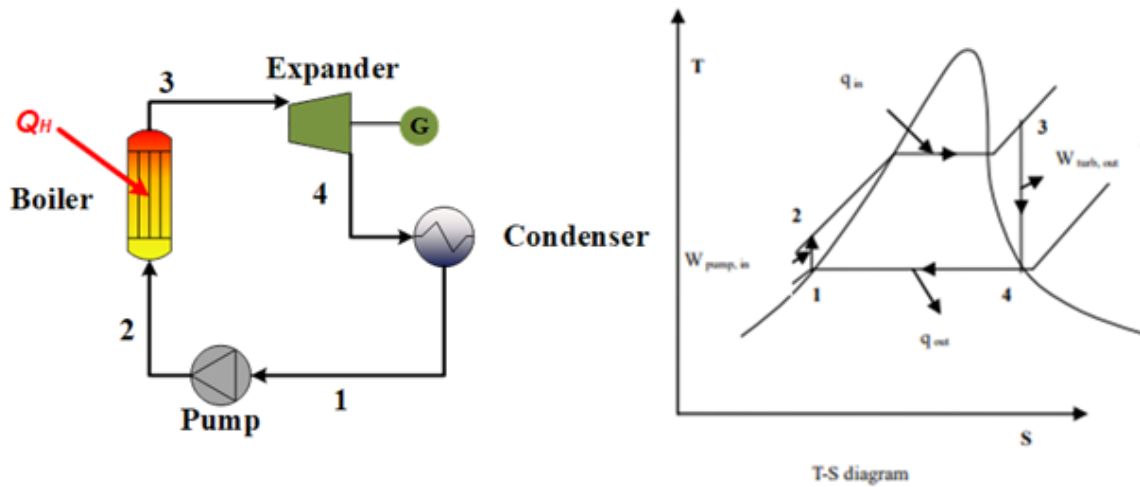


Figure 1.1 Schematic of a Conventional Rankine Cycle configuration and T-s diagram [3]

A widely implemented variation of Rankine Cycle includes reheating of the produced steam. The superheated vapor enters the high pressure turbine and it is expanded. When the steam pressure is equal to approximately a fourth of the feeding pump's pressure, it reenters the boiler so as to get reheated until reaching the inlet temperature of the first turbine. Then it enters a second turbine, which is in series with the first one, and it is fully expanded. The reheating process results in higher efficiency and in decreased condensation of the steam in the low pressure turbine. Nowadays, it is a common practice to use two stages of reheating for maximizing the efficiency of the cycle.

Another common variation of the conventional Rankine Cycle includes the regenerative preheating of water. Steam is extracted from specific stages of the turbine and is used to preheat the water before entering the boiler, therefore leading to decreased fuel consumption. Nevertheless, the amount of steam expanded in the turbine is reduced resulting in less power generation. Proper design of the preheating system leads to an enhancement of the cycle's efficiency. Preheaters are divided into two categories: the *direct-contact preheaters* where the extracted steam is mixed with the water steam before entering the boiler and the *closed feedwater preheaters* where the two fluid currents do not mix. The latter category is further divided into two

subcategories: the first one where the extracted steam after its condensation is mixed with the preheated water and the second one where the condensated current is driven towards the condenser.

1.2 Organic Rankine Cycle

In recent years, the Organic Rankine Cycle (ORC) has been extensively investigated and commercially implemented as a sustainable technology for heat and cooling as well as for electricity generation from low-temperature heat sources, such as solar, biomass, geothermal and waste heat. Thus, ORC is widely used in various microscale decentralized applications.

The operation of ORC is similar to that of Conventional Rankine Cycle (Figure 1.2). However, instead of water, the working fluids of ORCs are organic compounds such as hydrocarbons (HCs), hydrochlorofluorocarbons (HCFCs), hydrofluorocarbons (HFCs), perfluorocarbons (PFCs), ethers, hydrofluoroolefins (HFOs), hydrofluoroethers (HFEs) and siloxanes [4]. Moreover, it is apparent that the main difference of the two cycles is the transferring of the energy content of the heat source to the working fluid. In the Conventional Rankine Cycle the temperature of the water is increased by entering the boiler through pipes, while in the Organic Rankine Cycle the temperature of the working fluid is increased through an intermediate heat exchanger. It is common practice to insert a thermal oil or pressurized water between the heat source and the refrigerant to absorb the fluctuations in the heat supply stream.

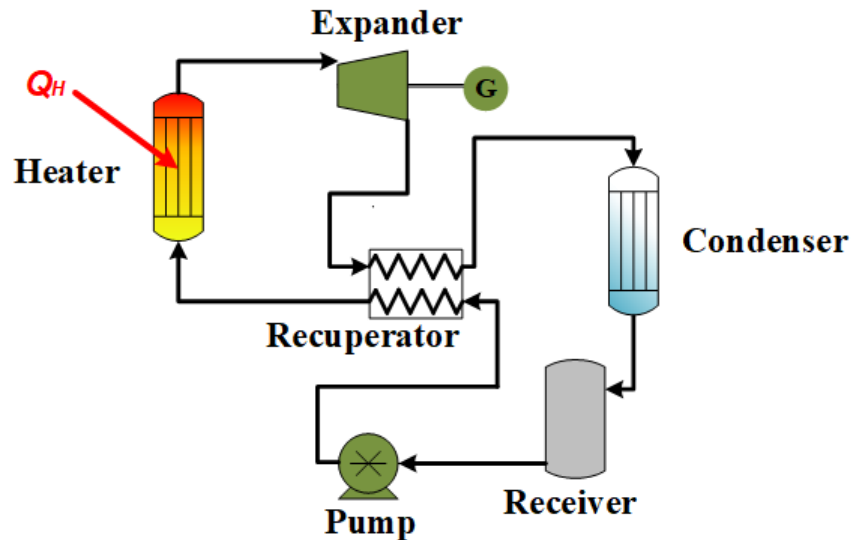


Figure 1.2 Schematic process scheme of a typical ORC configuration [5]

ORC has numerous advantages compared to Conventional Rankine Cycle, therefore resulting in its extensive investigation and implementation. First and foremost, due to the low boiling point and decreased evaporation heat of the used refrigerants, ORC can be used to utilize medium and

low temperature heat sources. Furthermore, many organic fluids, called *dry* fluids, have a positive slope of the saturated vapor curve in the T-s diagram. Therefore, their expansion ends in vapor region and as a result superheating is not required after the evaporator as well as droplet formation is negligible thus leading to the expander's safe operation. Moreover, due to low pressure values in ORCs, a wide variety of expansion machines can be installed in small and microscale applications, such as the scroll and the screw expanders.

The organic compounds used in ORCs can be divided in three categories depending on the derivative of their vapor saturation in T-s diagram (Figure 1.3). These categories are as follows:

- *Wet* fluids which have a negative slope of the saturated vapor curve and low molecular masses, such as water (M=18) and ammonia (M=17).
- *Isentropic* fluids which have a nearly vertical slope and moderate molecular masses, such as R134a (M=102) and R123 (M=153).
- *Dry* fluids which as aforementioned have a positive slope of the saturated vapor curve and high molecular masses, such as HFE7100 (M=250).

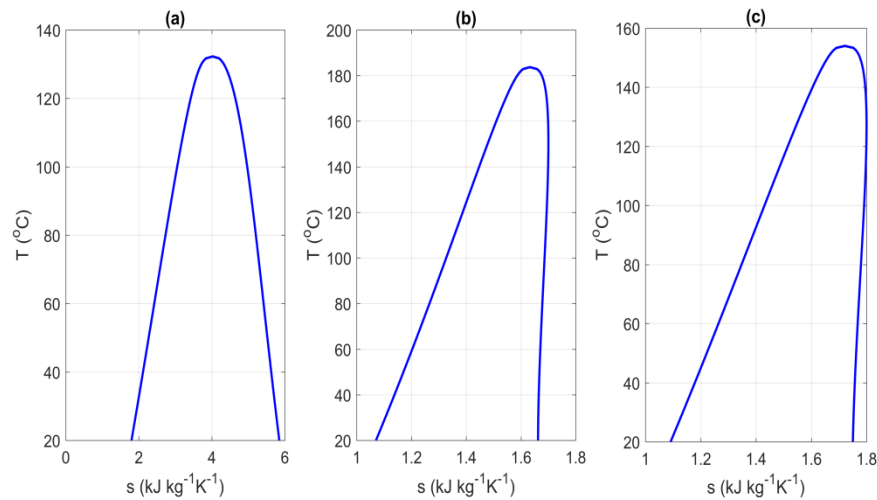


Figure 1.3 T-s diagrams of (a) a wet fluid (b) an isentropic fluid and (c) a dry fluid

The selection of the working fluid for a specific application is a crucial procedure which determines the total efficiency of the cycle and its operational range, therefore defining the capability of utilizing the energy content of the available heat source. Furthermore, it is essential to take into consideration the environmental impact of the working fluid to be used. This impact is characterized by the depletion of the atmospheric ozone layer and the contribution of the refrigerant to global warming. Two indexes are used to describe the contribution of the working fluid to these negative environmental phenomena: the ozone depletion potential (ODP) and the global warming potential (GWP) respectively. Moreover, another crucial parameter to be taken into account is the safety of working fluids. The toxicity, corrosiveness and flammability of the refrigerants must be as low as possible, in order to ensure the safety of the people and the equipment in case of a leakage or to prevent an explosion in an accident.

Another parameter which determines the selection of working fluids is their availability and cost for each application. Refrigerants which are widely used in industrial processes are characterized by low cost due to their mass production thus leading to their easy acquisition. Working fluids which are expensive and scarce may lead to high operation and maintenance cost of the cycle and result in practical problems if their replacement is critical but their availability limited.

The selection of the working fluid determines the type of the expansion machine which is best suitable for the application due to the fact that depending on the operating conditions a working fluid might not be fitting for a specific expander. The expansion machines which are widely installed in ORCs are axial and radial turbomachines and screw and scroll expanders (positive displacement expanders) [6].

Axial turbomachines can offer single-stage expansion for low and medium temperatures at the expense of low pressure ratios due to low speed of sound. Moreover, they are not suitable for very-small-scale implementations because of very high rotational speeds (up to 50,000 rpm). Radial turbines, on the other hand, offer high pressure ratios and efficiency even at part load conditions and a light construction. They are mainly used for power generation at the range of 50 – 500 kW. Nevertheless, radial turbines are characterized by their high cost, the difficulty of assembling stages in series and their low efficiency for high Mach numbers (above 0.85).

Screw expanders, with power capacity of 15 – 200 kW, operate with low rotational speeds and high off-design efficiency. Furthermore, two-phase operation is feasible. However, lubrication is mandatory and the construction and seal of the expander is challenging, thus making it a slightly expensive option for an ORC expander. Scroll expanders, with low power capacity of 1 – 10 kW, are characterized by high efficiency and durability as well as by low cost, noise and rotational speeds. Moreover, two-phase operation is feasible, similarly to screw expanders. Despite its simple and light construction, complicated geometry is inevitable and lubrication is required for its safe operation. Last but not least, another disadvantage of scroll expanders is their small expansion ratios.

Scroll and screw expanders are constrained by the built-in volume flow ratio, which is usually lower than 4 and 5 respectively [7]. When the volume flow ratio of the working fluid largely deviates from the built-in ratio, expanders serially connected may be used. Finally, another limitation that needs to be taken into consideration is the flow capacity ranges of these expanders. These ranges depend on the swept volume per rotation and the rotational speed of positive displacement expanders, which is usually below 6000 rpm. According to Quoilin et al. [7] the flow rates of scroll and screw expanders range between 1.1 – 49 and 25 – 1100 lt/s respectively.

1.3 Photovoltaic Systems

Global energy demand is constantly increasing, thus new solutions for energy supply, energy conservation and environmental protection are highly desirable. This purpose can be served by utilizing renewable energy, such as solar energy. At present, the most common solar technologies are solar thermal heat and solar photovoltaic (PV), which contribute towards a great share of energy supply worldwide [8]. In 2014 the globally installed total capacity of PV systems was 177 GW_e . The installed total capacity is expected to be increased in the future, as according to International Energy Agency's projections by 2050 there will be 3000 GW_e of installed PVs worldwide covering almost 11% of the expected global supply of electricity[9] .

Photovoltaic system technology is based on the conversion of photons from the sun into electricity in the PV cell, which is a solid-state semiconductor and is the essence of a PV system. By combining PV cells into large groups, PV modules are formed. Connecting the latter in a parallel series configuration results in a PV array [10]. Due to the fact that the output of a PV cell is direct current (DC) while most power consuming devices operate with alternating current (AC) [11] as an input, the installation of an inverter is mandatory, as seen in (Figure 1.4). Furthermore, a battery is commonly implemented so as to store DC voltage throughout charging mode and supply electrical energy during discharge mode [12].

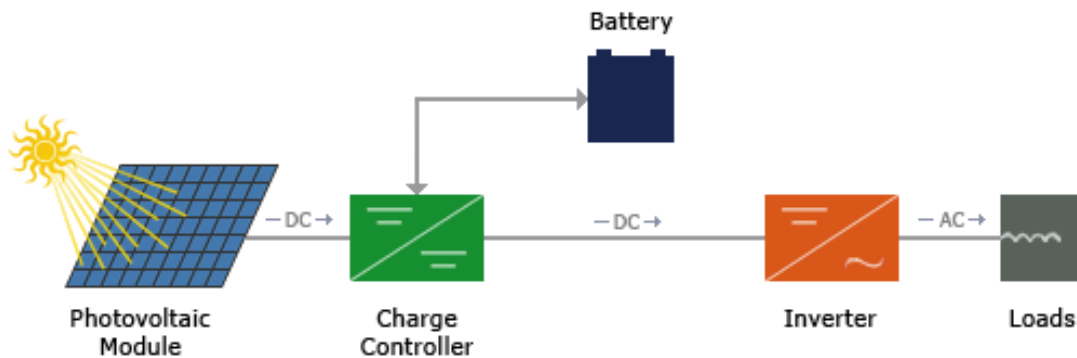


Figure 1.4 *PV System powering AC loads with battery bank [13]*

PV cells are made of semiconductor materials, such as mono- or poly-crystalline silicon, copper indium gallium selenide (CIGS), gallium arsenide (GaAs) and cadmium telluride (CdTe). The most commonly used material, with over 80% of installations [14], is silicon but other materials are nowadays used due to various advantages. GaAs has a similar structure to silicon. It is characterized by low efficiency compared to silicon, but its high heat resistance and its low weight lead to its wide use as a material in concentrated photovoltaic systems (CPV) and in space applications [15]. The need for thin films has led to the research of CIGS and CdTe as PV cell materials. The main challenges that confine their share in the market are the shortage of indium and the toxicity of cadmium respectively [16].

Organics and polymers have been proposed in literature as environmentally friendly solutions for PV cells. Their low cost, disposability, mechanical flexibility and light weight lead to wide

research for their use in the PV market. However, the efficiency of these materials is quite low in comparison to currently available technologies [17, 18]. Another new technology which is investigated by researchers is the dye-sensitized solar cell (DSSC). DSSC materials, such as titanium oxide (TiO_2) are characterized by low production costs and wide availability, they pose no harm to the environment and they are able to operate efficiently with diffused light, thus allowing for energy production at dawn, dusk or cloudy days [19].

Photovoltaic systems have been installed globally in great numbers due to various advantages they pose. First and foremost, the construction of a PV module is characterized by its design simplicity and its low maintenance costs. Moreover, the power density of a PV module is the highest among other renewable technologies and a stand-alone operation is feasible.

On the other hand, PV technology has numerous disadvantages. The reduction of the production cost of a PV module is a challenge due to the high cost of its materials. The efficiency of a typical PV module is very low not only because it is unable to absorb solar radiation from the complete solar spectrum but also because most of the solar radiation is converted into heat losses. Furthermore, high temperatures induce further efficiency decline. In order to alleviate this problem, it is an urgent need to reduce the temperature of the PV system. The simplest and least expensive method to accomplish that is with either natural or forced-air circulation. A more effective but expensive method of cooling is water-heat extraction [20] as in Photovoltaic Thermal (PVT) Systems which will be subsequently elaborated.

1.4 Photovoltaic Thermal Systems

Researchers in an effort to increase the efficiency of PV systems and simultaneously generate heat and electricity proposed the coupling of photovoltaic modules with solar thermal components in the late 1970s. These systems, called photovoltaic thermal (PVT) systems, improve the efficiency of the PV panel by reducing its temperature with the circulation of a working fluid of the thermal subsystem. Moreover, the temperature reduction leads to longer life of the PV panel as the silicon decay due to high temperatures is prevented. The extracted heat can be used in various applications, including space and water heating, crop drying, industrial process heating and preheating. PVT systems provide heat and electricity cogeneration in smaller area and with only low added cost compared to the installation of a PV and solar thermal system separately [21]. The PV layer may fully or partially cover the thermal absorber.

PVT systems are divided into flat-plate, flexible and concentrated according to the type of their PV module. Flat plate PVT systems consist of a flat-plate PV module which produces electricity from sunlight and a solar thermal absorber at the back which cools down the PV by extracting the excessive heat. This heat can be later used for a wide range of applications, such as hot water supply, solar cooling, thermal storage, desalination, space and pool heating. Flat plate systems may be glazed or unglazed. The first system results in higher electricity production, while the

latter in increased heat extraction. Nevertheless, no more than three glass covers are recommended due to very low electrical efficiency [22].

Flexible PVT operate in low and medium temperature like flat plate systems. Their structure is similar to that of flat plate systems, but their PV material is often amorphous Silicon (α -Si). Their electrical efficiency is pretty low (5-10%) [23] compared to the equivalent value of flat plate PVT (6.7-15%) [24] but their thermal efficiencies are equal (22-79%) [24]. On the other hand, concentrated PVT systems operate in high temperatures due to their compound parabolic concentrator. Their electrical efficiency is almost equal to that of flat plate collectors (7-16%) while their thermal efficiency is (39-70%) [25]. Flexible PVT systems can be used for hot water supply, space heating and fresh water production, while concentrated PVT are ideal for absorption and adsorption refrigeration and dehumidification due to the high temperature of their working fluid as well as for hot water supply, fresh water production and greenhouse drying.

The structures of the three aforementioned types of PVT systems depending on the type of their PV module are depicted in Figure 1.5.

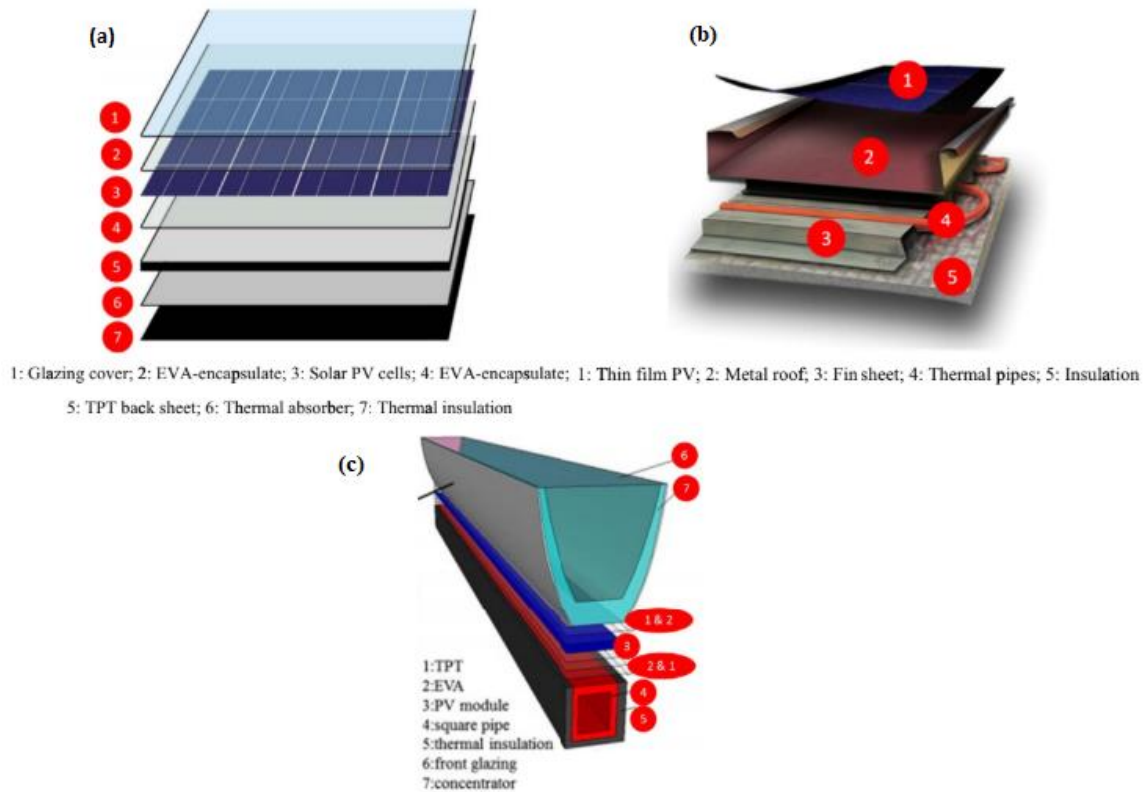


Figure 1.5 Schematic of (a) Flat Plate PVT (b) Flexible PVT (c) Concentrated PVT [26]

Recent research indicates that different types of thermal absorbers are better suited depending on the PVT module application. The most prominent type of thermal absorber in PVT technology is the *sheet-and-tube* structure owing to its good heat-transfer efficiency and its low cost due to established industry. Nevertheless, it is not exclusively used as it is characterized by complex structure with demanding welding techniques and heavy weight with risk of leakage of the

working fluid. Another widely implemented thermal absorber in PVT technology is *rectangular tunnel with or without fins/grooves*. A great range of working fluids, such as water, air, phase change materials, thermal oil and nanofluids, can be used in large scale projects. Their simple structure, low cost and low weight have led to their great popularity despite their relatively low efficiency. The addition of fins or grooves improves the heat-transfer efficiency as the flow becomes more turbulent [22] [27] . These two types of thermal absorbers can be installed in all three types of PVT modules that were aforementioned.

Flat plate tube is a common absorber of flat plate PVT modules as it improves the contact between the thermal and the PV layer. However, its high flow resistance and leakage risk combined with the increased fluid temperature confine its establishment as a prominent thermal absorber. Novel technologies for flat plate and flexible PVT modules include the *micro-channel heat pipe* which is characterized by its high heat transfer performance and reliability [28] but also by its increased thermal resistance and uneven temperature distribution, the *extruded heat exchanger* with its simple and inexpensive construction but its high volume of working fluid, the *roll-bond heat exchanger* which is characterized by its uniform temperature profile, low weight and high efficiency, yet it is not long-term reliable and there is a high risk of corrosion, and the *cotton wick structure* which is inexpensive but inefficient.

The integration of PVT modules impinges on their thermal efficiency due to thermal resistance between PV layer and thermal absorber. Different integration methods have been proposed depending on the application. *Direct contact* of the two layers is the simplest solution with no additional thermal resistance, yet high freezing risk in cold environments and low heat removal efficiency have led to its limited application. This method is applicable in flat plate and flexible PVT modules. Another method which can be implemented in all PVT modules is the use of *thermal adhesive*. This technique is simple and inexpensive, but the formation of mini air-gap bubbles and the imprecision of the adhesive thickness result in increased heat losses [24]. Mechanical fixing of flat plate and concentrated PVT systems ensures firm combination of the PV and thermal layer. Nevertheless, the existence of air gaps combined with high cost and weight of the equipment decrease the overall efficiency. The most promising integration technique for flat plate PVT systems is the *EVA based lamination*. This method is cost-effective and secures a firm, low thermal-resistant combination, although careful attention need to be paid during the lamination process in order to avoid geometry deformation [29].

PVT systems can be further divided according to the type of working fluid of the thermal subsystem. First and foremost, in *air based* PVT modules, air is designed to pass through the PV surface with either active or passive mode through various absorber configurations. Single or double pass may be used, the latter being more efficient than the former [11]. Experiments conducted by Jin et al. [30] showed that higher thermal efficiency is obtained with a glazed system while higher electrical efficiency is achieved with an unglazed one. The main disadvantage of air based systems is their inability to work efficiently at high temperature due to air's low density and heat capacity.

Water based PVT modules, on the other hand, achieve higher thermal output compared to air based, as water has better heat transfer properties than air. Nevertheless, the cost of additional

water heat exchanger should be taken into consideration during the design of the system. Research results indicate that the use of glass covers results in higher thermal and energy output, while an unglazed system provides higher electrical and exergy output [31]. *Bifluid based* PVT systems are designed in order to overcome the limitations of air- and water-based PVT modules. The two fluids used by researchers are water and air, resulting in higher total efficiency at the expense of higher power consumption and more expensive construction.

Novel PVT systems proposed include the use of nanofluids, heat pipes and phase change materials (PCM). Nanofluids may be used either as heat transfer fluids or as optical filters depending on their properties and characteristics, resulting in significant enhancement on performance parameters of PVT systems [32, 33]. Heat pipes extract heat from the PV back surface for the evaporation process. This heat is then offered as a thermal output to a working fluid via the condensation process and can be used for various applications, such as hot water supply, space heating etc. Last but not least, PCM proposed in literature improve the efficiency of PVT systems. Nevertheless, careful attention should be paid to their melting temperature and thickness so as to obtain the desirable benefits of their integration.

Research work has been extensively carried out in building integrated PVT systems in order to accomplish a more viable and prominent solution for building heat load. A great number of working fluids have been studied, such as water, air, heat pipe, PCM, showing promising results as a sustainable technology for heat and electricity production [34, 35].

As aforementioned, conventional and novel PVT technologies included, the bifluid based PVT systems offer the highest total efficiency at the expense of high cost. Water based systems are characterized by high thermal output, while the novel technologies result in high electricity production.

High temperature of PV cell leads to reduced efficiency of the PVT system. Thus, overheating prevention and stagnation handling measures have been proposed. Shading is seldom used as it reduces the electrical output and it is exposed to extreme weather conditions. Methods which demand external power include night-time tank cooling with low implementation cost, tank fluid purging with similar results as the former method and active collector heat dumping which is simple, reliable and effective albeit expensive. The most appealing technology is venting as its electrical output is high. This technology needs to be further researched as its expensive structure and complexity restrict its wide implementation. Lastly, the use of silicone encapsulants instead of EVA lamination reduce the risk of stagnation in medium temperatures, but their high cost, which is 7 times higher than EVA layers, is a restraint towards their implementation [36].

1.5 Literature Review

The coupling of ORC with PVT collectors has not been studied extensively in literature as it is a novel method of exploiting the full potential of solar energy, while at the same time the relatively low temperatures extracted from the PVTs result in lower ORC efficiencies and thus discourage the thorough investigation of the coupling.

A thorough performance evaluation of a PVT/ORC system has been conducted by Tourkov and Schaefer [37] in which various photovoltaic materials and working fluids were studied. For the evaluation, a constant evaporation temperature $T_{evap} = 100^{\circ}\text{C}$ and condensation temperature $T_{cond} = 30^{\circ}\text{C}$ were considered. Firstly, a simple Organic Rankine Cycle was analyzed and it was proven that R11 had the highest efficiency ($\eta_{th} = 0.1358$) while having acceptable volume ratio and comparably low volumetric flow rate. Nevertheless, the use of this working fluid is not recommended as, due to its high ODP, it has been phased out by 2010 following Montreal's Protocol. The addition of an internal heat exchanger (IHE) increased the overall performance. The highest efficiency was observed by n-dodecane ($\eta_{th} = 0.148$). An alternate modification included a medium pressure bleed from the expander into an open or closed feed organic fluid heater (OFOH, CFOH) attaining thermal efficiencies of $\eta_{th} = 0.1454$ and $\eta_{th} = 0.1469$ for R11 respectively. The last system configuration examined included the addition of an IHE and a CFOH (Figure 1.6).

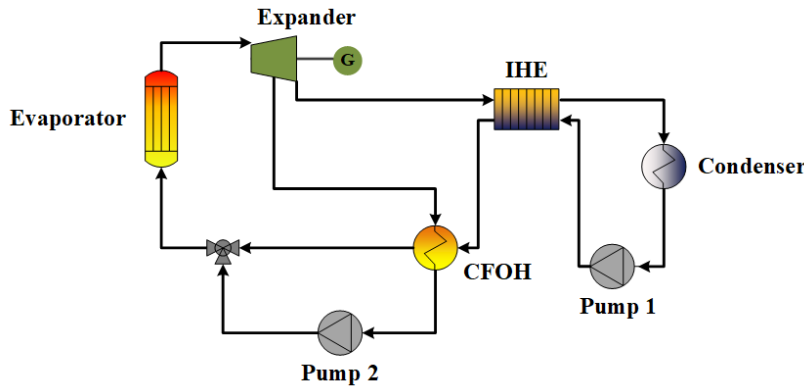


Figure 1.6 The CFOH-IHE ORC investigated by Tourkov and Schaefer [37]

This configuration proved to be the most promising solution as a thermal efficiency of $\eta_{th} = 0.1526$ was attained for n-dodecane. However, the use of heavy alkanes is not recommended due to their high flammability. Light alkanes, on the other hand, have the highest potential when evaluated on the basis of environmental sustainability and efficiency despite their flammability. These working fluids include n-Butane, Isopentane, n-Pentane, Isohexane, n-Hexane, the use of latter results into higher efficiency but its high volumetric ratio leads to a more expensive equipment. Finally, n-Butane was found to be the most promising working fluid being at the same time economically and environmentally viable. The optimized ORC was then combined with 5 different PV cells to examine the enhancement on overall efficiency over standalone PV

operation. It was concluded that the CdS cells almost double their overall efficiency, while triple-junction cells were able to achieve over 45% solar efficiency while operating at 110°C.

The combination of ORC with a concentrating PV/T system was examined by Kosmadakis et al. [38] in order to increase the total power generation. For the study, silicon-based collectors with a concentrated ratio equal to 10 were used and the working fluid selected was R-245fa with low mass flow rate and condensation temperature of $T_{cond} = 40^{\circ}\text{C}$. Considering the PV cells' temperature to be equal to 100°C , the electrical efficiency of the PV was equal to $\eta_{el,CPV} = 8.4\%$ while the total efficiency of the application was $\eta_{tot} = 10.58\%$. The highest total efficiency ($\eta_{tot} = 11.83\%$) was observed when the evaporation temperature was equal to $T_{evap} = 130^{\circ}\text{C}$. By comparing the annual efficiency of the CPV system with or without the coupling of an ORC, ($\eta_{tot} = 10.58\%$ and $\eta_{total} = 4.36\%$ respectively while $T_{PV,cell} = 100^{\circ}\text{C}$) it is apparent that the implementation of the ORC is a promising solution for high electrical energy yield. Last but not least, it was concluded that the combined system has a superior economic performance than the standalone CPV system when the electricity cost is considered as an independent variable.

Rahbar et al. [39] conducted a thorough research about the coupling of an ORC with a nano-fluid based concentrating PVT Collector (NFCPV/T) in order to achieve high heat recovery, energy efficiency and performance enhancement. For the study a parabolic trough collector was used, while the working fluid selected was R1233zd and the nano-fluid was a solution of water with Ag. The research included a comparative study between water and nano-fluid based CPV/T, in which the evaporation temperature was selected equal to $T_{evap} = 80^{\circ}\text{C}$ and the condensation temperature $T_{cond} = 30^{\circ}\text{C}$. It was demonstrated that the nano-fluid based system was more efficient than the water based one ($\eta_{tot} = 20.5\%$ and $\eta_{tot} = 17.79\%$ respectively) for concentration values greater than 7. Furthermore, its electrical and thermal efficiencies had greater values as well ($\eta_{el} = 15.38\%$ and $\eta_{th} = 6.744\%$ compared to $\eta_{el} = 13.31\%$ and $\eta_{th} = 5.72\%$ of the water based system). These results make evident, that the proposed coupling of NFCPV/T with ORC is able to enhance performance and efficiency substantially when developing solar concentrating power systems.

As aforementioned, the coupling of an ORC with PVT collectors is not widely investigated in literature. Thus, the mention of the coupling of ORCs with low-temperature solar thermal collectors is of interest.

Delgado-Torres and García-Rodríguez [40] investigated the implementation of an Organic Rankine Cycle with solar thermal collectors. Four different configurations were examined, but only two of them concerned for low-temperature profiles. One configuration with a flat-plate collector and one with a compound parabolic collector worked at low temperatures, as the evaporation temperature was approximately $T_{evap} = 80^{\circ}\text{C}$, the superheating value was $T_{superheat} = 95^{\circ}\text{C}$ and the condensation temperature was $T_{cond} = 30^{\circ}\text{C}$. Flat-plate collectors showed more promising results, as for various working fluids the thermal efficiency of the ORC and the solar power cycle efficiency were higher. Both configurations operated better with Isopentane as their working fluid, with an equal thermal ORC efficiency $\eta_{th} = 10.49\%$ while the solar power cycle efficiencies were equal to $\eta_{sol} = 4.45\%$ and $\eta_{sol} = 4.03\%$ for the flat-plate

and the parabolic collector respectively. It is worth mentioning that the highest thermal efficiency ($\eta_{th} = 16.40\%$) was attained for an evacuated tube collector with Isopentane as its working fluid for a superheating temperature equal to $T_{superheat} = 145^\circ\text{C}$.

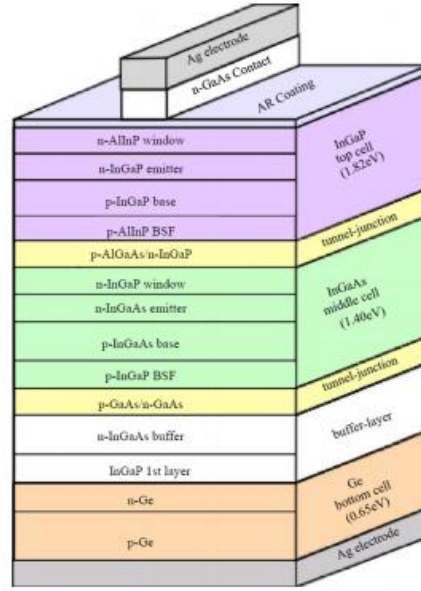


Figure 1.7 Schematic of the triple junction PV cell considered at the study of Rahbar et al. [39]

Michaël Marion et al. [41] investigated the implementation of single and double-glazed flat-plate collectors as the heat source for an ORC. The working fluids examined were R134a, R227ea and R365mfc. When the single-glazed configuration was studied, the evaporation temperature varied between $T_{evap} = 70 - 85^\circ\text{C}$ for all refrigerants and their energetic efficiency was approximately 4 – 5% for a solar radiation equal to $G = 850\text{W}/\text{m}^2$. R365mfc was the most effective working fluid and R227ea the least one. Adding an improved second glazing increased the expected efficiency up to 7% for R134a and R227ea and up to 8% for R365mfc. However, the implementation of a second glazing resulted into higher evaporation temperatures ($T_{evap} = 95^\circ\text{C}$ for R134a and R227ea, $T_{evap} = 120^\circ\text{C}$ for R365mfc). Lastly, the addition of an IHE at the double-glazed collector, with R365mfc as its working fluid, resulted into the highest efficiency equal to 11%. It was concluded that the overall efficiency installation strongly depends on the mass flow rate of the working fluid which appears as a linear function of solar radiation.

Wang et al. [42] compared the performance of pure and zeotropic mixtures for an ORC which exploited the thermal energy of flat plate collectors. The fluids examined were pure R245fa and two zeotropic mixtures of R245fa and R152a with 0.9/0.1 and 0.7/0.3 ratios respectively. The selection of these refrigerants was based on their low GWP and zero ODP. It was observed that the addition of R152a resulted into higher power output and cycle's efficiency. The 0.7/0.3 mixture attained the highest ORC thermal efficiency equal to $\eta_{th} = 5.59\%$ while the efficiency of the other two working fluids were 4.29% (0.9/0.1) and 4.16% (pure R245fa), with a superheating temperature $T_{superheat} = 85^\circ\text{C}$. The overall efficiency of the installation was

$\eta_{tot} = 1.28\%$ as the collector's efficiency was equal to 22.93%. The study concluded that the incorporation of an external heat exchanger might improve the overall efficiency of the zeotropic mixtures as the partial condensation heat can be recovered.

A non-exhaustive review of Organic Rankine Cycles driven by low temperature heat sources is listed at Table 1.1.

Table 1.1 *Non-exhaustive review of Organic Rankine Cycles driven by low temperature heat sources*

Maximum Cycle Temperature (°C)	Heat Source	Working Fluid	Thermal Efficiency (%)	Reference
100	PVT collectors <ul style="list-style-type: none"> ▪ Simple cycle ▪ IHE ▪ OFOH ▪ CFOH ▪ IHE and CFOH 	<ul style="list-style-type: none"> ▪ R11 ▪ n-dodecane ▪ R11 ▪ R11 ▪ n-dodecane 	<ul style="list-style-type: none"> ▪ 13.58 ▪ 14.80 ▪ 14.54 ▪ 14.69 ▪ 15.26 	Tourkov and Schaefer [37]
90	Concentrated PVT collectors	R245fa	8.47	Kosmadakis et al. [38]
80	Concentrated PVT collectors <ul style="list-style-type: none"> ▪ Water-based ▪ Nano-fluid based 	R1233zd	<ul style="list-style-type: none"> ▪ 5.72 ▪ 6.744 	K. Rahbar et al. [39]
95	<ul style="list-style-type: none"> ▪ Flat-plate Collectors ▪ Compound Parabolic Collectors 	Isopentane	<ul style="list-style-type: none"> ▪ 10.49 ▪ 10.49 	A. Delgado-Torres and L. García-Rodríguez [40]
85	▪ Single-glazed Flat-plate collectors	R365mfc	5	Michaël Marion et al. [41]
95	▪ Double-glazed Flat-plate collectors	R134a	7	
85	Flat-Plate collectors	Zeotropic Mixture (0.7 R245fa/0.3 R152a)	5.59	Wang et al. [42]

1.6 Thesis Scope

As indicated by subchapter 1.5, the coupling of a PVT-ORC system has not yet been thoroughly investigated, thus there is significant room for improvement. This study aims to examine from both an energetic/exergetic as well as an economical point of view the potential coupled system and identify its viability as a decentralized application.

In the next chapters, the main questions to be addressed are the following:

- How could the PV modules as well as the thermal collectors and the solar storage tank be modeled for an accurate and computationally fast approach for year round simulations?
- Which are the optimal design aspects for an efficient solar driven Organic Rankine Cycle?
- How will the off-design operation of the cycle be estimated?
- How efficient from an energy and exergy point of view is the PVT-ORC system?
- What is the total cost of the ORC as well as of the whole system?
- How applicable is the considered solution for a residential building?

In order to answer the above questions, a detailed modeling of the PVT modules and the components of the ORC has to be realized. Then, the on and off-design simulation of the cycle is feasible. Finally, the separate models will be coupled into a single entity, which will be implemented in different case scenarios in order to find the most optimum combination which minimizes the payback period and the annual cost of energy.

Chapter 2. PVT Modeling

2.1 Photovoltaic Module Modeling

The heat source of the ORC studied at this thesis is a water/glycol mix which is the working fluid of PVT collectors produced by DualSun. For the modeling of the PV modules of this installation, the procedure proposed by Bellia et al [43] was used.

First step towards the modeling of the PV modules is the calculation of their optimal tilt angle for maximizing annual solar irradiance on their surface. For this purpose, the annual meteorological data of 5 European cities (Athens, Naples, Larnaca, Madrid and Lisbon) are used. By combining some of these data (global horizontal radiation, direct normal radiation and diffuse horizontal radiation) with the latitude, longitude and time zone meridian of each city, the hourly incident solar radiation for an optimal tilt angle is calculated throughout the whole year. The procedure is consequently elaborated.

For each hour of the year, the next equations are used:

$$I_T = I_{bT} + I_d * \frac{1 + \cos\beta}{2} + I * \rho' * \frac{1 - \cos\beta}{2} \quad (2.1)$$

where I_T is the total incline solar irradiance on the PV module, I_{bT} is the direct incline solar irradiance, I_d is the diffuse horizontal radiation, β is the tilt angle of the PV module, I is the global horizontal radiation and $\rho' = 0.2$ is a typical value of ground's reflectance.

$$I_{bT} = I_{bn} * \cos\theta \quad (2.2)$$

where I_{bn} is the direct normal radiation and θ is the incidence angle which is calculated by the following equation for PV modules installed at northern hemisphere with south orientation:

$$\cos\theta = \sin\delta * \sin(\varphi - \beta) + \cos\delta * \cos(\varphi - \beta) * \cos\omega \quad (2.3)$$

where φ is the latitude of the location, δ is the sun declination calculated by next equation and ω is the hour angle (deviation from solar noon).

$$\delta = 23.45 * \sin\left(\frac{360}{365} * (284 + n)\right) \quad (^\circ) \quad (2.4)$$

where n is the day of the year.

$$\omega = 0.25 * (time(\text{min}) \pm 4 * (L_{st} - L_{loc}) + EE - 12 * 60) \quad (2.5)$$

where L_{st} is the meridian of the location's time zone, L_{loc} is the longitude of each location and $-$ is for east longitudes while $+$ is for west. EE is a function of time defined as follows:

$$EE = 9.87 * \sin(2B) - 7.53 * \cos(B) - 1.5 * \sin(B) \quad (\text{min}) \quad (2.6)$$

$$B = 360 * \frac{n - 81}{364} (^{\circ}) \quad (2.7)$$

The results of this procedure are summarized at Table 2.1.

Table 2.1 *Optimal tilt angles for each location*

City	Latitude ($^{\circ}$)	Tilt Angle ($^{\circ}$)
Athens	37.98 N	25.52
Naples	40.83 N	25.20
Larnaca	34.88 N	26.30
Madrid	40.45 N	25.71
Lisbon	38.73 N	29.23

By applying a set of different values for the voltage of the module from 0 up to the open circuit voltage, the output currents are calculated, for a set of ambient temperature and solar irradiance for the aforementioned tilt angles. The voltage and current of the module are determined by finding the values that maximize the power output.

The performance of a PV module is highly affected by its cell temperature ($T_{PV,cell}$), thus the estimation of this temperature is of utmost importance. For the calculation of the PV cell temperature, the Faïman model [44] is used:

$$T_{PV,cell} = T_{amb} + \frac{I_T}{c_0 + c_1 u_w} \quad (2.8)$$

where T_{amb} is the hourly ambient temperature of each location, u_w is the wind speed and c_0, c_1 are a set of constants dependent on the site location. The values of these constants are considered to be equal for all researched locations due to their Mediterranean climate [45]:

$$c_0 = 41.86 \text{ W/Km}^2$$

$$c_1 = 3.95 \text{ Ws/Km}^3$$

For a single diode mode, the output current $I_{PV,mod}$ of a single module can be estimated as following [46], by taking into consideration the series R_s and the shunt R_p resistance:

$$I_{PV,mod} = I_{ph} - I_o \left(\exp \left(\frac{V_{olt_{PV,mod}} + I_{PV,mod} R_s}{a_v} \right) - 1 \right) - \frac{V_{olt_{PV,mod}} + I_{PV,mod} R_s}{R_p} \quad (2.9)$$

where:

➤ I_{ph} is the photocurrent of a single module and is calculated from the following equation:

$$I_{ph} = \frac{I_T}{I_{T,STC}} * \left(I_{sc,STC} + \mu_{sc} (T_{PV,cell} - T_{PV,cell,STC}) \right) \quad (2.10)$$

where $I_{T,STC}$ is the solar irradiance at standard test conditions (STC) and is equal to 1000 Wh/m^2 , $I_{sc,STC}$ is the short circuit current at STC, μ_{sc} is the temperature coefficient of short circuit current, $T_{PV,cell}$ is the PV cell temperature and $T_{PV,cell,STC}$ is the cell's temperature at STC and is equal to $T_{PV,cell,STC} = 298 \text{ K}$.

- I_o is the reverse saturation current of a single module and is calculated from the following equation:

$$I_o = I_{sc,STC} * \exp\left(\frac{-Volt_{oc,STC}}{a_v}\right) * \left(\frac{T_{PV,cell}}{T_{PV,cell,STC}}\right)^3 * \exp\left(\frac{q * \varepsilon_g}{c_{ideal} * k} * \left(\frac{1}{T_{PV,cell}} - \frac{1}{T_{PV,cell,STC}}\right)\right) \quad (2.11)$$

where $Volt_{oc,STC}$ is the open circuit voltage at STC, ε_g is the material band energy and a_v is the corrected thermal voltage and is calculated from the following equation:

$$a_v = N_s * c_{ideal} * k \frac{T_{PV,cell}}{q} \quad (2.12)$$

where N_s is the number of cells in the PV module, c_{ideal} is the ideality factor, $k = 1.3806 * 10^{-23} \text{ J/K}$ is the Boltzmann constant and $q = 1.602 * 10^{-19} \text{ C}$ stands for the electron charge.

- R_p is the shunt resistance and is estimated from the following expression:

$$R_p = \frac{Volt_{mp,STC} + I_{mp,STC} * R_s}{I_{sc,STC} * \left(1 - \exp\left(\frac{Volt_{mp,STC} + I_{mp,STC} * R_s - Volt_{oc,STC}}{a_v}\right) + \exp\left(\frac{-Volt_{oc,STC}}{a_v}\right)\right) - \frac{P_{mp,STC}}{Volt_{mp,STC}}} \quad (2.13)$$

where the subscript mp refers to maximum power operation.

Given the fact that the PV modeling is developed for a domestic application, an array of modules will be used. By assuming that the array consists of a number of parallel $N_{PV,p}$ and in series $N_{PV,s}$ modules the total current and voltage of the array are calculated by the following equations respectively:

$$I_{PV,array} = I_{PV,mod} * N_{PV,p} \quad (2.14)$$

$$Volt_{PV,array} = V_{PV,mod} * N_{PV,s} \quad (2.15)$$

The aforementioned constants for the PV module are listed on Table 2.2 which follows:

Table 2.2 *DualSun characteristic constants [47]*

Parameter	Value	Unit
N_s	60	—
c_{ideal}	1.2	—
$I_{sc,STC}$	9.30	A
μ_{sc}	$4.8 * 10^{-4}$	A/K
$Volt_{oc,STC}$	38.88	V
ε_g	$1.7944 * 10^{-19}$	J
R_s	0.19	Ω
$Volt_{mp,STC}$	31.95	V
$I_{mp,STC}$	8.77	A
$P_{mp,STC}$	280	W
Dimensions	1677x990x45	mm

By executing the aforementioned model of Bellia et al [43], the $I - Volt$ and $P - Volt$ characteristics can be determined for each set of solar irradiance and ambient conditions, as it is depicted in Figure 2.1 and Figure 2.2 respectively.

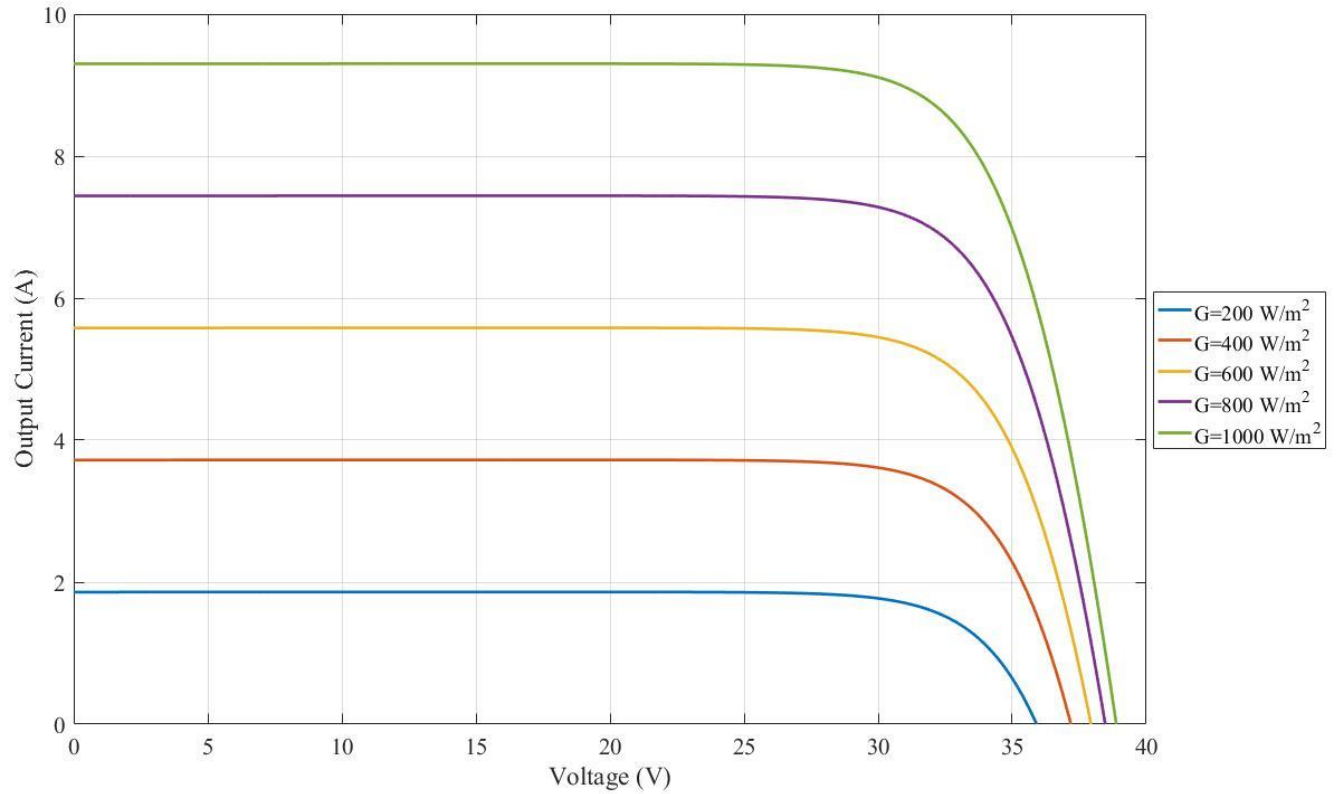


Figure 2.1 *I-Volt Characteristic curve at STC*

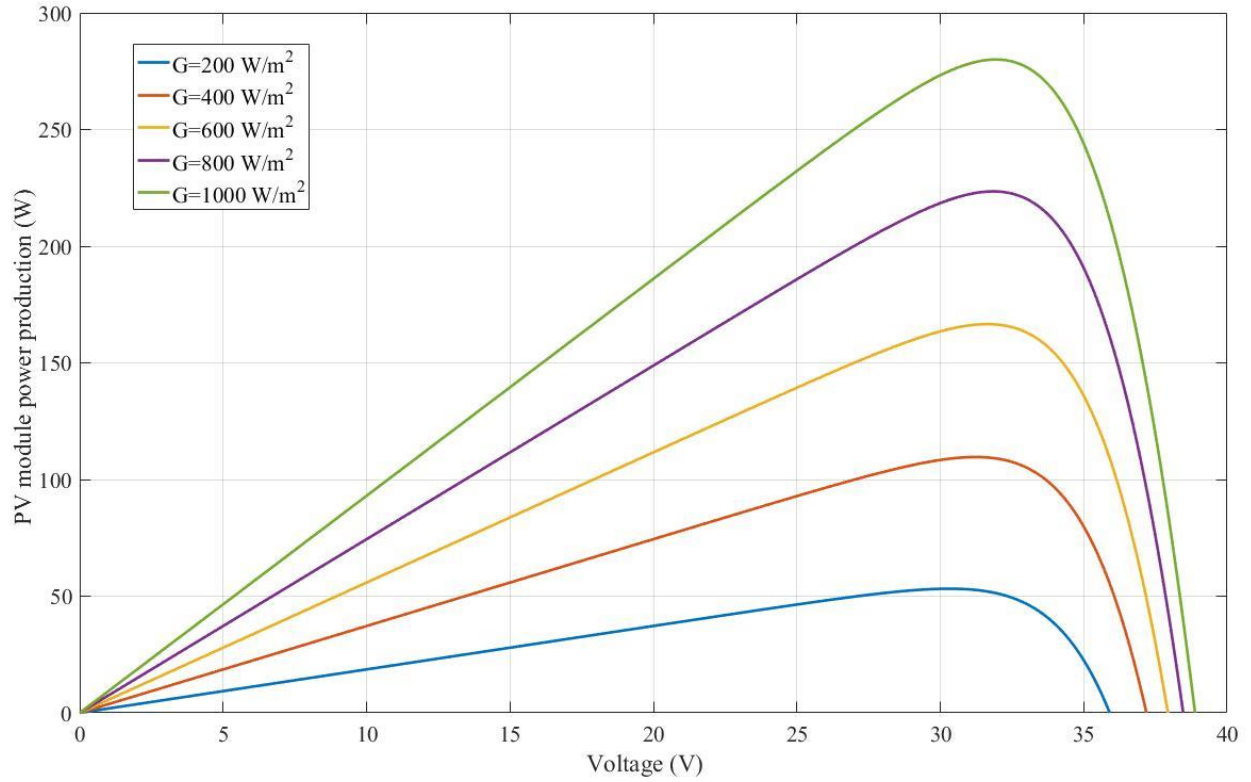


Figure 2.2 *P-Volt characteristic curve at STC*

From the two figures listed above it is apparent that with high solar irradiance, the output current and thus the power production are increased. The maximum power output is observed when the voltage of the short circuit equals to $Volt_{sc} = Volt_{mp,STC} = 31.95\text{ V}$.

By estimating the PV cell temperature through equation (2.8) and the maximum hourly power output by using the Bellia model for each location, the following figures (Figure 2.3-Figure 2.12) are designed. The hourly power output is measured in W/m^2 , as at this point the total surface area of the PVT collectors is not determined. From these figures it is concluded that the PV cell temperature is relatively higher than the ambient and the maximum values of temperature and power production are observed during summer as the solar irradiance is high and close to standard test conditions.

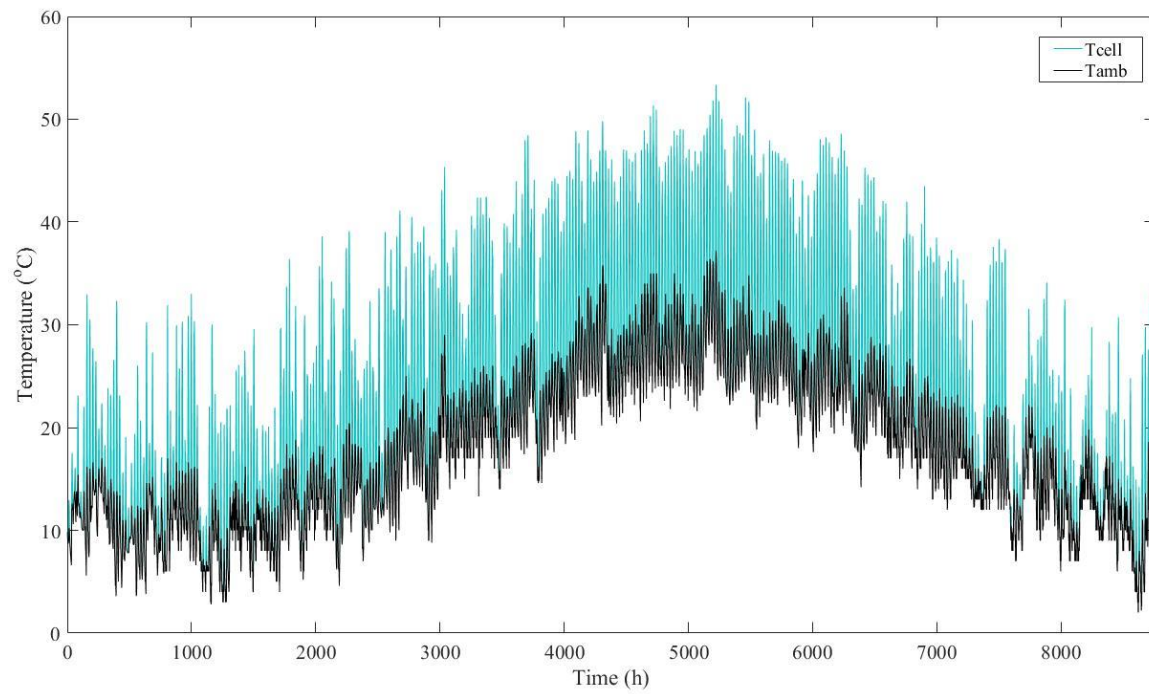


Figure 2.3 *PV cell and ambient temperature in Athens*

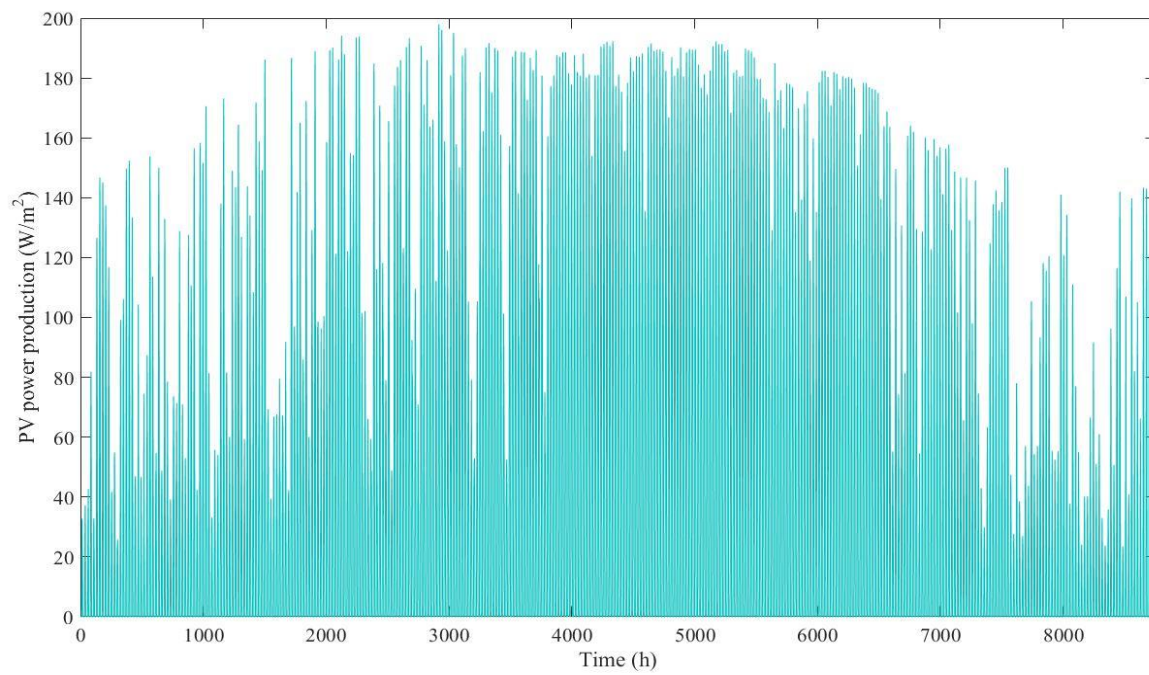


Figure 2.4 *PV power production in Athens*

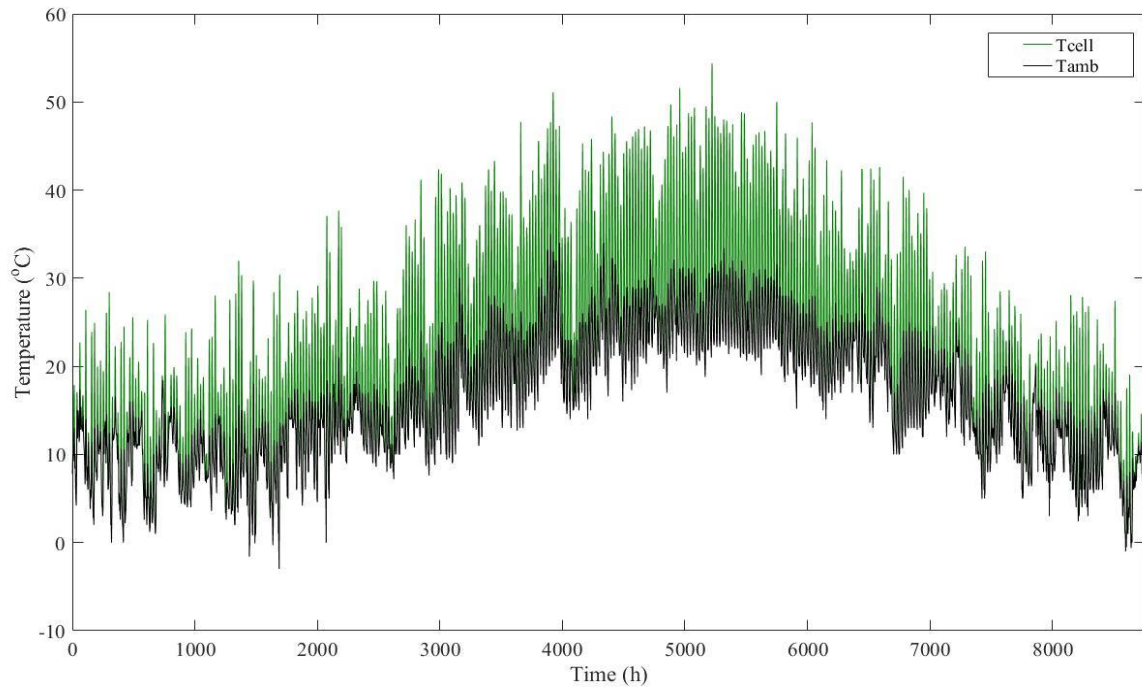


Figure 2.5 *PV cell and ambient temperature in Naples*

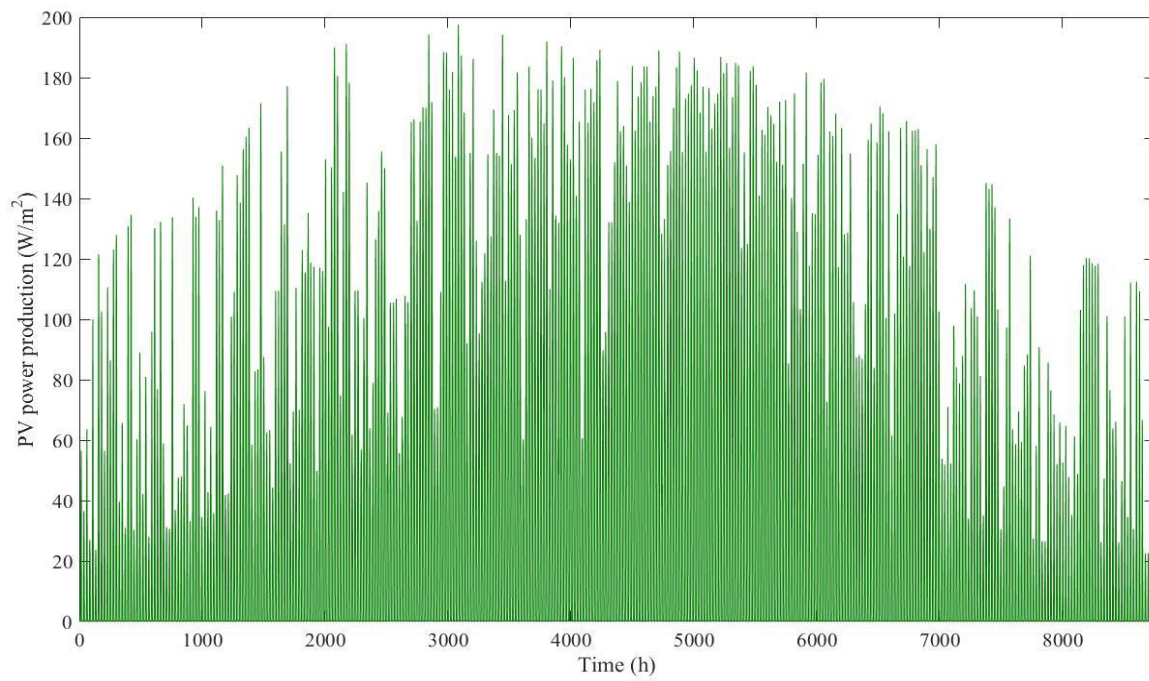


Figure 2.6 *PV power production in Naples*

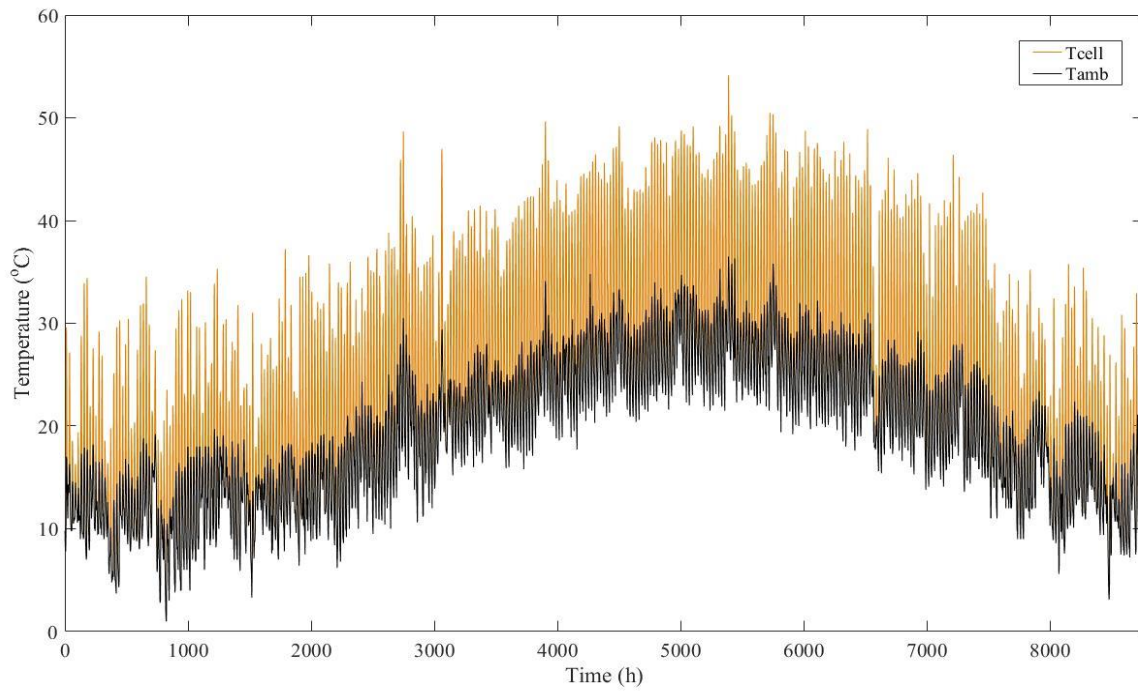


Figure 2.7 *PV cell and ambient temperature in Larnaca*

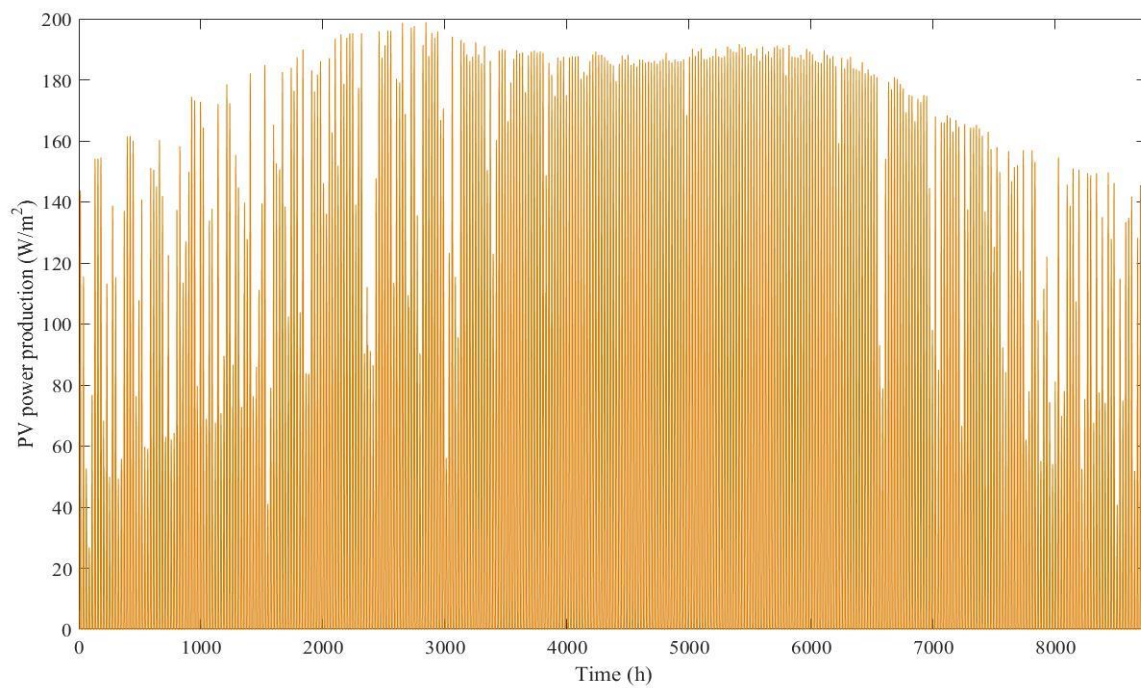


Figure 2.8 *PV power production in Larnaca*

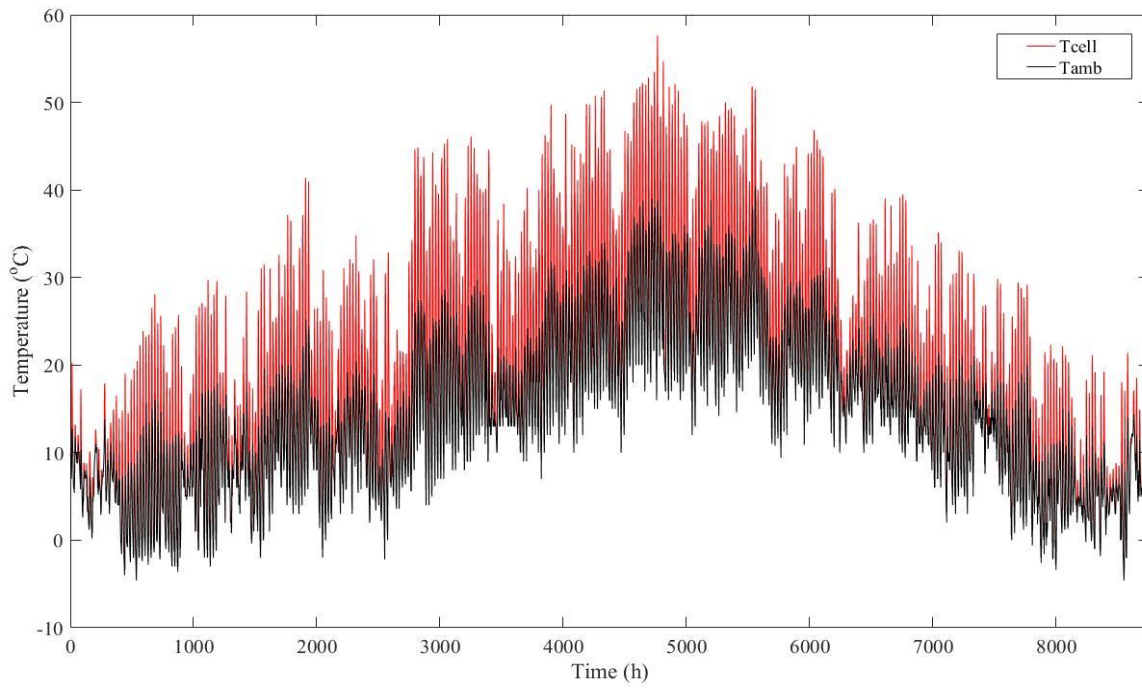


Figure 2.9 *PV cell and ambient temperature in Madrid*

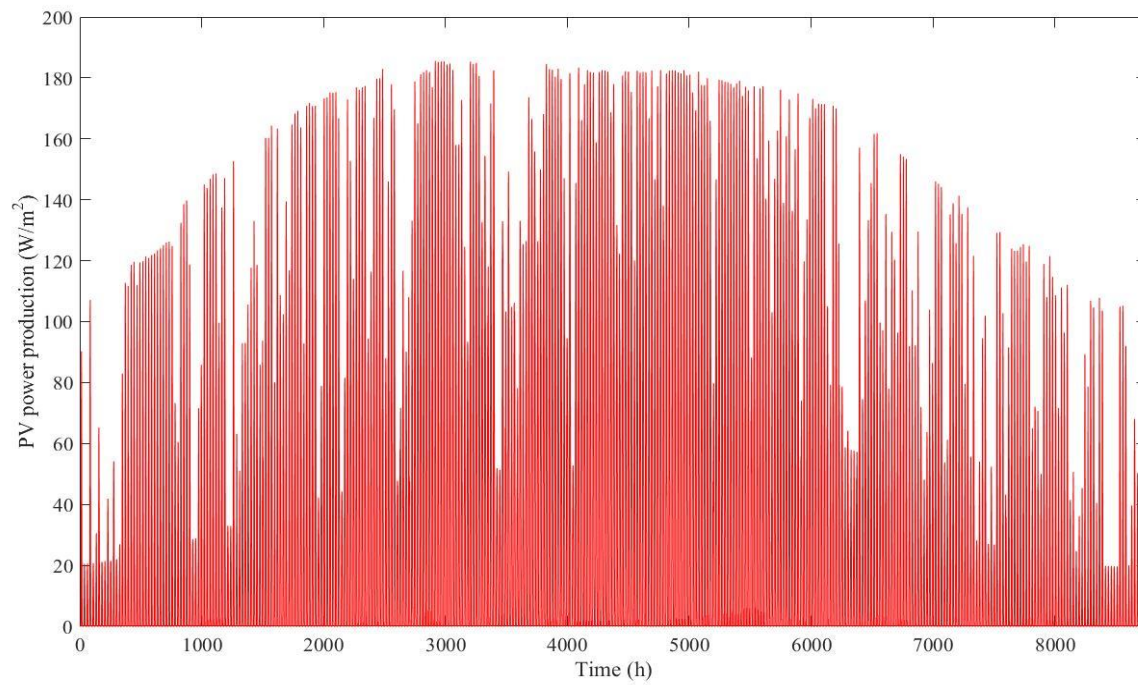


Figure 2.10 *PV power production in Madrid*

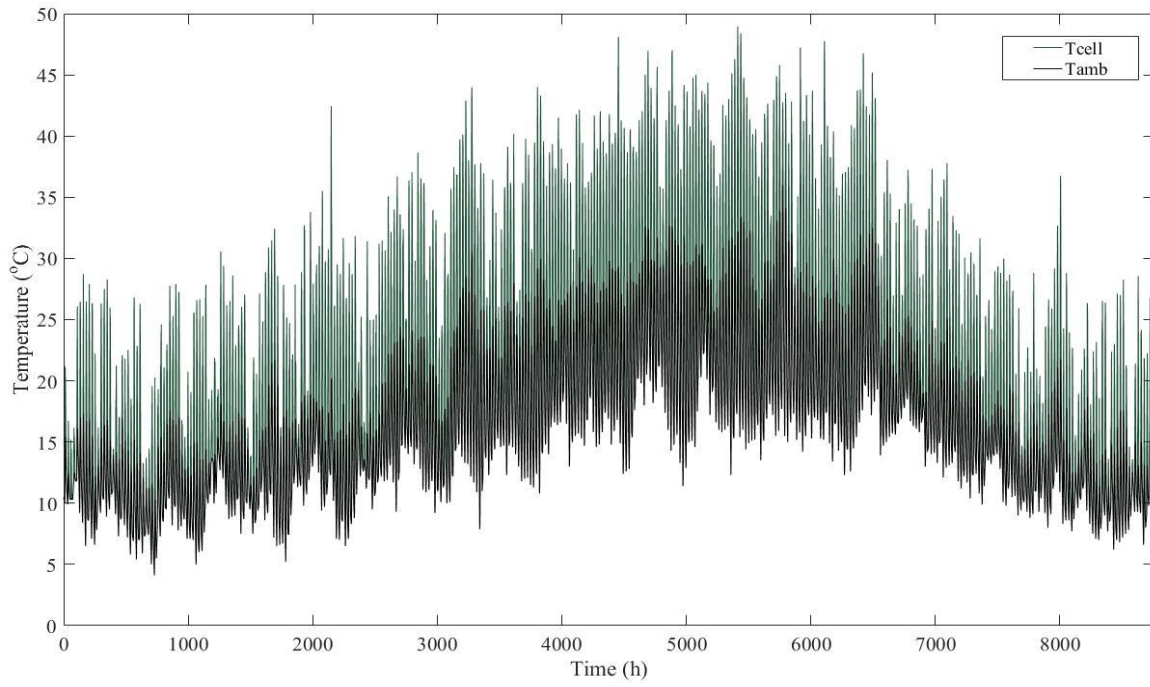


Figure 2.11 *PV cell and ambient temperature in Lisbon*

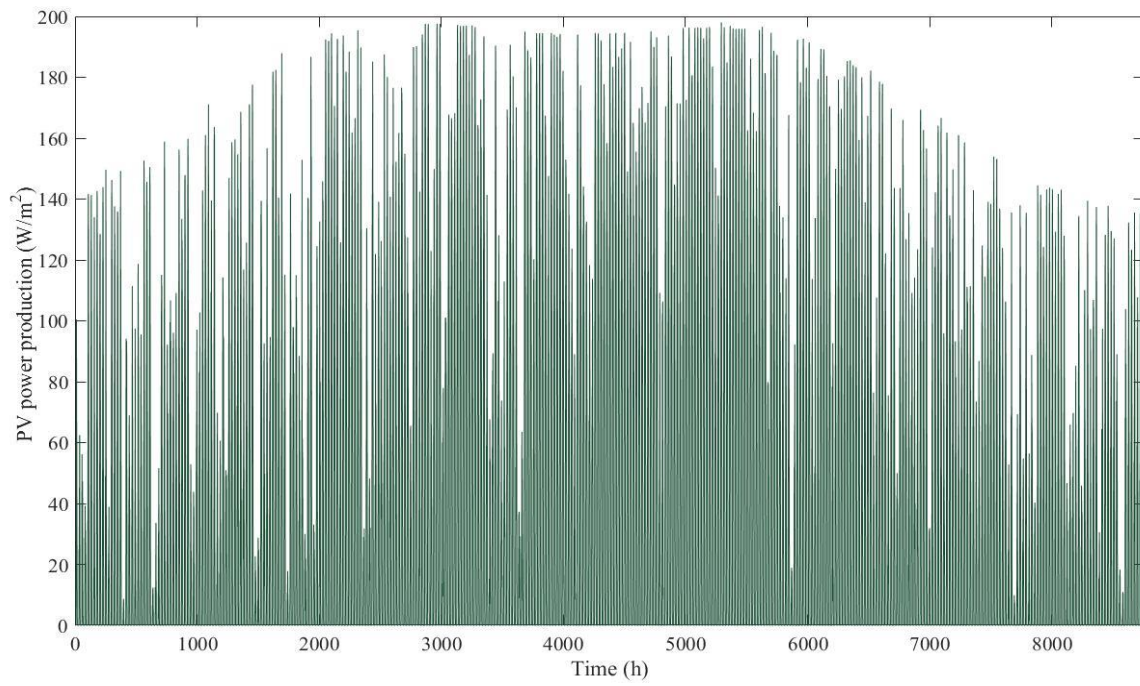


Figure 2.12 *PV power production in Lisbon*

2.2 Thermal Collector Modeling

The first step towards the modeling of the thermal component of the PVT collectors is the calculation of its efficiency. For this purpose, the following equation is used:

$$\eta_{col} = a_0 - a_1 * \left(\frac{T_{col} - T_{amb}}{G_T} \right) - a_2 * G_T * \left(\frac{T_{col} - T_{amb}}{G_T} \right)^2 \quad (2.16)$$

where T_{col} is taken equal to the outlet temperature of the collector, T_{amb} is the ambient temperature, G_T is the total incline solar irradiance on the PVT module, a_0 is the optical efficiency of the collector and a_1 and a_2 are the heat loss coefficients of the collector. According to DualSun [47] the values of these coefficients are the following:

$$a_0 = 0.472$$

$$a_1 = 9.1 \text{ W/Km}^2$$

$$a_2 = 0 \text{ W/K}^2\text{m}^2$$

In Figure 2.13 the efficiency of the thermal component of the PVT module is depicted as a function of the temperature of its working fluid in STC conditions ($T_{amb} = 25^\circ\text{C}$, $G_T = 1000 \text{ W/m}^2$). This efficiency is very low compared to that of thermal collectors, as the PV module absorbs most of the solar radiation and heat for electricity production.

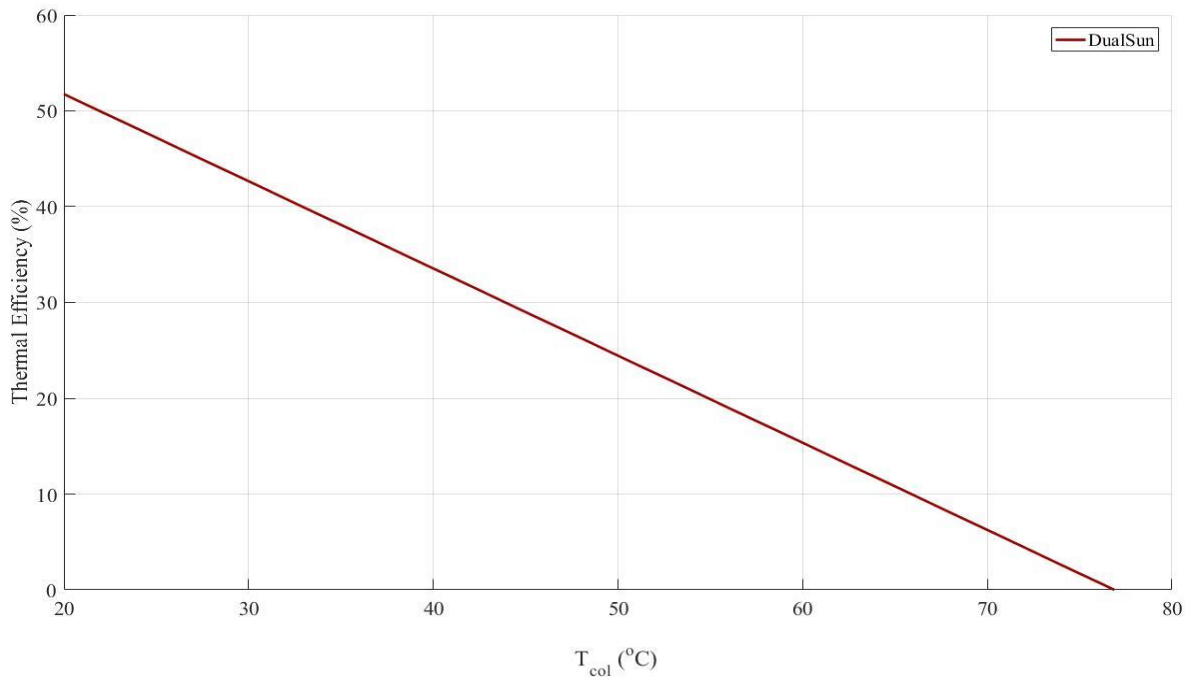


Figure 2.13 Efficiency of the thermal component of the PVT as a function of its temperature

According to equation (2.16), in order to estimate the collector's efficiency, the outlet temperature of the collector $T_{col,out}$ should be known. Nevertheless, this temperature is the main output parameter needed from the modeling of the thermal collectors. Thus, an initial guess value is assumed ($T_{col,out} = T_{col,in}$) and the collector's temperature is defined after iterations. Within every loop, the efficiency of the collector is estimated through equation (2.16) with the guessed value as an input. Then, the heat absorbed by the working fluid can be calculated as follows:

$$\dot{Q}_{col} = \eta_{col} * A_{col} * G_T \quad (2.17)$$

Hence, the temperature of the working fluid exiting the collector can be calculated from the following equation:

$$T_{col,out} = T_{col,in} + \frac{\dot{Q}_{col}}{\dot{m}_{col} * c_{p,T_{col,in}}} \quad (2.18)$$

According to DualSun [47] the mass flow rate of the collector per square meter is steady and equal to:

$$\dot{m}_{col,m^2} = 0.0336 \text{ kg/sm}^2$$

This procedure is terminated when the relative error between the outlet temperature of the collector and the guessed temperature is within an acceptable range. This range is defined as following:

$$error = \left| \frac{T_{col,out} - T_{guess}}{T_{guess}} \right| < 0.0075 \quad (2.19)$$

If this condition is not met, the guessed value is increased by a step equal to 0.02°C until the error is lower than the restriction.

2.3 Storage Tank Modeling

The variation of solar irradiance throughout the day as well as the mismatch between the availability of solar excess and the heat consumption make the use of a storage tank a necessity for the utilization of solar energy. The installation of a storage tank leads to the minimization of energy losses to the environment and a better management of the thermal content of the working fluid [48]. Moreover, for the examined application, where the coupling of an ORC with PVT modules is considered, the implementation of a storage tank results into a more stable operation of the ORC as it absorbs the energy spikes due to ambient conditions. The selection of the thermal energy storage depends on the storage period and capacity, the economic viability and the operating conditions. For a small application, as the one examined in this thesis, a storage tank suffices as the storage period is small and it is cost effective [49].

The modeling of the storage tank is based on the assumption of a number of mixing zones within the tank, each and every one of which has a uniform temperature. An energy balance is then applied to each zone in order to model the mass and heat transfer within its boundaries. Due to the fact that the storage tank model will be implemented for hourly weather data, an implicit method of discretization, which enhances the system solver's stability, is used.

The storage tank was decided to be divided into a total number of $n = 20$ mixing zones as this was the minimum number of elements to ensure high accuracy of the model by combining low computational cost.

For a number of $n = 20$ mixing zones within the storage tank and for hourly time intervals ($\Delta t = 3600s$) the following energy balances must be satisfied [50]. The first mixing zone (element) refers to the top of the storage tank, where the working fluid exits the PVT collectors and enters the ORC evaporator, while the last element refers to the bottom of the storage tank, where the working fluid exits the evaporator of the ORC and enters the circuit of the collectors. A visual presentation of the aforementioned mixing zones is depicted at Figure 2.14.

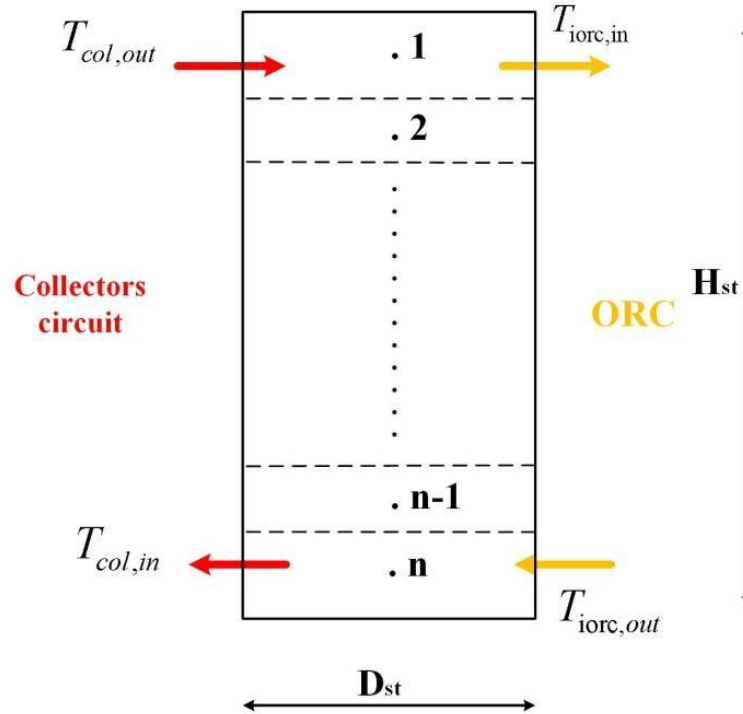


Figure 2.14 Schematic of the storage tank's mixing zones [48]

➤ Element n_1 :

$$\frac{Mass_{st}}{n} c_p \frac{T_{st}(t, 1) - T_{st}(t - 1, 1)}{\Delta t} = \dot{m}_{col} c_p (T_{col,out} - T_{st}(t, 1)) + \dot{m}_{iorc} c_p (T_{st}(t, 2) - T_{st}(t, 1)) - U_l A_{st}(1) (T_{st}(t, 1) - T_{amb}) \quad (2.20)$$

➤ Elements $n_j, j = 2: 19$:

$$\frac{Mass_{st}}{n} c_p \frac{T_{st}(t, j) - T_{st}(t - 1, j)}{\Delta t} = \dot{m}_{col} c_p (T_{st}(t, j - 1) - T_{st}(t, j)) \\ + \dot{m}_{iorc} c_p (T_{st}(t, j + 1) - T_{st}(t, j)) - U_l A_{st}(j) (T_{st}(t, j) - T_{amb}) \quad (2.21)$$

➤ Element n_{20} :

$$\frac{Mass_{st}}{n} c_p \frac{T_{st}(t, 20) - T_{st}(t - 1, 20)}{\Delta t} = \dot{m}_{col} c_p (T_{st}(t, 19) - T_{st}(t, 20)) \\ + \dot{m}_{iorc} c_p (T_{orc,out} - T_{st}(t, 20)) - U_l A_{st}(20) (T_{st}(t, 20) - T_{amb}) \quad (2.22)$$

where the heat loss coefficient of the storage tank is assumed to be equal to $U_l = 0.5 \text{ W/m}^2\text{K}$ according to Bellos et al. [51]. Moreover, the total mass of the storage tank can be calculated from its volume capacity as follows:

$$Mass_{st} = \rho_{wf} * Vol_{st} \quad (2.23)$$

Furthermore, the mass flow rate of the hot stream of the evaporator of the ORC is taken equal to $\dot{m}_{iorc} = 0.3 \text{ kg/s}$ throughout the whole study. Finally, the surface of the mixing zones is calculated through the following equations:

➤ Elements n_1, n_{20} :

$$A_{st}(1) = A_{st}(20) = \frac{\pi * D_{st}^2}{4} + \frac{\pi * D_{st} * H_{st}}{n} \quad (2.24)$$

➤ Elements $n_j, j = 2: 19$:

$$A_{st}(j) = \frac{\pi * D_{st} * H_{st}}{n} \quad (2.25)$$

where D_{st} is the diameter of the storage tank and H_{st} its height.

By formulating the above equations in a tabular $Ax = B$ form, the system can be implemented and solved in Matlab, using as input parameters the outlet temperatures of the solar collectors and the ORC circuit, as well as their mass flow rates \dot{m}_{col} and \dot{m}_{iorc} respectively. The inlet temperature of the hot stream of the evaporator of the ORC is assumed to be equal to the temperature of the first element of the storage tank, and the inlet temperature of the collectors is taken equal to the temperature of the last element of the storage tank.

For a fully stratified tank, the effects of buoyancy are insignificant and can be neglected [52]. Nevertheless, in the case of high-returning temperatures from the outlet of the evaporator of the ORC, the buoyancy effect may have significant impact on the accuracy of the aforementioned model. In order to avoid this problem, a node-mixing model is applied in the script of the storage tank, assuming that when the temperature of a zone is higher than that of the above zone, the two elements mix completely and reach a uniform temperature [53].

Chapter 3. Organic Rankine Cycle

The basic principles of the Organic Rankine Cycle have already been elaborated. In this chapter, the on and off-design modeling of the ORC, to be coupled with the previously developed solar collectors' circuit, is analyzed.

3.1 ORC Modeling

The ORC to be studied utilizes the thermal content of the storage tank of the PVT collectors, as aforementioned. This heat source is subsequently used so that more electrical energy is produced by the generator which is coupled with the expander of the ORC. The working fluid enters the expander at superheated state, by absorbing the heat surplus of the storage tank through the evaporator. After the expander, the working fluid enters the condenser in order to be cooled down by a cold stream of water through a flat plate heat exchanger and then goes to the feeding tank. In the end, a feeding pump, which is coupled with a motor, is used in order to increase the pressure of the working fluid and produce more work.

The thermal efficiency of the cycle is defined as the ratio of the enthalpy difference of the expander minus the enthalpy difference of the pump to the enthalpy difference of the evaporator:

$$\eta_{th} = \frac{\Delta h_{exp} - \Delta h_{pump}}{\Delta h_{evap}} \quad (3.1)$$

The net electrical production is calculated as follows:

$$P_{el,net} = P_{el,gen} - P_{el,mot} \quad (3.2)$$

where $P_{el,gen}$ is the electricity produced by the generator and $P_{el,mot}$ is the energy consumed by the motor of the pump. The net electrical efficiency is defined as:

$$\eta_{el,net} = \frac{P_{el,net}}{\dot{Q}_{evap}} \quad (3.3)$$

where \dot{Q}_{evap} is the heating load absorbed by the evaporator.

The modeling of all the components of the cycle is a procedure that needs to be followed in order to accomplish the design of the whole cycle.

3.1.1 Evaporator Modeling

There will be two different heat exchangers developed for this ORC configuration, an evaporator and a condenser. The final model selection for each category highly depends on its cost and size.

After examining various heat transfer correlations for evaporation, condensation and single phase heat transfer, the correlation of Donowski and Kandlikar [54] was selected for the calculation of Nusselt number for the single phase heat transfer:

$$Nu = 0.2875Pr^{1/3}Re^{0.78}, Re \geq 200 \quad (3.4)$$

For the single phase pressure drops, the correlation proposed by Focke et al. [55] was selected as its results were more realistic:

$$f = 5.03 + \frac{755}{Re}, \quad 90 < Re < 400 \quad (\varphi = 60^\circ)$$
$$f = 26.8Re^{-0.209}, \quad 400 < Re < 16,000 \quad (3.5)$$

As far as the evaporation is concerned, the most moderate correlation proposed for the calculation of Nusselt number is the one by Yan and Lin [56] :

$$Nu = 19.26 * Re_L^{0.5} * Bo_{eq}^{0.3} * Pr_L^{\frac{1}{3}}, \quad 2,000 < Re_{eq} < 10,000 \quad (3.6)$$

while for the estimation of the respective pressure drops, the correlation proposed by Hsieh and Lin [57] gives the most average results:

$$f = 6.1 * 10^4 * Re_{eq}^{-1.25} \quad (3.7)$$

For the case of the condenser, the most appropriate correlation for the estimation of Nusselt number was the one proposed by Thonon et al. [58], while for the calculation of pressure drop the one proposed by Yan et al. [59] :

$$Nu = 0.5427 * \frac{\lambda}{D_h} * Re^{0.653} * Re_{eq}^{-0.76} * Pr_L^{\frac{1}{3}} \quad (3.8)$$

$$f = 94.75 * Re_{eq}^{-0.0467} * Re^{-0.4} * Bo^{0.5} * p_{red}^{0.8}, 500 < Re < 1000 \text{ and } 60 \leq G \leq 120 \quad (3.9)$$

The hot side of the evaporator refers to the water/glycol mix of the solar circuit, while the cold side refers to the ORC's working fluid. The properties for both streams are calculated using CoolProp. For the case of water/glycol mix, due to the low concentration of the glycol, its effect was considered insignificant and thus the thermodynamic calculations for the hot side of the evaporator were executed with water as its fluid.

A function was developed to calculate the geometry of the flat plate evaporator in order to achieve the required heat duty. According to DualSun [47] the maximum temperature of water is $T_{hs} = 80^\circ\text{C}$ and its pressure is equal to $p_{hs} = 1.2 \text{ bar}$.

For the initialization of the sizing calculations, the function requires as input data the inlet state of both streams (temperature, pressure and mass flow rate). Moreover, another input data required is the output state of the ORC's working fluid. Then, through an energy balance, the output state of the hot stream may also be estimated. Four models of flat plate heat exchangers developed by Alfa Laval were examined for this application. Their technical characteristics are listed on Table 3.1 that follows.

Table 3.1 *Technical characteristics of examined flat plate heat exchangers for the evaporator*

Model	Port diameter D_p (m)	Vertical plate length L_p (m)	Horizontal distance between nozzles B_p (m)	Min-Max number of plates $N_{min}-N_{max}$	Max flow rate \dot{m} ($\frac{kg}{s}$)
AC30EQ	0.02	0.269	0.095	4-120	8.8
AC70X	0.02	0.466	0.111	4-124	14.0
AC112	0.02	0.519	0.191	10-300	51.0
CB200	0.04	0.624	0.324	10-230	128.0

Furthermore, for all the aforementioned models, the following typical plate dimensions were selected in order to carry out the heat transfer analysis as listed on Table 3.2.

Table 3.2 *Typical flat plate heat exchangers' dimensions*

	Number of Passes N_p	Plate thickness t_{pl} (mm)	Chevron angle ϕ' (°)	Pitch pit (mm)	Plate amplitude a_{pl} (mm)	Corrugation pitch Λ (mm)
Value	1	0.7	60	2.5	1	7

In Figure 3.1 a sketch of Alfa Laval's model AC30EQ is depicted, where the inlet and outlet of both streams are shown as well as some geometrical dimensions of the exchanger.

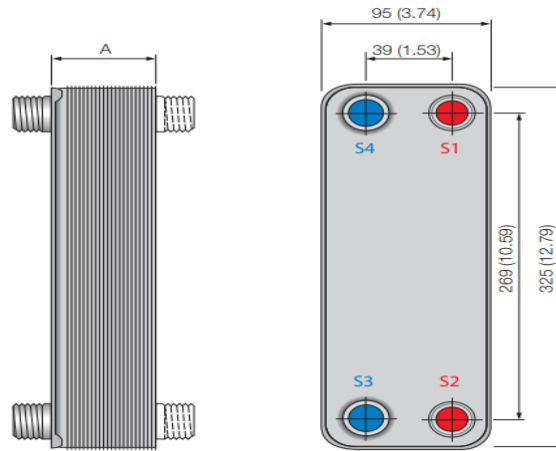


Figure 3.1 *Sketch of Alfa Laval's model AC30EQ [60]*

To compare the heat transfer surface calculated with the heat transfer analysis and the one provided for a specific number of plates, the heat transfer area of one plate without taking the corrugations into account and the heat transfer area taking them into account must be calculated.

$$A_{ref} = B_p * L_p \quad (3.10)$$

$$A_p = \Phi * A_{ref} \quad (3.11)$$

where Φ is the enlargement factor calculated by the following equations:

$$\Phi = \frac{1}{6} \left(1 + \sqrt{1 + X^2} + 4 \sqrt{1 + \frac{X^2}{2}} \right) \quad (3.12)$$

$$X = \frac{2\pi\alpha_{pl}}{\Lambda} \quad (3.13)$$

Moreover, the hydraulic diameter is calculated by the following equation:

$$D_h = 4 \frac{\alpha_{pl}}{\Phi} \quad (3.14)$$

The mass velocity per stream is then calculated:

$$G_{hs,ch} = \frac{\dot{m}_{hs}}{N_{cp}A_{ch}} \quad (3.15)$$

$$G_{cs,ch} = \frac{\dot{m}_{cs}}{N_{cp}A_{ch}} \quad (3.16)$$

where \dot{m}_{hs} is the mass flow rate of the hot stream, \dot{m}_{cs} is the mass flow rate of the cold stream, N_{cp} is the number of channels per pass and A_{ch} is the channel surface equal to:

$$A_{ch} = 2 * \alpha_{pl} * B_p \quad (3.17)$$

For the heat transfer calculations, three separate zones were considered: a preheating zone where the subcooled liquid turns into saturated liquid, the evaporation zone where it turns into saturated vapor and the superheating zone where it turns into superheated vapor. Based on the fact that for the preheating and superheating zone single phase heat transfer analysis was used, these zones were solved as a single element. On the other hand, the evaporation zone was discretized and solved in 10 consecutive elements as the heat transfer rate is highly depending on the quality of the liquid. The assumption of equal increase in the cold stream's quality within each element was made.

The analysis of each zone is consequently elaborated.

I. Preheating Zone

The preheating zone was solved as a single element. Thus, the inlet conditions of the cold stream are equal to the inlet conditions of the whole evaporator, while its outlet state corresponds to the saturated liquid state. The outlet state of the hot stream is equal to the outlet conditions of the evaporator, thus it is also known. The inlet conditions of the hot stream can be then calculated with a simple energy balance as the mass flow rates for both streams are known. The pressures for both streams were considered to be equal to the heat exchanger function's inputs.

After calculating the mean preheating zone's temperature on both sides, $\bar{T}_{hs,pre}$ and $\bar{T}_{cs,pre}$, the mean temperature of the plate can be calculated:

$$\bar{T}_{pl,pre} = \frac{\bar{T}_{hs,pre} + \bar{T}_{cs,pre}}{2} \quad (3.18)$$

Then the mean wall temperatures are calculated:

$$\bar{T}_{wall,hs} = \frac{\bar{T}_{hs,pre} + \bar{T}_{pl,pre}}{2} \quad (3.19)$$

$$\bar{T}_{wall,cs} = \frac{\bar{T}_{cs,pre} + \bar{T}_{pl,pre}}{2} \quad (3.20)$$

The logarithmic mean temperature is then calculated:

$$\Delta T_{lm} = \frac{(T_{hs,in,pre} - T_{cs,out,pre}) - (T_{hs,out,pre} - T_{cs,in,pre})}{\ln \left(\frac{T_{hs,in,pre} - T_{cs,out,pre}}{T_{hs,out,pre} - T_{cs,in,pre}} \right)} \quad (3.21)$$

The calculation of the Prandtl number is made with the assistance of the CoolProp database for the respective mean condition. The calculation of Reynolds numbers follows:

$$Re_{hs} = \frac{G_{hs,ch} * D_h}{\mu_{hs}} \quad (3.22)$$

$$Re_{cs} = \frac{G_{cs,ch} * D_h}{\mu_{cs}} \quad (3.23)$$

The hot side heat transfer coefficient is calculated by the following equation:

$$a_{hs,pre} = \frac{Nu_{hs} * \lambda_{hs}}{D_h} \quad (3.24)$$

where Nu_{hs} is calculated by Donowski and Kandlikar [54] equation as aforementioned and λ_{hs} is the thermal conductivity of the hot stream's liquid.

The cold side heat transfer coefficient is calculated by the following equation:

$$a_{cs,pre} = \frac{Nu_{cs} * \lambda_{cs}}{D_h} \quad (3.25)$$

where Nu_{cs} is calculated by Donowski and Kandlikar [54] equation as aforementioned and λ_{cs} is the thermal conductivity of the ORC's working fluid.

Finally, the overall heat transfer coefficient for the preheating zone is equal to:

$$U_{pre} = \frac{1}{\frac{1}{a_{hs,pre}} + \frac{1}{a_{cs,pre}} + \frac{t_{pl}}{\lambda_{wall}} + R_{f,cs} + R_{f,hs}} \quad (3.26)$$

where $R_{f,cs}$ and $R_{f,hs}$ refer to the fouling resistances of the cold and hot side stream respectively and they are equal to $R_{f,cs} = R_{f,hs} = 0.00017 \frac{Km^2}{W}$ and $\lambda_{wall} = 16.2 W/mK$ is the thermal conductivity of the wall.

Eventually, the required heat transfer surface can be calculated from the following equation:

$$A_{req,pre} = \frac{\dot{Q}_{pre}}{\Delta T_{lm} * U_{pre}} \quad (3.27)$$

where \dot{Q}_{pre} is the heating load of the preheating zone.

The pressure drop of the single phase hot side is calculated by the equation proposed by Focke et al. [55] as aforementioned:

$$\Delta p_{hs,pre} = \frac{f * L_p}{D_h} * \frac{\rho_{hs,pre} * v_{hs,pre}^2}{2} \quad (3.28)$$

where $\rho_{hs,pre}$ is the density of the hot stream fluid, $v_{hs,pre}$ is the mean velocity of the hot side in the preheating zone calculated from the next equation:

$$v_{hs,pre} = \frac{G_{hs,ch}}{\rho_{hs,pre}} \quad (3.29)$$

and f is the friction factor calculated by equation (3.5).

Following the same procedure, the pressure drop for the cold side $\Delta P_{cs,pre}$ is also calculated.

II. Evaporation Zone

As aforementioned, the evaporation zone is discretized in 10 elements (*iter*) for increased accuracy. In each element, an equal increase of the quality of the working fluid is considered, thus the inlet and outlet conditions of the cold stream were easily calculated for each element. The inlet of the cold stream in the evaporation zone is equal to its outlet from the preheating zone,

while the outlet of the hot stream from the evaporation zone is assumed to be equal to its inlet in the preheating zone. A schematic diagram of the evaporation zone is depicted at Figure 3.2.

The inlet enthalpy of the hot stream for each element (j) can be calculated by an energy balance, starting from the first element:

$$h_{hs,in}(j) = h_{hs,out}(j) + \frac{\dot{m}_{cs}}{\dot{m}_{hs}} (h_{cs,out}(j) - h_{cs,in}(j)) \quad (3.30)$$

Since all the enthalpies for each element have been determined, the respective temperatures can be calculated by using CoolProp as the pressures are known. This means that the calculation of the mean logarithmic temperature is also feasible via equation (3.21). Then the Prandtl number for each stream is calculated with CoolProp and the Reynolds number is determined similarly as in the preheating zone with equations (3.22 – 3.23). As the hot stream is undergoing a single phase cooling process, equations (3.4) and (3.24) can be used for the calculation of the hot side heat transfer coefficient for each element in the evaporation zone $a_{hs,evap}(j)$.

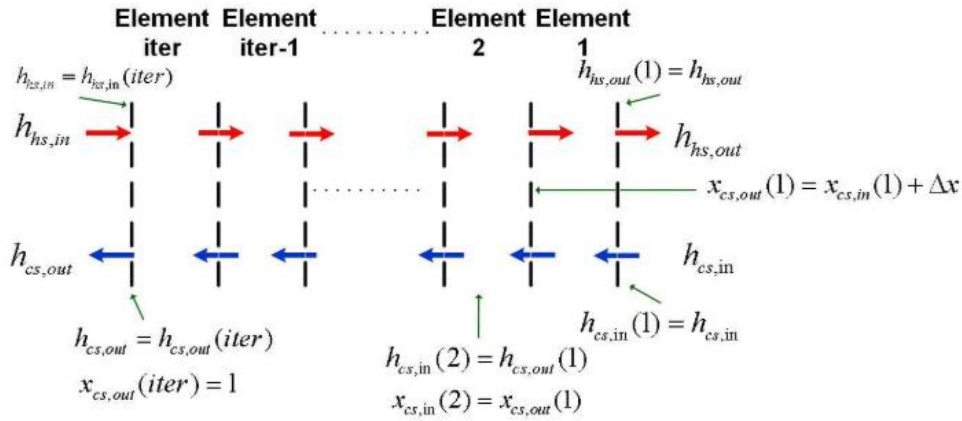


Figure 3.2 Schematic diagram of the discretized evaporation zone [48]

Nevertheless, the cold stream undergoes a two phase heating process. Hence, the Nusselt number for the cold stream in the evaporation zone is calculated with the correlation proposed by Yan and Lin [56] via equation (3.6). The boiling number of the correlation is equal to:

$$Bo_{eq} = \frac{q_{flux}}{G_{cs,ch,eq} * h_{fg}} \quad (3.31)$$

where $G_{cs,ch,eq}$ is the equivalent mass flow rate per m^2 per channel and calculated as follows:

$$G_{cs,ch,eq} = G_{cs,ch} * \left(1 - x + x \left(\frac{\rho_L}{\rho_G} \right)^{\frac{1}{2}} \right) \quad (3.32)$$

with x to be the mean quality of the stream, ρ_L the density of the saturated liquid at the examined pressure and ρ_G the density of the saturated gas at the same pressure

and the vaporization enthalpy h_{fg} of each element equals to:

$$h_{fg}(j) = h_{cs,out}(j) - h_{cs,in}(j) \quad (3.33)$$

The Reynolds number and the cold side heat transfer coefficient are then calculated by the following equations:

$$Re_L = \frac{G_{cs,ch} * D_h}{\mu_{cs,L}} \quad (3.34)$$

$$a_{cs,evap}(j) = \frac{Nu_{cs}(j) * \lambda_{cs,L}}{D_h} \quad (3.35)$$

Finally, the overall heat transfer coefficient and the required heat transfer surface for each element of the evaporation zone are calculated:

$$U_{evap}(j) = \frac{1}{\frac{1}{a_{hs,evap}(j)} + \frac{1}{a_{cs,evap}(j)} + \frac{t_{pl}}{\lambda_{wall}} + R_{f,cs} + R_{f,hs}} \quad (3.36)$$

$$A_{req,evap}(j) = \frac{\dot{Q}_{evap}(j)}{\Delta T_{lm} * U_{evap}(j)} \quad (3.37)$$

The total heat transfer surface of the evaporation zone is equal to the sum of the surface of each element.

The pressure drop of the hot stream is calculated for each element through the equation (3.28). For the cold stream, the correlation proposed by Hsieh and Lin [57] is used, in which the friction factor is calculated with the equation (3.7) and the two-phase drop is determined as follows:

$$\Delta p_{cs,evap}(j) = \frac{f * L_p}{D_h} * \frac{G_{cs,ch,eq}^2}{\rho_L} \quad (3.38)$$

The total pressure drop of both streams is equal to the sum of pressure drop of each and every element.

III. Superheating Zone

The superheating zone is calculated as a single element, like the preheating zone, since on both sides single phase heat transfer takes place. The inlet of the cold stream is equal to the outlet of the evaporation zone, while the outlet is equal to the outlet of the cold stream from the evaporator. As far as the hot stream is concerned, its inlet conditions are equal to its storage tank conditions, while its outlet can be easily calculated by a simple energy balance.

Since all enthalpies are known, the temperatures for each stream can be calculated, as well as the mean logarithmic temperature from equation (3.21). Then, the Prandtl number is determined with the assistance of CoolProp and the Reynolds numbers for the hot and cold stream are calculated from the equations (3.22) and (3.23) respectively. For the calculation of the Nusselt number, the Donowski and Kandlikar [54] correlation is used and the hot and cold side heat transfer coefficients are determined through the equations (3.24) and (3.25) respectively.

Finally, the overall heat transfer coefficient and the required heat transfer surface for the superheating zone are calculated:

$$U_{superheat} = \frac{1}{\frac{1}{a_{hs,superheat}} + \frac{1}{a_{cs,superheat}} + \frac{t_{pl}}{\lambda_{wall}} + R_{f,cs} + R_{f,hs}} \quad (3.39)$$

$$A_{req,superheat} = \frac{\dot{Q}_{superheat}}{\Delta T_{lm} * U_{superheat}} \quad (3.40)$$

The calculation of the pressure drop for both streams are calculated by applying the same method as in preheating zone, the Focke et al. [55] correlation.

IV. Overall Calculations

The combination of the 3 zones results in the sizing of the evaporator. Its total surface is equal to:

$$A_{req,tot,evap} = A_{req,pre} + \sum_{j=1}^{j=10} A_{req,evap}(j) + A_{req,superheat} \quad (3.41)$$

The pressure drop for each stream is calculated by the following expressions:

$$\Delta p_{hs,evap,tot} = \Delta p_{hs,pre} + \sum_{j=1}^{j=10} \Delta p_{hs,evap}(j) + \Delta p_{hs,superheat} + \Delta p_{hs,port} \quad (3.42)$$

$$\Delta p_{cs,evap,tot} = \Delta p_{cs,pre} + \sum_{j=1}^{j=10} \Delta p_{cs,evap}(j) + \Delta p_{cs,superheat} + \Delta p_{cs,port} \quad (3.43)$$

where the pressure drop at the ports is calculated as follows:

$$\Delta p_{port} = 0.75 * \left(\frac{G_{port}^2}{\rho_{stream,in}} + \frac{G_{port}^2}{\rho_{stream,out}} \right) \quad (3.44)$$

$$G_{port} = \frac{\dot{m}_{stream}}{A_{port}} = \frac{4 * \dot{m}_{stream}}{\pi * D_p^2} \quad (3.45)$$

The procedure for the sizing of the evaporator is the following: at the beginning a flat plate heat exchanger model is guessed (starting from the smallest one) and its number of plates is increased until the surface of the exchanger is greater than the $A_{req,evap,tot}$. If this condition is not met, the next plate exchanger is examined. Besides the surface area of the exchanger, an upper limit for the pressure drop is set, 20 kPa for both streams. If all three restrictions are overcome, the sizing of the optimal evaporator is completed.

3.1.2 Expander Modeling

For this ORC application, a scroll expander was selected as its high efficiency, durability, low cost and noise make it ideal for low power production. Moreover, two-phase operation is feasible without endangering the expander, a property which is very useful for some working fluids examined.

The modeling of the expander was based on the analysis of Lemort et al. [61]. In order to run this function, the inlet conditions of the working fluid (mass flow rate, pressure and enthalpy) need to be known as well as its outlet pressure. The inlet conditions are equal to the outlet state of the evaporator which are calculated as aforementioned. The outlet pressure of the scroll expander is equal to the condenser's pressure.

The calculation of the isentropic efficiency of the expander is based on a fitting equation proposed by Dumont et al. [62]. By taking into consideration the pressure ratio of the expander and guessing various nominal rotational speeds, the isentropic efficiency is calculated and the nominal rotational speed is taken equal to the respective value with which the highest efficiency is achieved.

Then, the nominal volumetric displacement of the expander can be calculated by the following equation:

$$\dot{V}_{exp,nom} = \frac{60 * \dot{m}}{N_{exp,nom} * ff * \rho_{exp,in}} \quad (3.46)$$

where \dot{m} is the working fluid's mass flow rate, $\rho_{exp,in}$ is its inlet state's density, N_{exp} is the nominal rotational speed of the expander in *rpm* and ff is the filling factor.

The filling factor of an expander is a function of the rotational speed and is a property of the expander's model. For the purpose of the study, experimental data from Dumont et al. [62] were used and the following equation was considered to be the best fit for these data:

$$ff = -3.85 * 10^{-12} N_{exp}^3 + 7.198 * 10^{-8} N_{exp}^2 - 5.034 * 10^{-4} N_{exp} + 2.047 \quad (3.47)$$

The system of the equations (3.46) and (3.47) is solved and the nominal volumetric displacement of the expander is estimated.

Since the isentropic efficiency of the expander is known, the outlet enthalpy of the stream can be calculated from the following equation:

$$\eta_{exp,is} = 0.95 \frac{h_{exp,in} - h_{exp,out}}{h_{exp,in} - h_{exp,out,is}} \quad (3.48)$$

where the inlet state of the stream is known, and the isentropic outlet enthalpy can be easily calculated by CoolProp as its pressure and entropy are known. For this calculation, heat losses equal to 5% of the maximum thermal work of the expander were estimated.

By considering a mediocre value for the mechanical efficiency of the expander ($\eta_{mech} = 0.95$), the produced mechanical work is calculated:

$$W_{exp} = \eta_{mech} * \dot{m} * (h_{exp,in} - h_{exp,out}) \quad (3.49)$$

3.1.3 Generator Modeling

In order to calculate the actual power output by the generator, which is coupled with the ORC's expander, it is essential to estimate the efficiency of the inverter and the generator. These efficiencies are calculated as polynomial functions of the expander's rotational speed and the power generated at the expander. These polynomials were derived from the data of Ziviani et al. [63]:

$$\eta_{gen} = b_0 + b_1 * \ln N + b_2 * (\ln N)^2 + b_3 * (\ln N)^3 + b_4 * \ln t + b_5 * (\ln t)^2 + b_6 * (\ln t)^3 + b_7 * \ln N * \ln t + b_8 * \ln N * (\ln t)^2 + b_9 * (\ln N)^2 * \ln t + b_{10} * (\ln N)^2 * (\ln t)^2 \quad (3.50)$$

$$\eta_{inv,gen} = a_0 + a_1 * \ln N + a_2 * (\ln N)^2 + a_3 * (\ln N)^3 + a_4 * \ln W + a_5 * (\ln W)^2 + a_6 * (\ln W)^3 \quad (3.51)$$

where t is referring to the torque developed in the expander's shaft and the ratios in the equations above are equal to:

$$N = \frac{N_{exp}}{N_{exp,nom}} \quad (3.52)$$

$$W = \frac{W_{exp}}{W_{exp,nom}} \quad (3.53)$$

$$t = \frac{t_{exp}}{t_{exp,nom}} = \frac{W_{exp}}{W_{exp,nom}} * \frac{N_{exp,nom}}{N_{exp}} = \frac{W}{N} \quad (3.54)$$

Since the on-design point is studied first, these three ratios are equal to 1 by default. The values of the coefficients a_i, b_i are listed on Table 3.3 that follows:

Table 3.3 Value of the generator's coefficients

	0	1	2	3	4	5	6	7	8	9	10
a_i	0.95573	0.02610	0.02423	0.01212	0.04948	0.03341	0.02274	-	-	-	-
b_i	0.89375	0.03230	-0.01918	0.01522	0.00733	-0.03171	0.02164	0.01631	0.00438	-0.04120	-0.01627

The final power output of the generator in the grid is equal to:

$$P_{el,gen} = W_{exp} * \eta_{gen} * \eta_{inv,gen} \quad (3.55)$$

3.1.4 Condenser Modeling

As aforementioned at subchapter 3.1.1, the condenser of the ORC installation is a flat plate heat exchanger, the model of which is determined by its cost and size. The cold side of the condenser is a stream of water with known inlet and outlet conditions ($T_{cs,cond,in} = 7.5^{\circ}\text{C}$, $T_{cs,cond,out} = 11.5^{\circ}\text{C}$ and $p_{cs,cond,in} = 2 \text{ bar}$) while the inlet state of the working fluid (hot side) is equal to the outlet of the expander.

For the calculation of Nusselt number for the single phase heat transfer, the correlation of Donowski and Kandlikar [54] as in equation (3.4) was used. Moreover, for the single phase pressure drops, the correlation proposed by Focke et al. [55] was selected as its results were more realistic, as shown in equation (3.5).

For the case of the two-phase heat transfer in the condenser, the most appropriate correlations for the estimation of Nusselt number and the calculation of pressure drop were the ones proposed by Thonon et al. [58] and Yan et al. [59] as aforementioned (equations 3.8 and 3.9).

For the initialization of the sizing calculations, the function requires as input data the inlet state of both streams (temperature, pressure and mass flow rate). Moreover, another input data required is the outlet temperature of the cold stream. Then, through an energy balance, the output state of the ORC's working fluid may also be estimated. Five models of flat plate heat exchangers developed by Alfa Laval were examined for this application. Their technical characteristics are listed on Table 3.4 that follows.

Table 3.4 *Technical characteristics of examined flat plate heat exchangers for the condenser*

Model	Port diameter D_p (m)	Vertical plate length L_p (m)	Horizontal distance between nozzles B_p (m)	Min-Max number of plates $N_{min} - N_{max}$	Max flow rate \dot{m} ($\frac{kg}{s}$)
CB30	0.02	0.250	0.113	4 – 150	14.0
AC30EQ	0.02	0.269	0.095	4 – 120	8.8
AC70X	0.02	0.466	0.111	4 – 124	14.0
AC112	0.02	0.519	0.191	10 – 300	51.0
CB200	0.04	0.624	0.324	10 – 230	128.0

Furthermore, for all the aforementioned models, some typical plate dimensions were selected in order to carry out the heat transfer analysis as listed on Table 3.2.

In Figure 3.3 a sketch of Alfa Laval's model CB30 is depicted, where the inlet and outlet of both streams are shown as well as some geometrical dimensions of the exchanger.

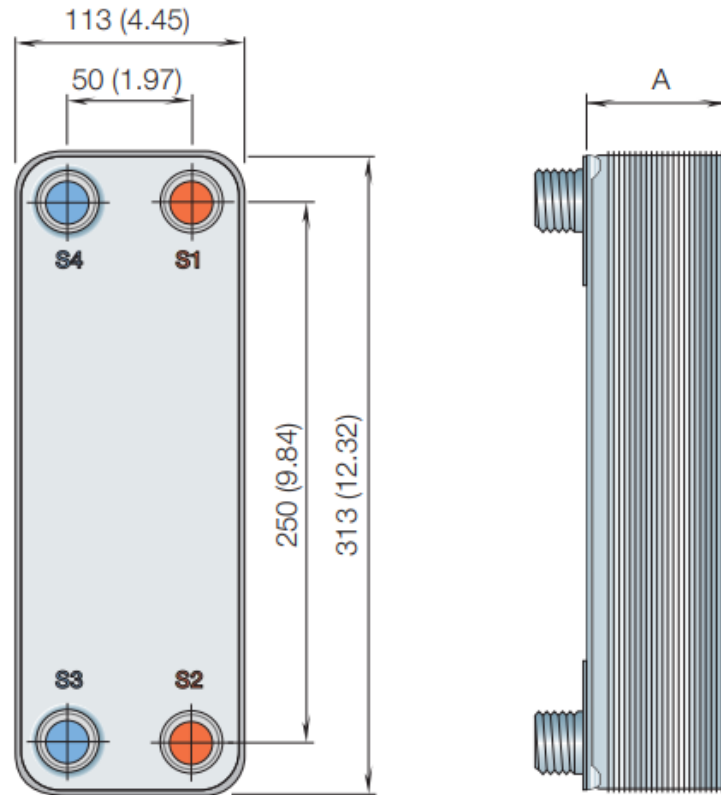


Figure 3.3 *Sketch of Alfa Laval's model CB30 [64]*

All the geometrical equations used in the case of the evaporator (equations 3.10-3.17), were also used for the sizing of the condenser, as the same commercial models were considered.

For the heat transfer calculations, three separate zones were considered: a desuperheating zone where the superheated vapor turns into saturated vapor, the condensation zone where it turns into saturated liquid and the subcooling zone where it turns into subcooled liquid. Based on the fact that for the superheating and subcooling zone single phase heat transfer analysis was used, these zones were solved as a single element. On the other hand, the condensation zone was discretized and solved in 10 consecutive elements as the heat transfer rate is highly depending on the quality of the liquid. The assumption of equal decrease in the hot stream's quality within each element was made.

The analysis of each zone is consequently elaborated.

I. Desuperheating Zone

As aforementioned, the desuperheating zone is calculated as a single element. Thus, the inlet conditions of this zone are equal to the inlet conditions of the hot stream of the condenser, while the outlet state of the hot stream corresponds to the saturated vapor state. Moreover, the outlet state of the cold stream from the desuperheating zone is equal to the outlet of the cold stream from the whole condenser. Hence, by applying an energy balance for the desuperheating zone, the inlet conditions of the cold stream are also estimated.

After calculating the mean desuperheating zone's temperature on both sides, $\bar{T}_{hs,desup}$ and $\bar{T}_{cs,desup}$, the mean plate and wall temperatures can be calculated, as well as the logarithmic mean temperature through equations (3.18 – 3.21) respectively.

The calculation of the Prandtl number is made with the assistance of the CoolProp database for the respective mean condition. The corresponding Reynolds numbers are calculated similarly as in the preheating zone by equations (3.22 – 3.23). As both streams are undergoing a single phase heat transfer process, equation (3.4) is used for the estimation of Nusselt number, while equations (3.24) and (3.25) can be used for the calculation of the hot and cold side heat transfer coefficient for both streams in the desuperheating zone ($a_{hs,desuper}$ and $a_{cs,desuper}$).

Finally, the overall heat transfer coefficient for the desuperheating zone is equal to:

$$U_{desup} = \frac{1}{\frac{1}{a_{hs,desup}} + \frac{1}{a_{cs,desup}} + \frac{t_{pl}}{\lambda_{wall}} + R_{f,cs} + R_{f,hs}} \quad (3.56)$$

where $R_{f,cs}$ and $R_{f,hs}$ refer to the fouling resistances of the cold and hot side stream respectively and they are equal to $R_{f,cs} = R_{f,hs} = 0.00017 \text{ Km}^2/\text{W}$ and $\lambda_{wall} = 16.2 \text{ W/mK}$ is the thermal conductivity of the wall.

Eventually, the required heat transfer surface can be calculated from the following equation:

$$A_{req,desup} = \frac{\dot{Q}_{desup}}{\Delta T_{lm} * U_{desup}} \quad (3.57)$$

where \dot{Q}_{desup} is the heating load of the desuperheating zone.

The pressure drop of the single phase hot side is calculated by the equation proposed by Focke et al. [55] as aforementioned:

$$\Delta p_{hs,desup} = \frac{f * L_p}{D_h} * \frac{\rho_{hs,desup} * v_{hs,desup}^2}{2} \quad (3.58)$$

where $\rho_{hs,desup}$ is the density of the hot stream fluid, $v_{hs,desup}$ is the mean velocity of the hot side in the desuperheating zone calculated from the next equation:

$$v_{hs,desup} = \frac{G_{hs,ch}}{\rho_{hs,desup}} \quad (3.59)$$

and f is the friction factor calculated by equation (3.5).

Following the same procedure for the cold side, the pressure drop for the cold side $\Delta P_{cs,desup}$ is also calculated.

II. Condensation Zone

As aforementioned, the condensation zone is discretized in 10 elements (*iter*) for increased accuracy. In each element, an equal decrease of the quality of the working fluid is considered, thus the inlet and outlet conditions of the hot stream were easily calculated for each element. The inlet of the hot stream in the condensation zone is equal to its outlet from the desuperheating zone, while the outlet of the cold stream from the condensation zone is assumed to be equal to its inlet in the desuperheating zone.

The inlet enthalpy of the cold stream for each element (j) can be calculated by an energy balance, starting from the first element:

$$h_{cs,cond,in}(j) = h_{cs,cond,out}(j) - \frac{\dot{m}_{hs}}{\dot{m}_{cs}} (h_{hs,cond,in}(j) - h_{hs,cond,out}(j)) \quad (3.60)$$

Since all the enthalpies for each element have been determined, the respective temperatures can be calculated by using CoolProp as the pressures are known. This means that the calculation of the mean logarithmic temperature is also feasible via equation (3.21). Then the Prandtl number for each stream is calculated with CoolProp and the Reynolds numbers are determined similarly as in the preheating zone with equations (3.22 – 3.23). As the cold stream is undergoing a single phase heating process, equations (3.4) and (3.25) can be used for the calculation of its heat transfer coefficient for each element in the condensation zone $a_{cs,cond}(j)$.

Nevertheless, the hot stream undergoes a two phase cooling process. Hence, the Nusselt number for the hot stream in the condensation zone is calculated with the correlation proposed by Yan et al. [59] by equation (3.8). Then the hot side heat transfer coefficient of each element can be calculated by the equation (3.24).

Finally, the overall heat transfer coefficient and the required heat transfer surface for each element of the condensation zone are calculated:

$$U_{cond}(j) = \frac{1}{\frac{1}{a_{hs,cond}(j)} + \frac{1}{a_{cs,cond}(j)} + \frac{t_{pl}}{\lambda_{wall}} + R_{f,cs} + R_{f,hs}} \quad (3.61)$$

$$A_{req,cond}(j) = \frac{\dot{Q}_{cond}(j)}{\Delta T_{lm} * U_{cond}(j)} \quad (3.62)$$

The total heat transfer surface of the condensation zone is equal to the sum of the surface of each element.

The pressure drop of the cold stream is calculated for each element through the equation (3.28). For the hot stream, the correlation proposed by Yan et al. [59] is used, in which the friction factor is calculated with the equation (3.9) and the two-phase drop is determined as follows:

$$\Delta p_{hs,cond}(j) = \frac{f * L_p}{D_h} * \frac{G_{hs,ch,eq}^2}{\rho_L} \quad (3.63)$$

The total pressure drop of both streams is equal to the sum of pressure drops of each and every element.

III. Subcooling Zone

The subcooling zone is calculated as a single element, like the desuperheating zone, since on both sides single phase heat transfer takes place. The inlet of the hot stream is equal to the outlet of the condensation zone, while the outlet is equal to the outlet of the hot stream from the whole condenser. As far as the cold stream is concerned, its inlet conditions are equal to its inlet to the condenser, while its outlet can be easily calculated by a simple energy balance.

Since all enthalpies are known, the temperatures for each stream can be calculated, as well as the mean logarithmic temperature from equation (3.21). Then, the Prandtl number is determined with the assistance of CoolProp and the Reynolds numbers for the hot and cold stream are calculated from the equations (3.22) and (3.23) respectively. For the calculation of the Nusselt number, the Donowski and Kandlikar [54] correlation is used and the hot and cold side heat transfer coefficients are determined through the equations (3.24) and (3.25) respectively.

Finally, the overall heat transfer coefficient and the required heat transfer surface for the subcooling zone are calculated:

$$U_{subcool} = \frac{1}{\frac{1}{a_{hs,subcool}} + \frac{1}{a_{cs,subcool}} + \frac{t_{pl}}{\lambda_{wall}} + R_{f,cs} + R_{f,hs}} \quad (3.64)$$

$$A_{req,subcool} = \frac{\dot{Q}_{subcool}}{\Delta T_{lm} * U_{subcool}} \quad (3.65)$$

The pressure drop for both streams is calculated by applying the same method as in desuperheating zone, the Focke et al. [55] correlation.

IV. Overall Calculations

The combination of the 3 zones results in the sizing of the condenser. Its total surface is equal to:

$$A_{req,cond,tot} = A_{req,desup} + \sum_{j=1}^{j=10} A_{req,cond}(j) + A_{req,subcool} \quad (3.66)$$

The pressure drop for each stream is calculated by the following expressions:

$$\Delta p_{hs,cond,tot} = \Delta p_{hs,desup} + \sum_{j=1}^{j=10} \Delta p_{hs,cond}(j) + \Delta p_{hs,subcool} + \Delta p_{hs,port} \quad (3.67)$$

$$\Delta p_{cs,cond,tot} = \Delta p_{cs,desup} + \sum_{j=1}^{j=10} \Delta p_{cs,cond}(j) + \Delta p_{cs,subcool} + \Delta p_{cs,port} \quad (3.68)$$

where the pressure drop of the port is calculated through equations (3.44) and (3.45).

The procedure for the sizing of the condenser is the following: at the beginning a flat plate heat exchanger model is guessed (starting from the smallest one) and its number of plates is increased until the surface of the condenser is greater than the $A_{req,cond,tot}$. If this condition is not met, the next plate exchanger is examined. Besides the surface area of the condenser, an upper limit for the pressure drop is set, 20 kPa for both streams. If all three restrictions are overcome, the sizing of the optimal condenser is completed.

3.1.5 Pump Modeling

The modeling of the ORC's pump is based on data derived from Wanner Engineering [65]. In particular the pump selected was D10 Series, a diaphragm pump as the system is designed for small scale application. In order to run this model, the inlet state of the working fluid needs to be known (mass flow rate, pressure and enthalpy), which is equal to the outlet state of the condenser, as well as the output pressure, which is equal to the evaporator's pressure.

The mechanical power consumption of the pump is calculated based on a formula provided by the manufacturer:

$$W_{mech,pump}(kW) = \frac{\dot{V}_{pump,dis} \left(\frac{lt}{min} \right) * \Delta p \text{ (bar)}}{511} + 15 \frac{N_{pump} \text{ (rpm)}}{84428} \quad (3.69)$$

where $\dot{V}_{pump,dis}$ is the volumetric flow rate of the pump at the discharge, Δp is the pressure difference and N_{pump} is the rotational speed of the pump respectively.

The volumetric flow rate is calculated by the following equation:

$$\dot{V}_{pump} = \frac{\dot{m}}{\rho_{pump}} * 60 * 10^3 \left(\frac{lt}{min} \right) \quad (3.70)$$

The rotational speed of the pump can be calculated according to the manufacturer by the following equation:

$$N_{pump} = 46.705 * \dot{V}_{pump} + 22.681 \text{ (rpm)} \quad (3.71)$$

By assuming there are no heat losses in the pump, the outlet enthalpy of the working fluid can be calculated:

$$h_{pump,dis} = h_{pump,in} + \frac{W_{mech,pump}}{\dot{m}} \quad (3.72)$$

Nevertheless, the equation (3.69) requires the volumetric flow rate of the pump at the discharge, thus an iterative method is implemented. As an initial value for the flow rate at the discharge port, the inlet state is considered. Then, the actual volumetric flow rate is estimated through equation (3.70) at the discharge port as well as the rotational speed of the pump by equation (3.71). Finally, the mechanical power consumption of the pump can be estimated through equation (3.69) and the outlet enthalpy of the working fluid through equation (3.72) and thus the entire outlet state.

In the end, the isentropic efficiency of the pump can be calculated as follows:

$$\eta_{pump,is} = \frac{h_{pump,dis,is} - h_{pump,in}}{h_{pump,dis} - h_{pump,in}} \quad (3.73)$$

3.1.6 Motor Modeling

In order to calculate the actual power consumption by the motor, which is coupled with the ORC's pump, it is essential to estimate the efficiency of the inverter and the motor. These efficiencies are calculated as polynomial functions of the pump's rotational speed and the work consumed at the pump. These polynomials were derived from the data of Ziviani et al. [63]:

$$\eta_{mot} = b_0 + b_1 * \ln N + b_2 * (\ln N)^2 + b_3 * (\ln N)^3 + b_4 * \ln t + b_5 * (\ln t)^2 + b_6 * (\ln t)^3 + b_7 * \ln N * \ln t + b_8 * \ln N * (\ln t)^2 + b_9 * (\ln N)^2 * \ln t + b_{10} * (\ln N)^2 * (\ln t)^2 \quad (3.74)$$

$$\eta_{inv,mot} = a_0 + a_1 * \ln N + a_2 * (\ln N)^2 + a_3 * (\ln N)^3 + a_4 * \ln W + a_5 * (\ln W)^2 + a_6 * (\ln W)^3 \quad (3.75)$$

where t is referring to the torque developed in the pump's shaft and the ratios in the equations above are equal to:

$$N = \frac{N_{pump}}{N_{pump,nom}} \quad (3.76)$$

$$W = \frac{W_{pump}}{W_{pump,nom}} \quad (3.77)$$

$$t = \frac{t_{pump}}{t_{pump,nom}} = \frac{W_{pump}}{W_{pump,nom}} * \frac{N_{pump,nom}}{N_{pump}} = \frac{W}{N} \quad (3.78)$$

Since the on-design point is studied first, these three ratios are equal to 1 by default. The values of the coefficients a_i, b_i are listed on Table 3.5 that follows:

Table 3.5 Value of the motor's coefficients

	0	1	2	3	4	5	6	7	8	9	10
a_i	0.95573	0.02610	0.02423	0.01212	0.04948	0.03341	0.02274	-	-	-	-
b_i	0.89375	0.03230	-0.01918	0.01522	0.00733	-0.03171	0.02164	0.01631	0.00438	-0.04120	-0.01627

The final power consumption by the motor is equal to:

$$P_{el,mot} = \frac{W_{mech,pump}}{\eta_{mot} * \eta_{inv,mot}} \quad (3.79)$$

3.2 Working Fluid Selection

As aforementioned, the selection of the working fluid for a specific application is a crucial procedure which determines the total efficiency of the cycle and its operational range, therefore defining the capability of utilizing the energy content of the available heat source. The critical temperature of the working fluid must be higher than the vapor's temperature at the outlet of the superheating zone at a subcritical ORC. Nevertheless, the difference of these temperatures should be low in order to achieve the highest thermal efficiency. Thus, the working fluids for this application should have a critical temperature $T_{crit} > 70^{\circ}\text{C}$. The upper limit for critical temperatures was considered to be $T_{crit,max} = 120^{\circ}\text{C}$. Moreover, high critical pressures should be avoided as they can be catastrophic for flat plate heat exchangers.

Furthermore, it is essential to take into consideration the environmental impact of the working fluid to be used. This impact is characterized by the depletion of the atmospheric ozone layer and the contribution of the refrigerant to global warming as already mentioned in subchapter 1.2.

Moreover, another crucial parameter to be taken into account is the safety of working fluids. The toxicity, corrosiveness and flammability of the refrigerants must be as low as possible, as shown by the ASHRAE safety group indicator.

Finally, another parameter which determines the selection of working fluids is their availability and cost for each application.

By taking into consideration all the above parameters for the selection of an ideal working fluid, the following working fluids from all organic compounds categories were examined, as shown at Table 3.6.

Table 3.6 *Examined Working Fluids and their properties*

	$T_{crit} (^{\circ}\text{C})$	$p_{crit} (\text{bar})$	ODP	GWP	ASHRAE	Cost ($\text{€}/\text{lt}$)
Propylene	91.06	45.55	0	1.8	A3	5.108 [66]
Propane	96.74	42.51	0	3.3	A3	1.079 [67]
R32	78.11	57.82	0	675	A2L	20.215[68]
R134a	101.06	40.59	0	1430	A1	32.630 [66]
R152a	113.26	45.20	0	124	A2L	4.754 [69]
R227ea	101.75	29.25	0	3220	A1	120.00 [70]
R410a	72.80	48.60	0	2088	A1	42.328 [71]
R-C318	115.23	27.78	0	10300	A1	887.065 [72]
R1234yf	94.70	33.82	0	4	A2L	101.330 [73]
R1234ze	109.37	36.36	0	6	A2L	38.434 [74]

3.3 On-Design Simulation of ORC

Since the separate models for each component of the ORC have been developed, the sizing and on-design operation of the whole cycle can be calculated.

For this purpose, as it was elaborated in the modeling of the components, the pressure of the evaporator and the condenser must be known. These values are calculated through the estimation of the pinch point of the evaporator and the condenser. Pinch point is defined as the lowest temperature difference of the hot and cold stream at the flat plate heat exchanger. In order to estimate this value, the inlet and outlet conditions of the hot stream of the evaporator and the cold stream of the condenser are known. These parameters that remain constant for all working fluids during the on-design simulation are the following:

$$T_{hs,evap,in} = 80^{\circ}\text{C}$$

$$P_{hs,evap,in} = 1.2 \text{ bar}$$

$$\dot{m}_{hs,evap} = 0.3 \text{ kg/s}$$

$$\dot{Q}_{evap} = 20 \text{ kW}$$

$$T_{cs,cond,in} = 7.5^{\circ}\text{C}$$

$$T_{cs,cond,out} = 11.5^{\circ}\text{C}$$

$$p_{cs,cond,in} = 2 \text{ bar}$$

In the case of the evaporator, the acceptable range of pinch point is set to be equal to:

$$PP_{evap} = 4.5 \pm 0.2 \text{ K}$$

For the calculation of the pinch point, an initial value of the evaporator's pressure is guessed. This initial value was set to be equal to the examined working fluid's pressure for $T_{cs,evap} = T_{hs,evap,in} - 20 \text{ K}$. Then the value of the pinch point is calculated for this pressure and the examined mass flow rate of the working fluid. If the estimated pinch point is higher than the acceptable value, the evaporator's pressure is increased and the procedure is repeated until reaching the desired range. On the other hand, if the estimated pinch point is lower than the acceptable value, the evaporator's pressure is decreased and the procedure is repeated until the value of the pinch point is within the aforementioned range.

In the case of the condenser, the acceptable range of pinch point is set to be equal to:

$$PP_{cond} = 7.5 \pm 0.2 \text{ K}$$

For the calculation of the pinch point, an initial value of the condenser pressure is guessed. This initial value was set to be equal to the examined working fluid's pressure for $T_{hs,cond} = 20^{\circ}\text{C}$.

Then the value of the pinch point is calculated for this pressure and the examined mass flow rate of the working fluid. If the estimated pinch point is lower than the acceptable value, the condenser's pressure is increased and the procedure is repeated until reaching the desired range. On the other hand, if the estimated pinch point is higher than the acceptable value, the condenser's pressure is decreased and the procedure is repeated until the value of the pinch point is within the aforementioned range.

Furthermore, a typical value for the temperature increase at the superheater and the temperature decrease at the subcooler were determined:

$$\Delta T_{superheat} = 5^{\circ}\text{C} , \quad \Delta T_{subcool} = 5^{\circ}\text{C}$$

After defining these parameters, the simulation of the design point of the ORC is feasible. The mass flow rate of the working fluid needs to be initialized. A typical value of $0.05 - 0.1 \text{ kg/s}$ is considered depending on the type of working fluid, as CoolProp is very sensitive to the thermodynamic changes of the fluids. Nevertheless, the first guessed value does not have an effect on the optimized value of the mass flow rate.

The optimization of the cycle is complete when the absolute difference of the inlet enthalpy of the evaporator and the outlet enthalpy of the pump is minimized.

The results of this procedure are summarized at the tables following for all the working fluids examined for this application.

Table 3.7 *On-design properties of Propylene*

Component	Variable	Value	Unit
—	Evaporation Temperature	65.55	$^{\circ}\text{C}$
	Condensation Temperature	19.83	$^{\circ}\text{C}$
Evaporator	Model	AC30EQ	—
	Number of Plates	48	—
	Surface	1.448	m^2
Expander	Isentropic Efficiency	77.97	%
	Nominal Rotational Speed	3350	rpm
	Nominal Volumetric Displacement	$14.188 * 10^{-6}$	m^3/rev
	Electric Power Output	1.6058	kWe
Condenser	Model	CB30	—
	Number of Plates	54	—
	Surface	1.800	m^2
	Cold stream's mass flow rate	1.090	kg/s
Pump	Isentropic Efficiency	67.77	%
	Nominal Rotational Speed	298.32	rpm
	Electric Consumption	0.3072	kWe
—	Mass flow rate	0.05150	kg/s
	Thermal Efficiency	8.578	%
	Net Electric Efficiency	6.493	%

Table 3.8 *On-design properties of Propane*

Component	Variable	Value	Unit
—	Evaporation Temperature	65.21	°C
	Condensation Temperature	19.82	°C
Evaporator	Model	<i>AC30EQ</i>	—
	Number of Plates	50	—
	Surface	1.508	m^2
Expander	Isentropic Efficiency	77.97	%
	Nominal Rotational Speed	3400	<i>rpm</i>
	Nominal Volumetric Displacement	$16.283 * 10^{-6}$	m^3/rev
	Electric Power Output	1.5793	<i>kWe</i>
Condenser	Model	<i>CB30</i>	—
	Number of Plates	54	—
	Surface	1.800	m^2
	Cold stream's mass flow rate	1.090	<i>kg/s</i>
Pump	Isentropic Efficiency	65.28	%
	Nominal Rotational Speed	297.38	<i>rpm</i>
	Electric Consumption	0.2669	<i>kWe</i>
—	Mass flow rate	0.04980	<i>kg/s</i>
	Thermal Efficiency	8.587	%
	Net Electric Efficiency	6.562	%

Table 3.9 *On-design properties of R32*

Component	Variable	Value	Unit
—	Evaporation Temperature	66.01	°C
	Condensation Temperature	19.81	°C
Evaporator	Model	<i>AC30EQ</i>	—
	Number of Plates	45	—
	Surface	1.357	m^2
Expander	Isentropic Efficiency	77.76	%
	Nominal Rotational Speed	3850	<i>rpm</i>
	Nominal Volumetric Displacement	$8.092 * 10^{-6}$	m^3/rev
	Electric Power Output	1.6410	<i>kWe</i>
Condenser	Model	<i>CB30</i>	—
	Number of Plates	53	—
	Surface	1.767	m^2
	Cold stream's mass flow rate	1.089	<i>kg/s</i>
Pump	Isentropic Efficiency	73.37	%
	Nominal Rotational Speed	225.18	<i>rpm</i>
	Electric Consumption	0.3463	<i>kWe</i>
—	Mass flow rate	0.07245	<i>kg/s</i>
	Thermal Efficiency	8.628	%
	Net Electric Efficiency	6.473	%

Table 3.10 *On-design properties of R134a*

Component	Variable	Value	Unit
—	Evaporation Temperature	65.06	°C
	Condensation Temperature	19.81	°C
Evaporator	Model	<i>AC30EQ</i>	—
	Number of Plates	54	—
	Surface	1.629	m^2
Expander	Isentropic Efficiency	77.16	%
	Nominal Rotational Speed	4300	<i>rpm</i>
	Nominal Volumetric Displacement	$15.239 * 10^{-6}$	m^3/rev
	Electric Power Output	1.5252	<i>kWe</i>
Condenser	Model	<i>CB30</i>	—
	Number of Plates	54	—
	Surface	1.800	m^2
	Cold stream's mass flow rate	1.090	<i>kg/s</i>
Pump	Isentropic Efficiency	62.80	%
	Nominal Rotational Speed	234.10	<i>rpm</i>
	Electric Consumption	0.1863	<i>kWe</i>
—	Mass flow rate	0.09389	<i>kg/s</i>
	Thermal Efficiency	8.595	%
	Net Electric Efficiency	6.694	%

Table 3.11 *On-design properties of R152a*

Component	Variable	Value	Unit
—	Evaporation Temperature	63.92	°C
	Condensation Temperature	19.82	°C
Evaporator	Model	<i>AC30EQ</i>	—
	Number of Plates	50	—
	Surface	1.508	m^2
Expander	Isentropic Efficiency	77.44	%
	Nominal Rotational Speed	4150	<i>rpm</i>
	Nominal Volumetric Displacement	$19.133 * 10^{-6}$	m^3/rev
	Electric Power Output	1.5351	<i>kWe</i>
Condenser	Model	<i>CB30</i>	—
	Number of Plates	52	—
	Surface	1.734	m^2
	Cold stream's mass flow rate	1.087	<i>kg/s</i>
Pump	Isentropic Efficiency	59.99	%
	Nominal Rotational Speed	211.17	<i>rpm</i>
	Electric Consumption	0.1490	<i>kWe</i>
—	Mass flow rate	0.06220	<i>kg/s</i>
	Thermal Efficiency	8.817	%
	Net Electric Efficiency	6.931	%

Table 3.12 *On-design properties of R227ea*

Component	Variable	Value	Unit
—	Evaporation Temperature	66.18	°C
	Condensation Temperature	19.86	°C
Evaporator	Model	<i>AC30EQ</i>	—
	Number of Plates	61	—
	Surface	1.840	m^2
Expander	Isentropic Efficiency	76.56	%
	Nominal Rotational Speed	4500	<i>rpm</i>
	Nominal Volumetric Displacement	$17.965 * 10^{-6}$	m^3/rev
	Electric Power Output	1.4340	<i>kWe</i>
Condenser	Model	<i>CB30</i>	—
	Number of Plates	58	—
	Surface	1.934	m^2
	Cold stream's mass flow rate	1.097	<i>kg/s</i>
Pump	Isentropic Efficiency	57.94	%
	Nominal Rotational Speed	282.09	<i>rpm</i>
	Electric Consumption	0.1834	<i>kWe</i>
—	Mass flow rate	0.13259	<i>kg/s</i>
	Thermal Efficiency	8.043	%
	Net Electric Efficiency	6.253	%

Table 3.13 *On-design properties of R410a*

Component	Variable	Value	Unit
—	Evaporation Temperature	68.75	°C
	Condensation Temperature	19.81	°C
Evaporator	Model	<i>AC30EQ</i>	—
	Number of Plates	55	—
	Surface	1.659	m^2
Expander	Isentropic Efficiency	77.43	%
	Nominal Rotational Speed	4150	<i>rpm</i>
	Nominal Volumetric Displacement	$6.912 * 10^{-6}$	m^3/rev
	Electric Power Output	1.6058	<i>kWe</i>
Condenser	Model	<i>CB30</i>	—
	Number of Plates	56	—
	Surface	1.867	m^2
	Cold stream's mass flow rate	1.094	<i>kg/s</i>
Pump	Isentropic Efficiency	74.67	%
	Nominal Rotational Speed	279.13	<i>rpm</i>
	Electric Consumption	0.4607	<i>kWe</i>
—	Mass flow rate	0.10237	<i>kg/s</i>
	Thermal Efficiency	8.267	%
	Net Electric Efficiency	6.005	%

Table 3.14 *On-design properties of R-C318*

Component	Variable	Value	Unit
—	Evaporation Temperature	65.89	°C
	Condensation Temperature	19.84	°C
Evaporator	Model	<i>AC30EQ</i>	—
	Number of Plates	63	—
	Surface	1.900	m^2
Expander	Isentropic Efficiency	76.05	%
	Nominal Rotational Speed	4600	<i>rpm</i>
	Nominal Volumetric Displacement	$24.063 * 10^{-6}$	m^3/rev
	Electric Power Output	1.3748	<i>kWe</i>
Condenser	Model	<i>CB30</i>	—
	Number of Plates	60	—
	Surface	2.001	m^2
	Cold stream's mass flow rate	1.100	<i>kg/s</i>
Pump	Isentropic Efficiency	51.70	%
	Nominal Rotational Speed	273.00	<i>rpm</i>
	Electric Consumption	0.1445	<i>kWe</i>
—	Mass flow rate	0.13757	<i>kg/s</i>
	Thermal Efficiency	7.842	%
	Net Electric Efficiency	6.152	%

Table 3.15 *On-design properties of R1234yf*

Component	Variable	Value	Unit
—	Evaporation Temperature	66.04	°C
	Condensation Temperature	19.83	°C
Evaporator	Model	<i>AC30EQ</i>	—
	Number of Plates	55	—
	Surface	1.659	m^2
Expander	Isentropic Efficiency	77.53	%
	Nominal Rotational Speed	4100	<i>rpm</i>
	Nominal Volumetric Displacement	$15.574 * 10^{-6}$	m^3/rev
	Electric Power Output	1.5224	<i>kWe</i>
Condenser	Model	<i>CB30</i>	—
	Number of Plates	55	—
	Surface	1.834	m^2
	Cold stream's mass flow rate	1.093	<i>kg/s</i>
Pump	Isentropic Efficiency	62.85	%
	Nominal Rotational Speed	292.00	<i>rpm</i>
	Electric Consumption	0.2314	<i>kWe</i>
—	Mass flow rate	0.10876	<i>kg/s</i>
	Thermal Efficiency	8.385	%
	Net Electric Efficiency	6.455	%

Table 3.16 On-design properties of R1234ze

Component	Variable	Value	Unit
—	Evaporation Temperature	64.93	°C
	Condensation Temperature	19.84	°C
Evaporator	Model	AC30EQ	—
	Number of Plates	55	—
	Surface	1.659	m ²
Expander	Isentropic Efficiency	77.04	%
	Nominal Rotational Speed	4350	rpm
	Nominal Volumetric Displacement	19.393 * 10 ⁻⁶	m ³ /rev
	Electric Power Output	1.4973	kWe
Condenser	Model	CB30	—
	Number of Plates	54	—
	Surface	1.800	m ²
	Cold stream's mass flow rate	1.091	kg/s
Pump	Isentropic Efficiency	58.31	%
	Nominal Rotational Speed	248.46	rpm
	Electric Consumption	0.1638	kWe
—	Mass flow rate	0.09647	kg/s
	Thermal Efficiency	8.519	%
	Net Electric Efficiency	6.667	%

It is apparent that the model of the evaporator and the condenser is the same for all refrigerants. This is anticipated as the flow rate of both streams in both cases is low, thus small flat plate heat exchangers are suitable for the transfer of the heating loads. Furthermore, as it can be seen from Figure 3.4 the surface of the evaporator is lower for working fluids with low mass flow rate compared to the refrigerants with high mass flow rate. In Figure 3.5 it is obvious that the surface of the condenser is almost identical for all working fluids, as the restriction of the pressure drop in the cold stream of the condenser defines its size.

In Figure 3.6 and Figure 3.7 it is shown that R152a has the highest thermal and net electric efficiency ($\eta_{th} = 8.817\%$ and $\eta_{el} = 6.931\%$ respectively) while R-C318 has the lowest thermal efficiency ($\eta_{th} = 7.842\%$) and R410a the lowest net electric efficiency ($\eta_{el} = 6.005\%$) due to its high motor consumption.

Furthermore, according to Figure 3.8 all working fluids are characterized by relatively high expander's isentropic efficiency, with Propylene and Propane having the highest value ($\eta_{exp,is} = 77.97\%$) while R-C318 has the lowest one ($\eta_{exp,is} = 76.05\%$). Finally, in Figure 3.9 it is apparent that the range of pump's isentropic efficiency for the examined working fluids is vast. R410a has the highest pump's isentropic efficiency ($\eta_{pump,is} = 74.67\%$) while R-C318 has the lowest one ($\eta_{exp,is} = 51.70\%$).

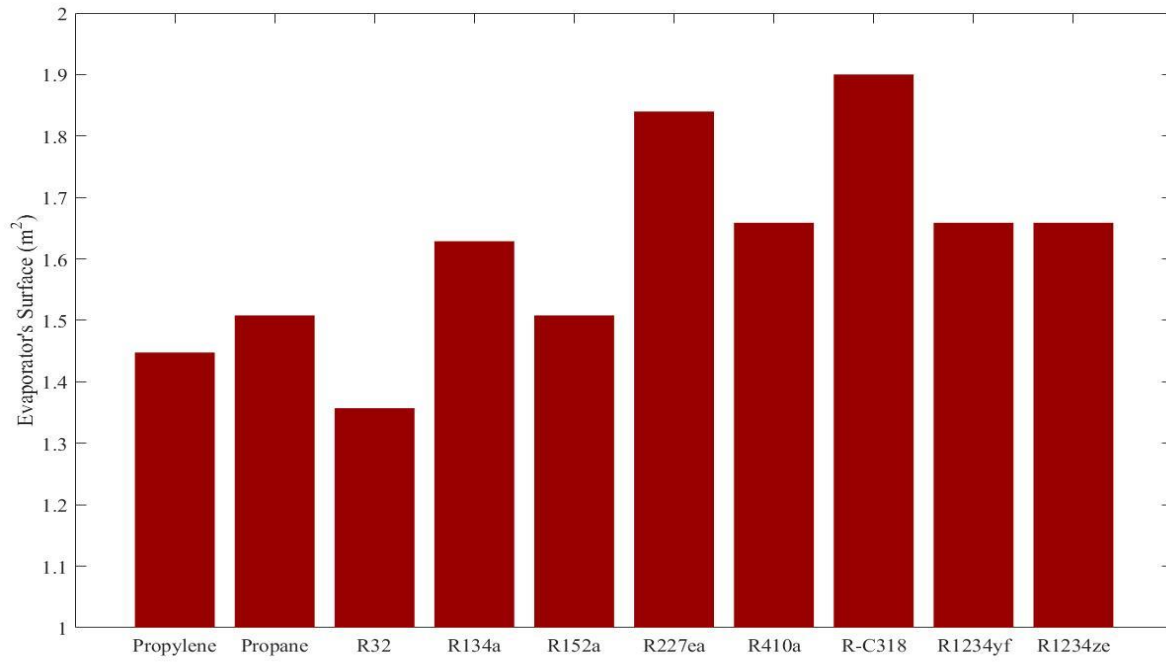


Figure 3.4 *Evaporator's surface of various working fluids*

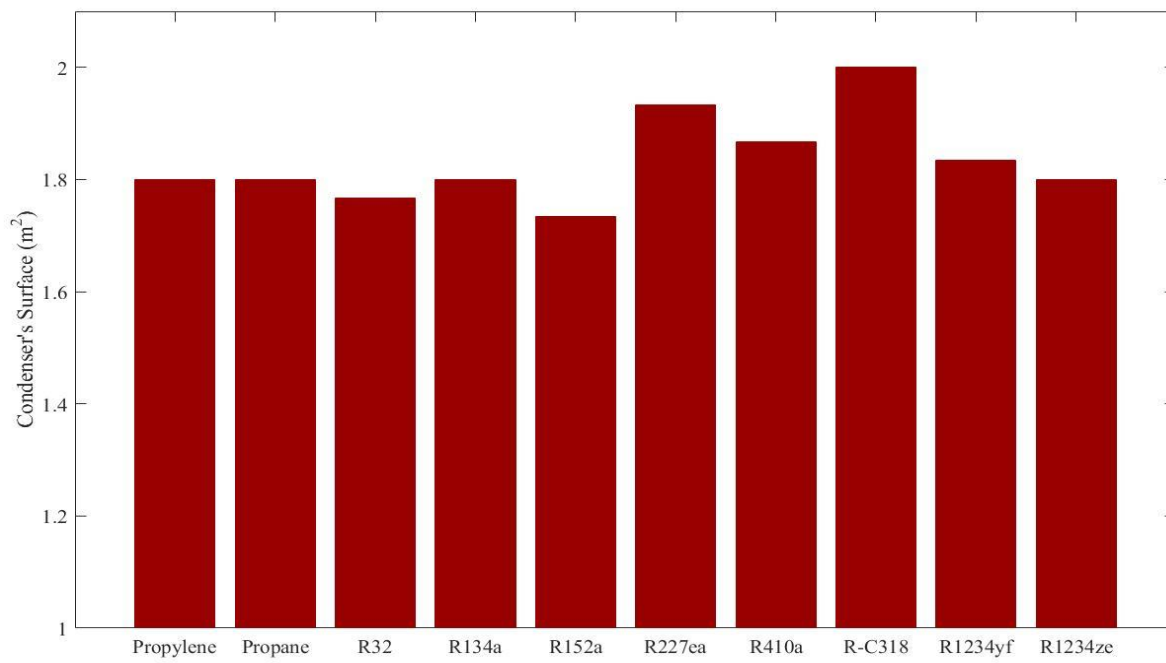


Figure 3.5 *Condenser's surface of various working fluids*

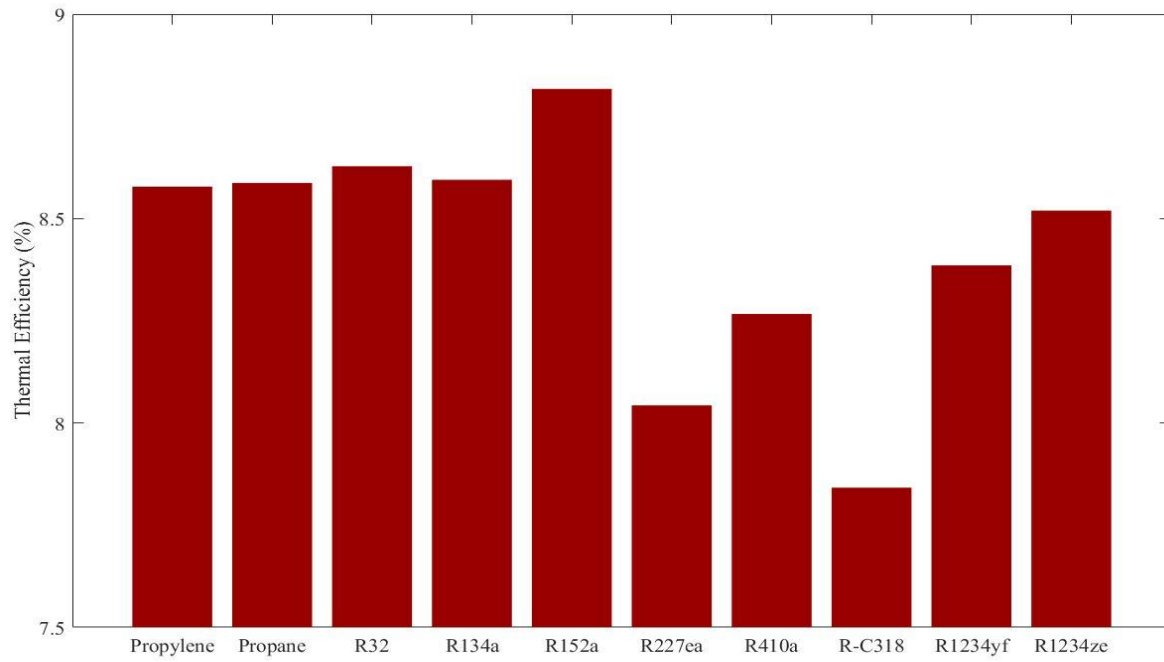


Figure 3.6 Thermal efficiency of various working fluids

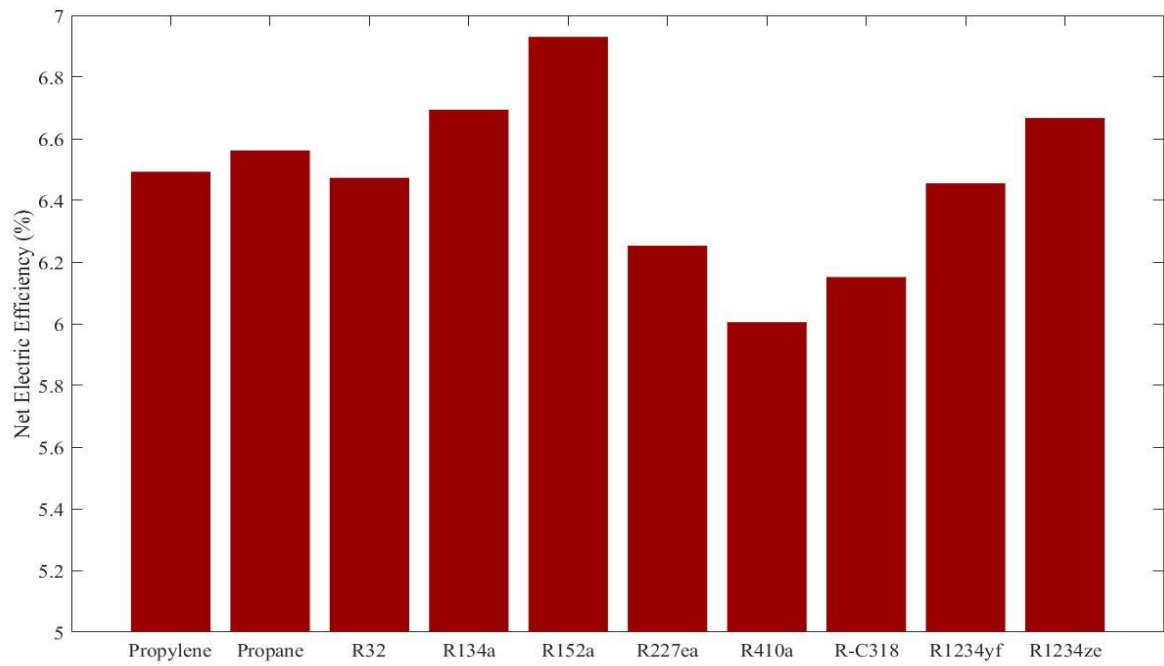


Figure 3.7 Net electric efficiency of various working fluids

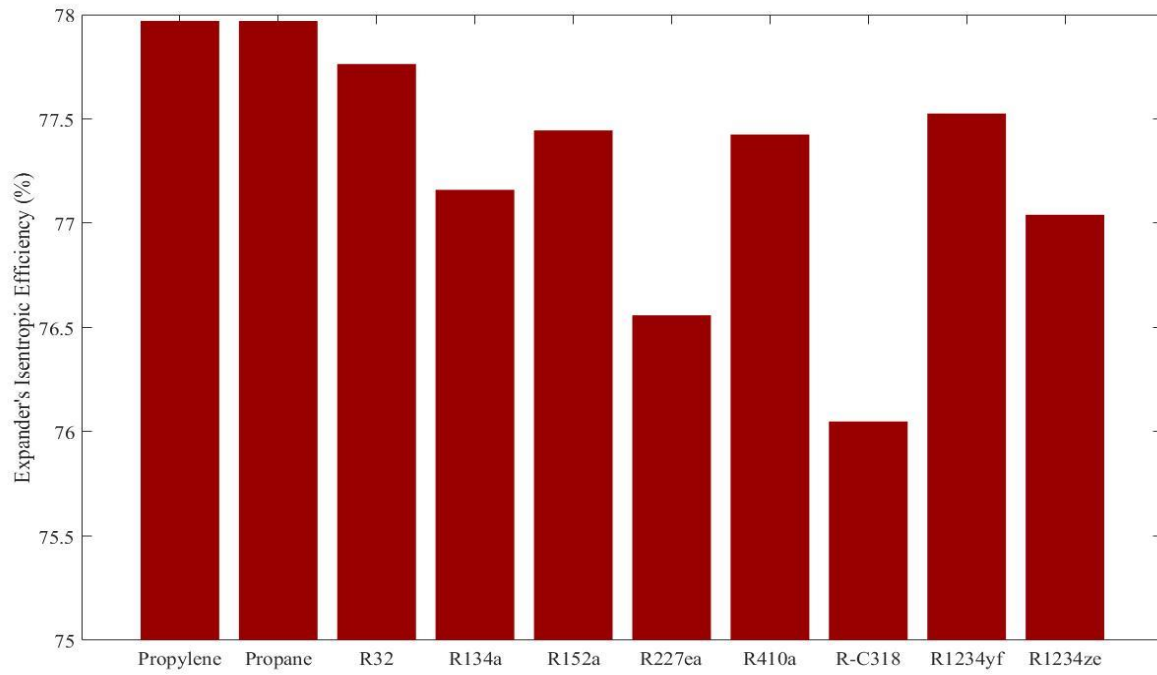


Figure 3.8 *Expander's isentropic efficiency of various working fluids*

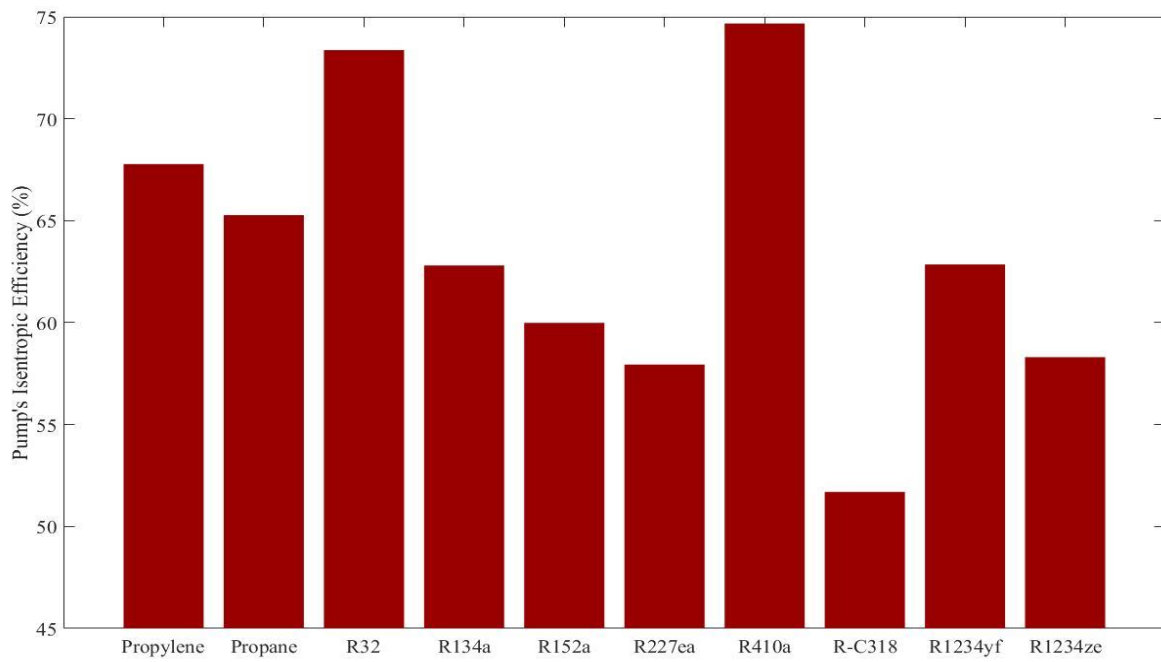


Figure 3.9 *Pump's isentropic efficiency of various working fluids*

3.4 Cost of ORC

After the calculation of the on-design properties of the ORC configuration for the examined working fluids, the estimation of the cycle's cost is feasible. In order to compute the total cost, the price of every component should first be calculated.

Control and hardware

The control mechanisms and hardware are essential so as to ensure the orderly operation of the cycle and the confinement of possible errors. A fixed cost [7] for the control system is assumed for all working fluids equal to:

$$C_{cont} = 800 \text{ €}$$

Piping

For this application, two different pipes are used. A small pipe with diameter equal to $\varnothing 22$ is used for the vapor state of the working fluid as the velocity of vapor must be high for safety reasons as well as its density and thus volume is lower than those of its liquid form. On the other hand, a pipe with diameter equal to $\varnothing 35$ is used for the liquid state of the working fluid as its velocity is lower and its density higher. The length of both pipes was assumed to be $3m$ and their cost was taken equal to $C_{22} = 6.6836 \text{ €/m}$ and $C_{35} = 12.1892 \text{ €/m}$. As a result, the total cost of the piping is equal to:

$$C_{pip,orc} = 3 * (C_{22} + C_{35}) \Rightarrow C_{pip,orc} = 56.62 \text{ €}$$

Feeding Tank

As this application is used for small electricity production, a feeding tank with a volume capacity equal to 30 lt was assumed. For the estimation of its cost, data from Zilmet company [75] were used in order to create a curve of the cost of the feeding tank as a function of its size. For a feeding tank of 30 lt , its cost is equal to:

$$C_{tank,orc} = 284.76 \text{ €}$$

Working Fluid

The most important variable for the sustainability of an ORC is the cost of its working fluid. For this application, it is assumed that the total volume of the working fluid is equal to:

$$V_{wf} = 1.5 * V_{tank,orc} \Rightarrow V_{wf} = 45 \text{ lt}$$

Thus the cost of each working fluid is easily calculated via the last column of Table 3.6:

$$C_{wf} = V_{wf} (\text{lt}) * cost_{wf} (\text{€/lt}) \quad (3.80)$$

Evaporator and Condenser

For the calculation of the cost of the flat plate heat exchangers the following equations are used [7]:

$$C_{evap} = 190 + 310 * A_{evap} \quad (3.81)$$

$$C_{cond} = 190 + 310 * A_{cond} \quad (3.82)$$

Expander

The cost of the expander is calculated through experimental data proposed in literature. The input data of its cost function is the electric output of the generator which is coupled with the expander.

Pump

For the estimation of the cost of the pump, the following formula was used [76]:

$$C_{pump} = 1800 * \left(\frac{W_{mech,pump}}{300} \right)^{0.25} \quad (3.83)$$

where $W_{mech,pump}$ is the nominal mechanical work of the pump and it is measured in W .

Generator and Motor

The cost of the generator and the motor is a function of their electricity production and consumption respectively. The formulas [77] used for this calculation are listed below, where the electric power is measured in kW :

$$C_{gen} = 71.7 * P_{el,gen}^{0.95} \quad (3.84)$$

$$C_{mot} = 71.7 * P_{el,mot}^{0.95} \quad (3.85)$$

The total cost of the cycle is equal to the sum of its components. The final cost is then divided by 0.7 in order to include the cost of the installation of the equipment [7]. Thus, the final cost is calculated by the following equation:

$$C_{tot,ORC} = \frac{C_{cont} + C_{pip,orc} + C_{tank,orc} + C_{wf} + C_{evap} + C_{cond} + C_{exp} + C_{pump} + C_{gen} + C_{mot}}{0.7} \quad (3.86)$$

In the following Table 3.17 and Figure 3.10, the total cost of the ORC for the examined working fluids is shown. The cost of R-C318 is emitted from the figure as it is very high and thus not economically compared to the rest of the examined refrigerants. Refrigerant R152a and the two examined hydrocarbons (Propylene and Propane) appear to be the most suitable candidates for the application.

Table 3.17 *Total cost of the ORC of the examined working fluids*

Working Fluid	Cost	Unit
Propylene	7638.82	€
Propane	7309.56	€
R32	8644.13	€
R134a	9162.70	€
R152a	7167.06	€
R227ea	14900.77	€
R410a	10450.29	€
R-C318	64123.85	€
R1234yf	13733.37	€
R1234ze	9470.49	€

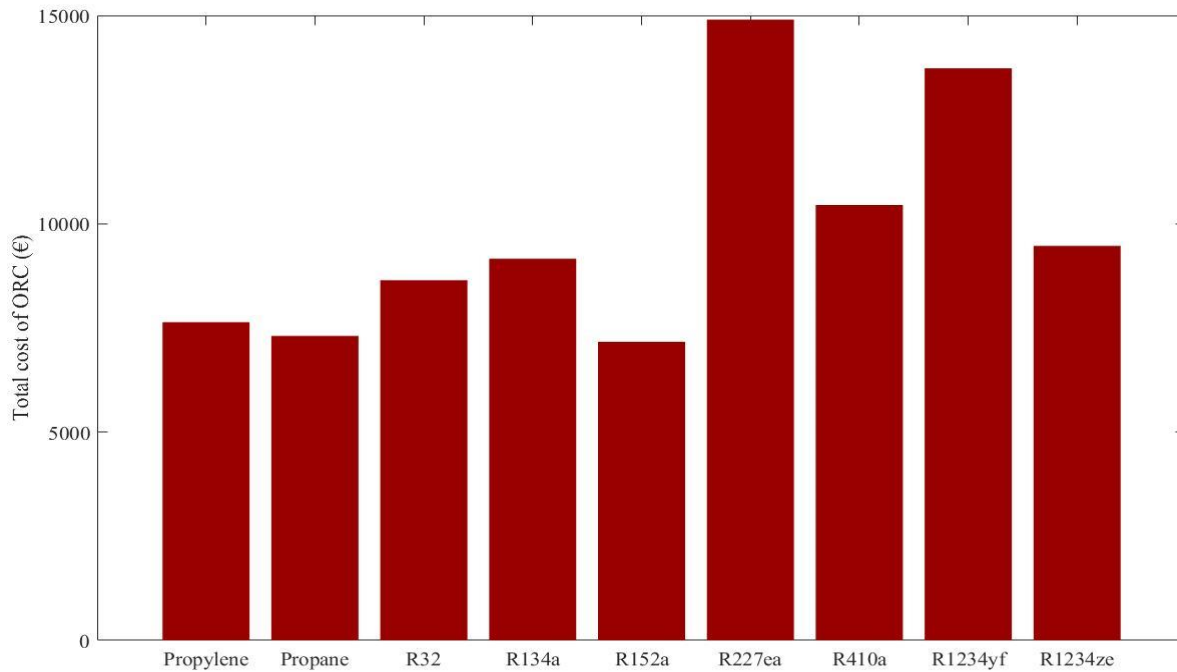


Figure 3.10 *Total cost of ORC of various working fluids*

A pie chart depicting the division of the total cost of the ORC into each component follows at Figure 5.3 when R152a is used as the working fluid, as it is proven to be the most economically viable choice as elaborated at Chapter 5. .

3.5 Off-Design Simulation of ORC

During the on-design simulation of the cycle, a steady input temperature of $T_{hs,evap,in} = 80^\circ\text{C}$ was assumed. However, as aforementioned, the ORC deploys the heat excess saved at the storage tank which originates from the thermal module of the PVT collectors. As a result, the input temperature of the ORC deviates from its on-design maximum temperature depending on the ambient temperature and the sun radiation.

For this application, it was decided that the ORC would operate if the hot stream of the evaporator reached a minimum temperature of $T_{hs,evap,in,min} = 65^\circ\text{C}$. Then, the following assumption for the heating load absorbed by the evaporator was made:

- For the minimum temperature mentioned, the heating load would be equal to the half of the on-design simulation:

$$T_{hs,evap,in,min} = 65^\circ\text{C} \Rightarrow Q_{evap,min} = 10 \text{ kW}$$

- For the maximum temperature of the on-design simulation, the heating load would be equal to the one mentioned in subchapter 3.3:

$$T_{hs,evap,in,max} = 80^\circ\text{C} \Rightarrow Q_{evap,max} = 20 \text{ kW}$$

For the in-between temperatures of the cycle's operation range, a linear interpolation was assumed for the calculation of the heating load of the evaporator. Then, the whole cycle was calculated for the examined working fluids for temperature intervals of 2.5°C .

For the calculations, the components of the ORC (evaporator, expander, generator, condenser, pump and motor) were the ones which resulted from the on-design simulation but their properties differed from their nominal ones. The parameters which remained constant throughout this simulation were the mass flow rate of the hot stream of the evaporator as well as the inlet and outlet conditions of the cold stream of the condenser:

$$\dot{m}_{hs,evap} = 0.3 \text{ kg/s}$$

$$T_{cs,cond,in} = 7.5^\circ\text{C}$$

$$T_{cs,cond,out} = 11.5^\circ\text{C}$$

An initial value of the mass flow rate of the working fluid was guessed as follows:

$$\dot{m}_{wf} = \dot{m}_{wf,max} * \frac{\dot{Q}_{evap}}{\dot{Q}_{evap,max}} \quad (3.87)$$

where $\dot{m}_{wf,max}$ is the mass flow rate of the refrigerant during on-design simulation.

The solution of the off-design problem is similar to the on-design one elaborated at subchapter 3.3. The results of this procedure, as well as the results of the on-design simulation, are listed on

Table 3.18 that follows. Furthermore, at Figure 3.11 the net electric production of the examined working fluids is depicted as a function of the input temperature of the hot stream of the evaporator. Similarly, at Figure 3.12 the net electric efficiency is shown as a function of the aforementioned temperature.

Table 3.18 *Off-design properties of the examined working fluids*

	Propylene				Propane			
$T_{hs,evap,in}$ (°C)	p_{evap} (bar)	$P_{el,net}$ (kW)	η_{el} (%)	\dot{m}_{wf} (kg/s)	p_{evap} (bar)	$P_{el,net}$ (kW)	η_{el} (%)	\dot{m}_{wf} (kg/s)
65.0	22.645	0.4579	4.5795	0.0259	18.918	0.4680	4.6801	0.0253
67.5	23.423	0.5773	4.9483	0.0302	19.590	0.5893	5.0507	0.0294
70.0	24.283	0.7049	5.2869	0.0344	20.283	0.7168	5.3759	0.0335
72.5	25.151	0.8390	5.5935	0.0387	21.008	0.8519	5.6795	0.0376
75.0	26.049	0.9804	5.8823	0.0430	21.827	0.9975	5.9847	0.0417
77.5	27.073	1.1327	6.1784	0.0472	22.624	1.1495	6.2699	0.0457
80.0	28.243	1.2986	6.4932	0.0515	23.528	1.3124	6.5620	0.0498
	R32				R134a			
$T_{hs,evap,in}$ (°C)	p_{evap} (bar)	$P_{el,net}$ (kW)	η_{el} (%)	\dot{m}_{wf} (kg/s)	p_{evap} (bar)	$P_{el,net}$ (kW)	η_{el} (%)	\dot{m}_{wf} (kg/s)
65.0	34.888	0.4712	4.7122	0.0349	14.749	0.5020	5.0199	0.0477
67.5	36.201	0.5898	5.0552	0.0409	15.380	0.6252	5.3589	0.0555
70.0	37.662	0.7161	5.3707	0.0470	16.019	0.7545	5.6588	0.0632
72.5	39.109	0.8467	5.6445	0.0531	16.677	0.8898	5.9319	0.0709
75.0	40.744	0.9860	5.9162	0.0594	17.370	1.0325	6.1953	0.0786
77.5	42.485	1.1333	6.1818	0.0658	18.095	1.1819	6.4466	0.0863
80.0	44.807	1.2947	6.4733	0.0725	18.923	1.3388	6.6942	0.0939
	R152a				R227ea			
$T_{hs,evap,in}$ (°C)	p_{evap} (bar)	$P_{el,net}$ (kW)	η_{el} (%)	\dot{m}_{wf} (kg/s)	p_{evap} (bar)	$P_{el,net}$ (kW)	η_{el} (%)	\dot{m}_{wf} (kg/s)
65.0	13.073	0.5223	5.2228	0.0315	10.416	0.4719	4.7192	0.0689
67.5	13.579	0.6485	5.5589	0.0366	10.894	0.5877	5.0370	0.0798
70.0	14.109	0.7818	5.8636	0.0418	11.369	0.7083	5.3122	0.0907
72.5	14.628	0.9198	6.1320	0.0469	11.868	0.8350	5.5669	0.1014
75.0	15.212	1.0685	6.4109	0.0520	12.431	0.9697	5.8181	0.1119
77.5	15.813	1.2242	6.6774	0.0571	12.989	1.1071	6.0389	0.1223
80.0	16.442	1.3861	6.9305	0.0622	13.619	1.2506	6.2532	0.1326
	R410a				R-C318			
$T_{hs,evap,in}$ (°C)	p_{evap} (bar)	$P_{el,net}$ (kW)	η_{el} (%)	\dot{m}_{wf} (kg/s)	p_{evap} (bar)	$P_{el,net}$ (kW)	η_{el} (%)	\dot{m}_{wf} (kg/s)
65.0	34.533	0.4351	4.3507	0.0488	7.404	0.4720	4.7200	0.0721
67.5	35.966	0.5464	4.6831	0.0572	7.730	0.5847	5.0114	0.0834
70.0	37.501	0.6632	4.9742	0.0657	8.086	0.7042	5.2814	0.0946
72.5	39.234	0.7867	5.2443	0.0744	8.445	0.8283	5.5221	0.1056
75.0	41.098	0.9160	5.4960	0.0833	8.860	0.9604	5.7624	0.1164
77.5	43.248	1.0526	5.7412	0.0924	9.263	1.0935	5.9643	0.1271
80.0	46.391	1.2010	6.0051	0.1024	9.695	1.2303	6.1515	0.1376

	R1234yf				R1234ze			
$T_{hs, evap, in}$ (°C)	p_{evap} (bar)	$P_{el, net}$ (kW)	η_{el} (%)	\dot{m}_{wf} (kg/s)	p_{evap} (bar)	$P_{el, net}$ (kW)	η_{el} (%)	\dot{m}_{wf} (kg/s)
65.0	14.633	0.4739	4.7388	0.0557	11.205	0.5027	5.0272	0.0494
67.5	15.219	0.5916	5.0712	0.0647	11.666	0.6245	5.3527	0.0574
70.0	15.823	0.7155	5.3666	0.0736	12.146	0.7526	5.6445	0.0653
72.5	16.512	0.8487	5.6577	0.0825	12.661	0.8886	5.9237	0.0732
75.0	17.187	0.9873	5.9238	0.0913	13.193	1.0303	6.1821	0.0810
77.5	17.949	1.1354	6.1929	0.1001	13.752	1.1794	6.4329	0.0888
80.0	18.769	1.2911	6.4555	0.1088	14.339	1.3335	6.6674	0.0965

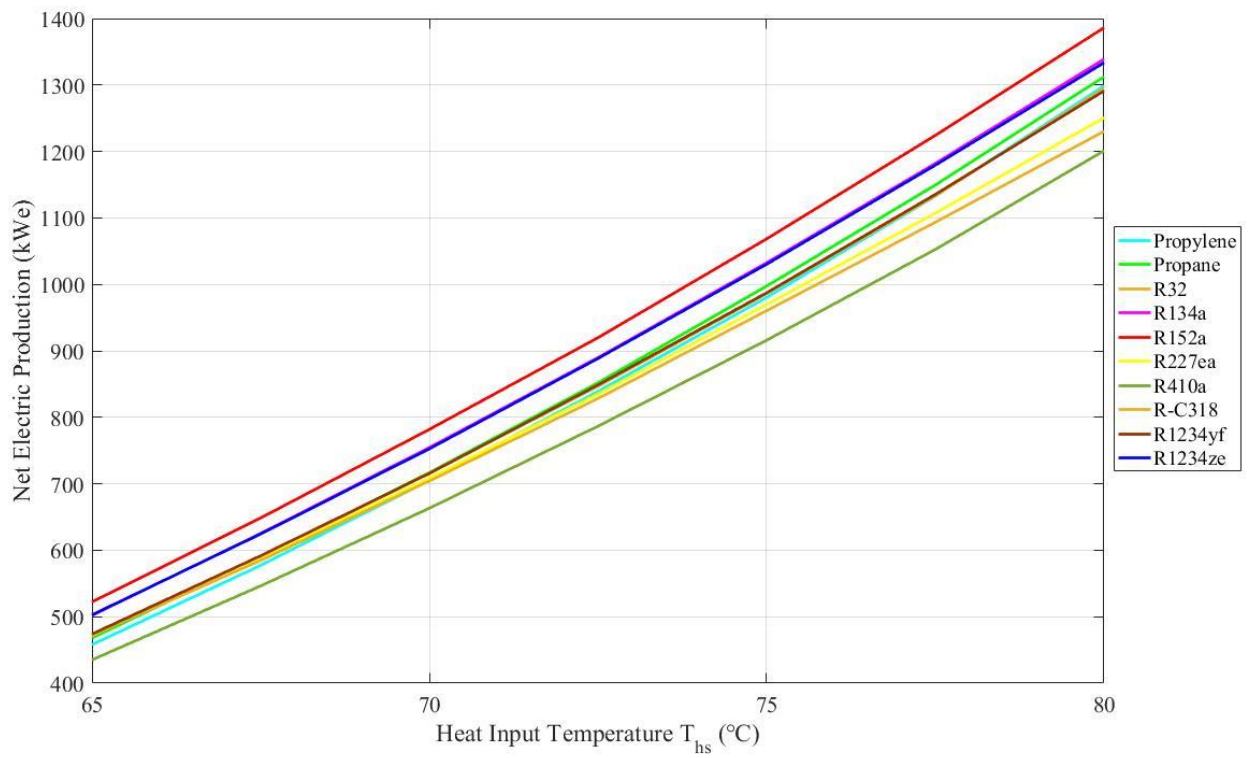


Figure 3.11 Net electric production as a function of heat input temperature

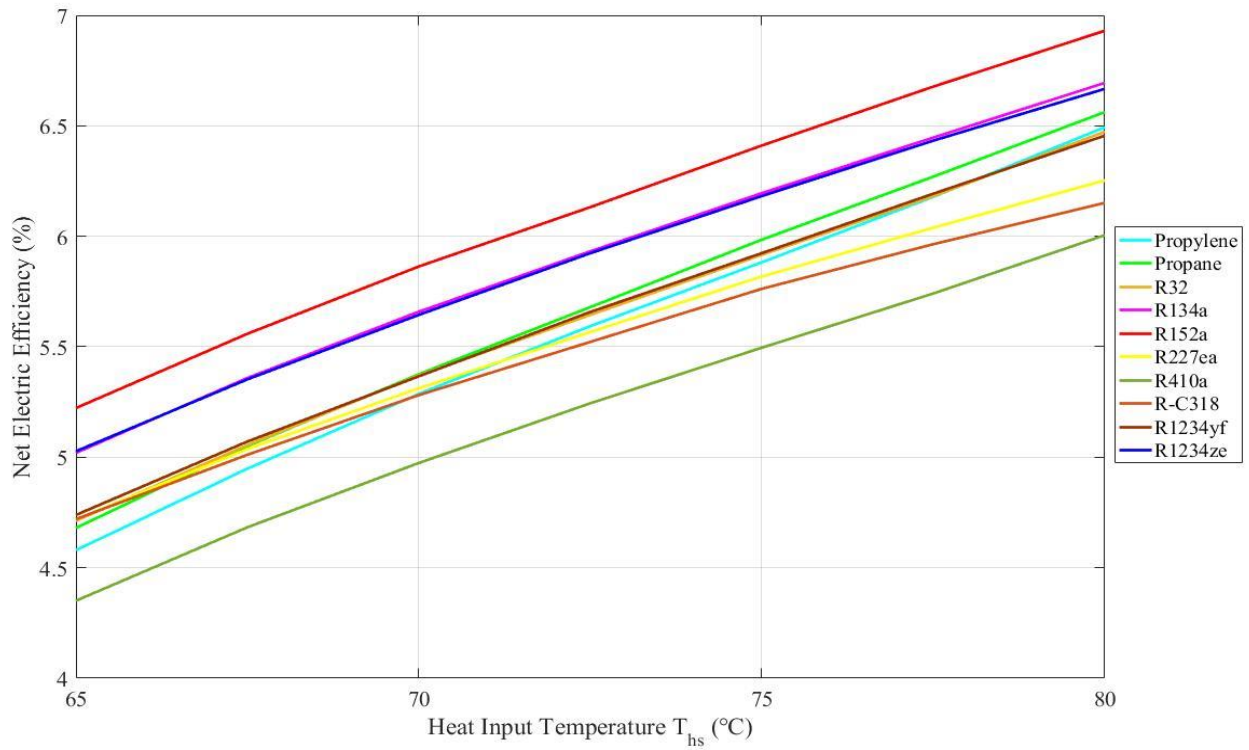


Figure 3.12 Net electric efficiency as a function of heat input temperature

From the two figures it is visible that for all refrigerants, the net electric production as well as the net electric efficiency is increased when the input temperature from the storage tank is increased. For some working fluids, like Propylene, Propane and R1234yf, the electric efficiency is increased with high rates at high temperatures compared to others like R227ea and R-C318 which are characterized by a more stable increase.

Furthermore, for the whole operational temperature range R152a leads as the most efficient and productive working fluid ($\eta_{el,min} = 5.2228\%$, $\eta_{el,max} = 6.9305\%$), while R410a is the worst one ($\eta_{el,min} = 4.3507\%$, $\eta_{el,max} = 6.0051\%$).

Chapter 4. Coupling of PVT-ORC System

4.1 Modeling of the Configuration

Since the modeling of all components has been elaborated, the coupling of the solar collectors and the ORC is feasible for every hour of the year. In order to calculate the hourly temperature of the collector and the storage tank, the following initialization was assumed: the temperature of the storage tank and the inlet of the collector at the 1st hour of the year are equal to the ambient temperature at that time. Afterwards, for every hour of the year, the temperatures of the collectors, the storage tank and the inlet of the ORC are calculated following the next procedure:

- If the solar radiation is equal to $I_T = 0 \text{ Wh/m}^2$ and the temperature of the first element of the storage tank is $T_{st,1} = T_{iorc} < 65^\circ\text{C}$, there is no mass flow towards the circuit of the collectors as well as towards the evaporator of the ORC. As a result, no energy is absorbed by the collectors and their outlet temperature is set to be equal with the inlet one. Furthermore, the temperature of the mixing zones of the storage tank and the next inlet temperature of the collectors and the ORC remain equal to their previous values.
- If the solar radiation is $I_T > 0 \text{ Wh/m}^2$ and the temperature of the first element of the storage tank is $T_{st,1} = T_{iorc} < 65^\circ\text{C}$, there is no mass flow towards the evaporator of the ORC, but the working fluid goes through the collectors of the PVT modules with a mass flow rate equal to $\dot{m}_{col} = A_{col} * \dot{m}_{col,m^2}$. As a result, the working fluid is heated by solar radiation and the outlet temperature of the collectors is increased depending on their efficiency, as analyzed at subchapter 2.2. Furthermore, in order to calculate the temperature of the elements of the storage tank as well as the inlet temperatures of the collectors and the ORC for the next time interval, the function of the storage tank, which was elaborated at subchapter 2.3, is called.
- If the solar radiation is $I_T > 0 \text{ Wh/m}^2$ and the temperature of the first element of the storage tank is $T_{st,1} = T_{iorc} \geq 65^\circ\text{C}$, there is mass flow towards the evaporator of the ORC ($\dot{m}_{iorc} = 0.3 \text{ kg/s}$) as well as the collectors of the PVT modules with a mass flow rate equal to $\dot{m}_{col} = A_{col} * \dot{m}_{col,m^2}$. As a result, the working fluid is heated by solar radiation and the outlet temperature of the collectors is increased depending on their efficiency, as mentioned above. For the calculation of the electricity production by the ORC and the heat extracted by the evaporator, suitable polynomials are used by extrapolating the respective variables that were estimated at the off-design simulation at subchapter 3.5. Then the outlet temperature of the hot stream of the evaporator can be calculated as the heat extracted by the working fluid of the ORC is known. Furthermore, in order to calculate the temperature of the elements of the storage tank as well as the inlet temperatures of the collectors and the ORC for the next time interval, the function of the storage tank, which was elaborated at subchapter 2.3, is called. In this case, the outlet temperature of the collectors and the inlet temperature of the ORC should not be greater than the maximum temperature proposed by DualSun:

$$T_{col,out} \leq 80^{\circ}\text{C and } T_{iorc} \leq 80^{\circ}\text{C}$$

Nevertheless, during the calculations it was observed that for this application the temperature of the collectors never reached its maximum value.

- If the solar radiation is $I_T = 0 \text{ Wh/m}^2$ and the temperature of the first element of the storage tank is $T_{st,1} = T_{iorc} \geq 65^{\circ}\text{C}$, there is mass flow towards the evaporator of the ORC ($\dot{m}_{iorc} = 0.3 \text{ kg/s}$) but not towards the solar collectors. As a result, no energy is absorbed by the collectors and their outlet temperature is set to be equal with the inlet one. For the calculation of the electricity production by the ORC and the heat extracted by the evaporator, suitable polynomials are used by extrapolating the respective variables that were estimated at the off-design simulation at subchapter 3.5. Then the outlet temperature of the hot stream of the evaporator can be calculated as the heat extracted by the working fluid of the ORC is known. Furthermore, in order to calculate the temperature of the elements of the storage tank as well as the inlet temperatures of the collectors and the ORC for the next time interval, the function of the storage tank, which was elaborated at subchapter 2.3, is called. In this case, the outlet temperature of the collectors and the inlet temperature of the ORC should not be greater than the maximum temperature proposed by DualSun:

$$T_{col,out} \leq 80^{\circ}\text{C and } T_{iorc} \leq 80^{\circ}\text{C}$$

As mentioned above, during the calculations it was observed that for this application the temperature of the collectors never reached its maximum value.

The above procedure was followed for all the following scenarios:

- ❖ For every city that was mentioned at subchapter 2.1 (Athens, Naples, Larnaca, Madrid, Lisbon)
- ❖ For all the examined working fluids (Propylene, Propane, R32, R134a, R152a, R227ea, R410a, R-C318, R1234yf, R1234ze)
- ❖ For 6 different values of solar collector area, starting at 10 panels, with a surface equal to $A_{panel} = 1.654 \text{ m}^2$, and adding 4 panels at each scenario until reaching a total surface area of $A_{col,max} = 49.62 \text{ m}^2$. This upper limit was set as this system was studied for a residence application and higher values of collectors' surface would be excessive.
- ❖ For 6 different storage tank volumes. The dimensions of each storage tank were acquired by Austria Email [78] and are listed at Table 4.1. It was assumed that the storage tank has a cylindrical shape instead of a more complicated one. Thus, by knowing its volume and diameter, its height was easily calculated as follows:

$$H_{st} = \frac{4 * V_{st}}{\pi * D_{st}^2} \quad (4.1)$$

Table 4.1 Dimensions of examined storage tanks

Volume V_{st} (lt)	Diameter D_{st} (m)	Height H_{st} (m)
200	0.50	1.019
300	0.50	1.528
500	0.65	1.507
800	0.79	1.632
1000	0.79	2.040
1500	1.00	1.910

4.2 Energetic and Exergetic Results

As a total number of 1800 scenarios were examined, it was decided that the results of only a few of them will be presented.

R152a was proven to be the most economically feasible solution as the working fluid of the ORC, as it will be shown at Chapter 5. Thus, at Figures 4.1 – 4.5 the net electricity production of the ORC with R152a as its working fluid is depicted for the examined cities as a function of the volume of the storage tank and the number of the PVT modules.

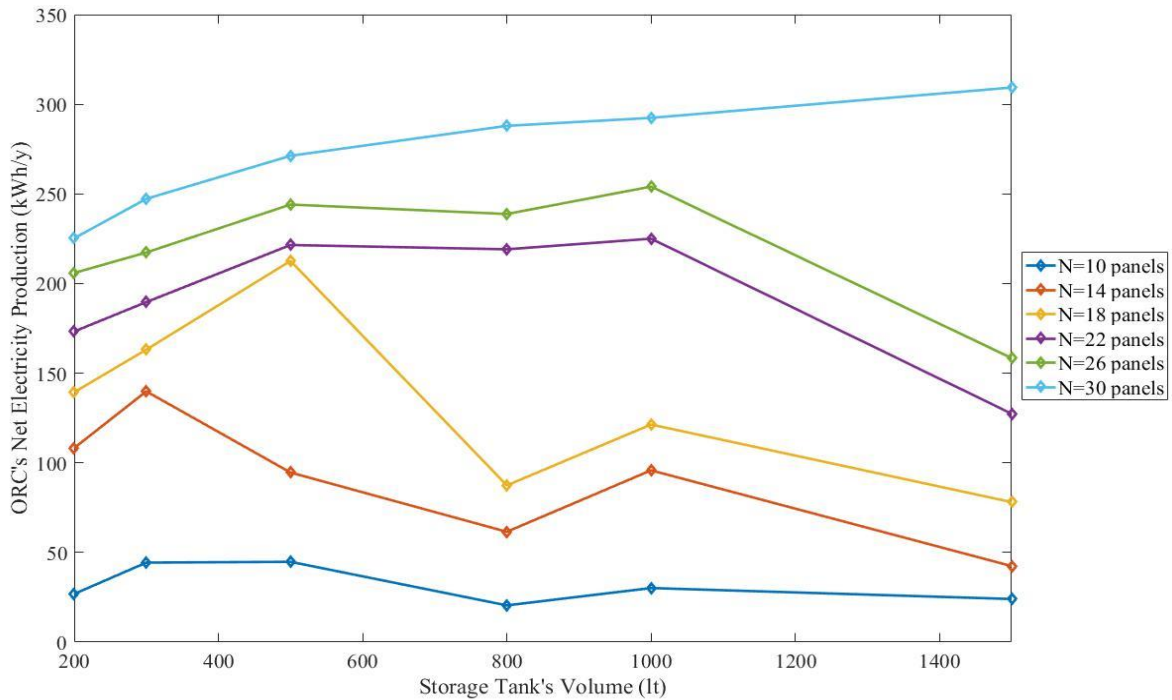


Figure 4.1 ORC's Net Electricity Production as a function of the number of PVT modules and the volume of storage tank in Athens

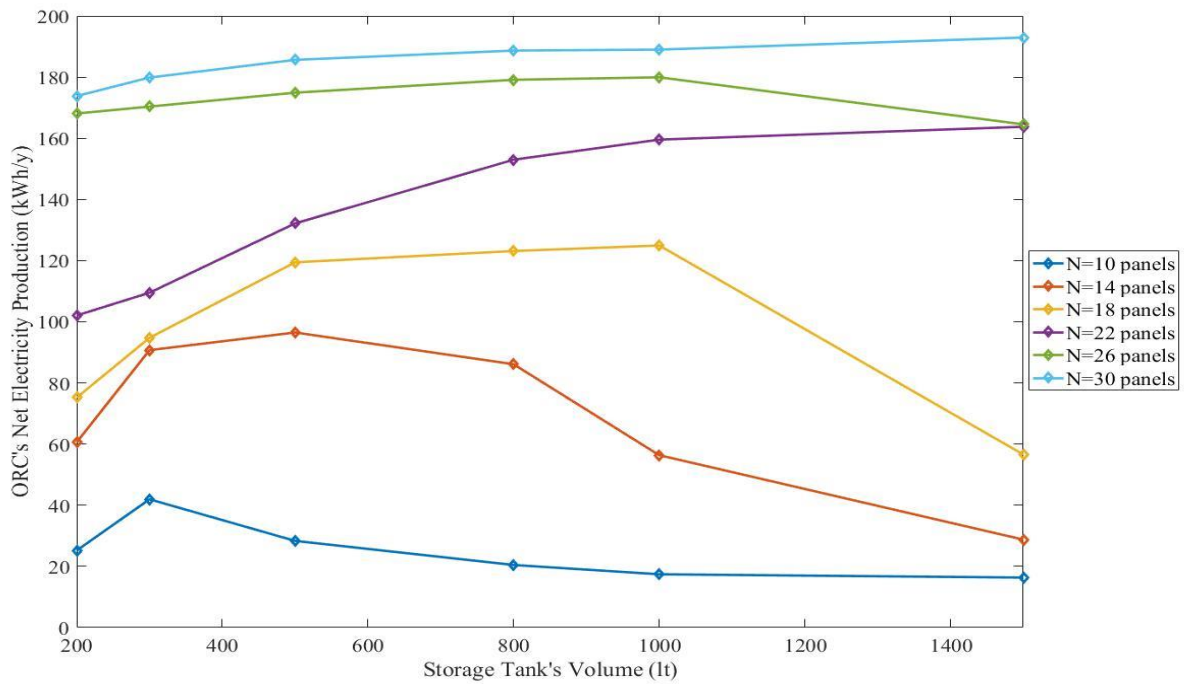


Figure 4.2 ORC's Net Electricity Production as a function of the number of PVT modules and the volume of storage tank in Naples

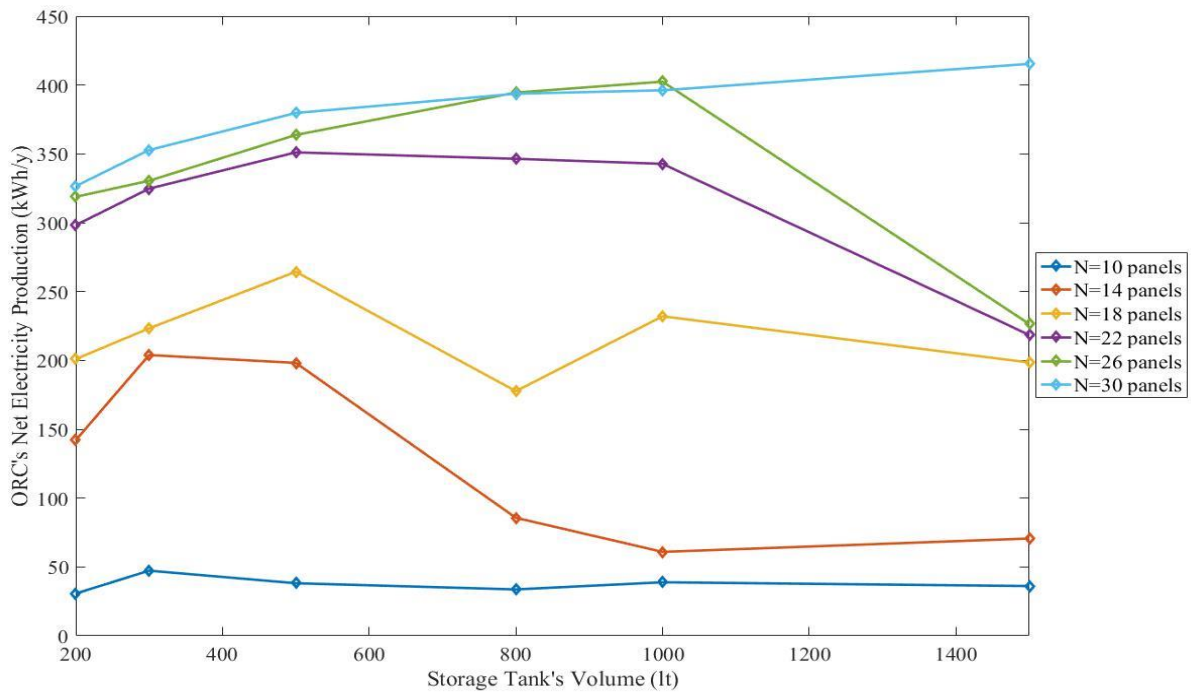


Figure 4.3 ORC's Net Electricity Production as a function of the number of PVT modules and the volume of storage tank in Larnaca

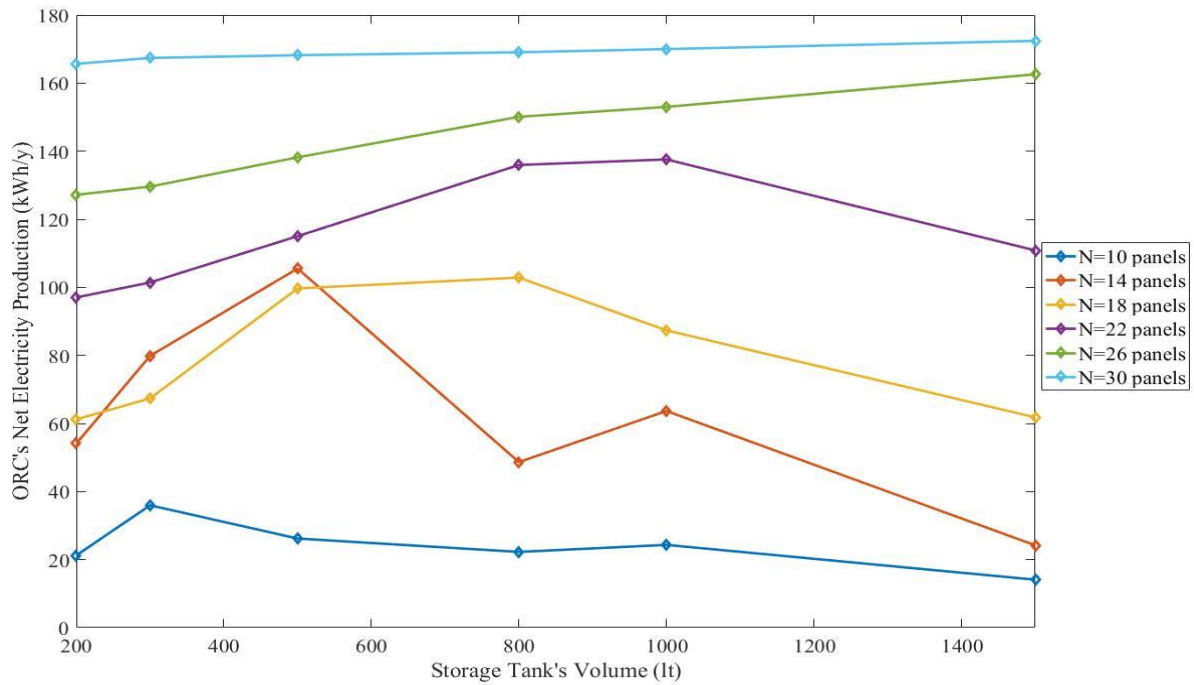


Figure 4.4 ORC's Net Electricity Production as a function of the number of PVT modules and the volume of storage tank in Madrid

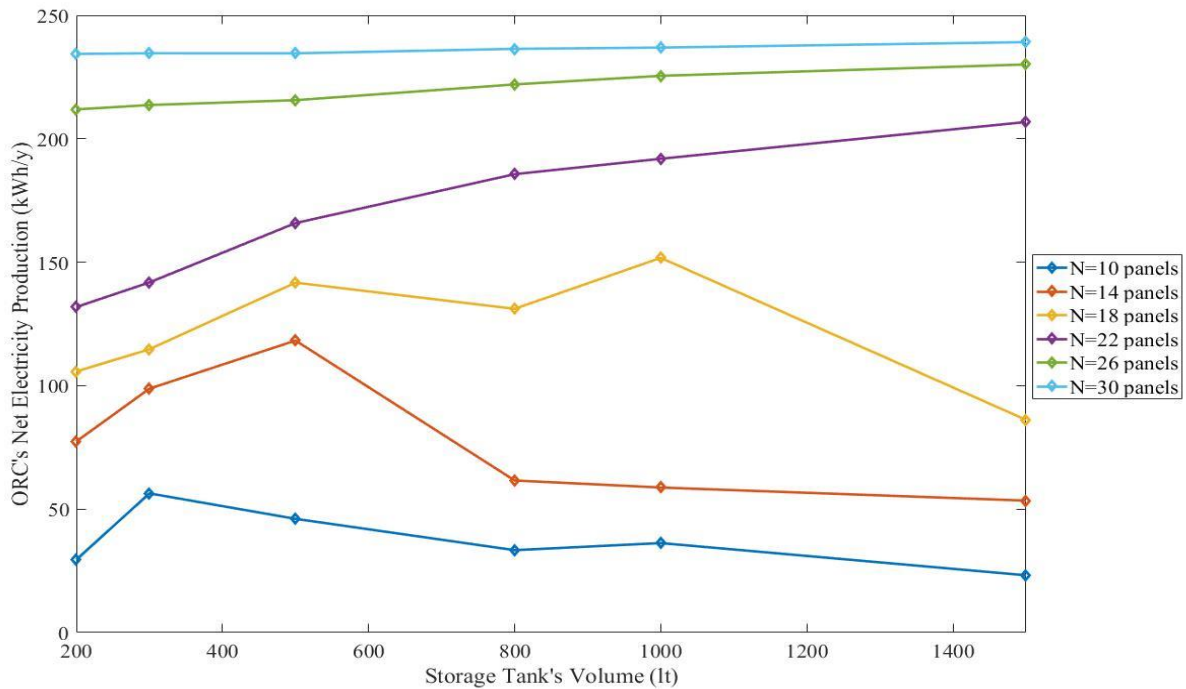


Figure 4.5 ORC's Net Electricity Production as a function of the number of PVT modules and the volume of storage tank in Lisbon

From the figures above, it can be concluded that by increasing the number of the PVT collectors, the net electricity production of the ORC is also increased. This is expected, as by increasing the collectors' surface, more solar radiation is utilized. There are two cases in Larnaca and Madrid that this rule does not apply. Moreover, as far as the volume of the storage tank is concerned, a conclusion cannot be drawn. It can be observed that for a small number of PVT modules, the net electricity production is maximized at a volume of storage tank equal to $V_{st} = 300 \text{ lt}$, while for a medium number of panels it is maximized at volumes equal to $V_{st} = 500 \text{ or } 800 \text{ lt}$. In the case of the maximum number of panels, the maximum electric production is observed with the maximum volume of storage tank examined. Nevertheless, these observations differ from city to city and thus a general conclusion cannot be drawn. Last but not least, as far as the impact of the meteorological data of every city is concerned, the ORC system produces the most electricity in Larnaca ($E_{el,net,ann} = 415.39 \text{ kWh/y}$) and the least in Madrid ($E_{el,net,ann} = 172.41 \text{ kWh/y}$) as it can be seen at Table 4.2, for the maximum volume of storage tank and number of PVT panels.

Table 4.2 Maximum net electricity production in every city with R152a as the working fluid of the ORC

City	Net Electricity Production (kWh/y)
Athens	309.32
Naples	192.93
Larnaca	415.39
Madrid	172.41
Lisbon	239.15

Another interesting result is the maximum net electricity production of all examined working fluids in every city. The maximum production for all working fluids and cities requires the maximum number of PVT modules as well as the biggest volume of the storage tank. The results of the maximization of electrical energy produced by the ORC by every refrigerant are depicted at Figures 4.6 – 4.10 that follow. From these figures, it is visible that in every city R152a leads as the most efficient working fluid with R1234ze and R134a following. On the other hand, R410a shows the least electricity production in every city followed by Propylene. These results were expected as the aforementioned refrigerants pose the highest and lowest efficiencies respectively at the off-design simulation, as shown at Table 3.18. The rest of the studied working fluids are characterized by similar electricity production in each location.

Furthermore, as mentioned before for R152a, all refrigerants show the highest production in Larnaca and the least one in Madrid, showing that the ambient conditions play a vital role to the viability of an ORC system powered by PVT modules.

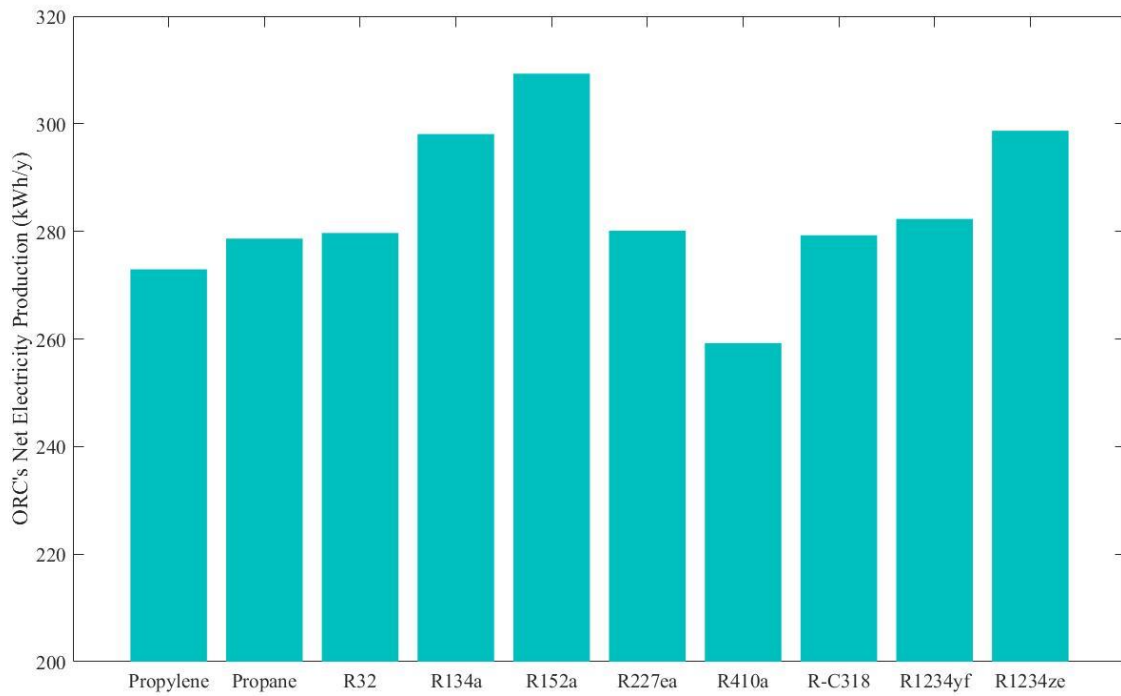


Figure 4.6 ORC's maximum net electricity production for the examined working fluids in Athens

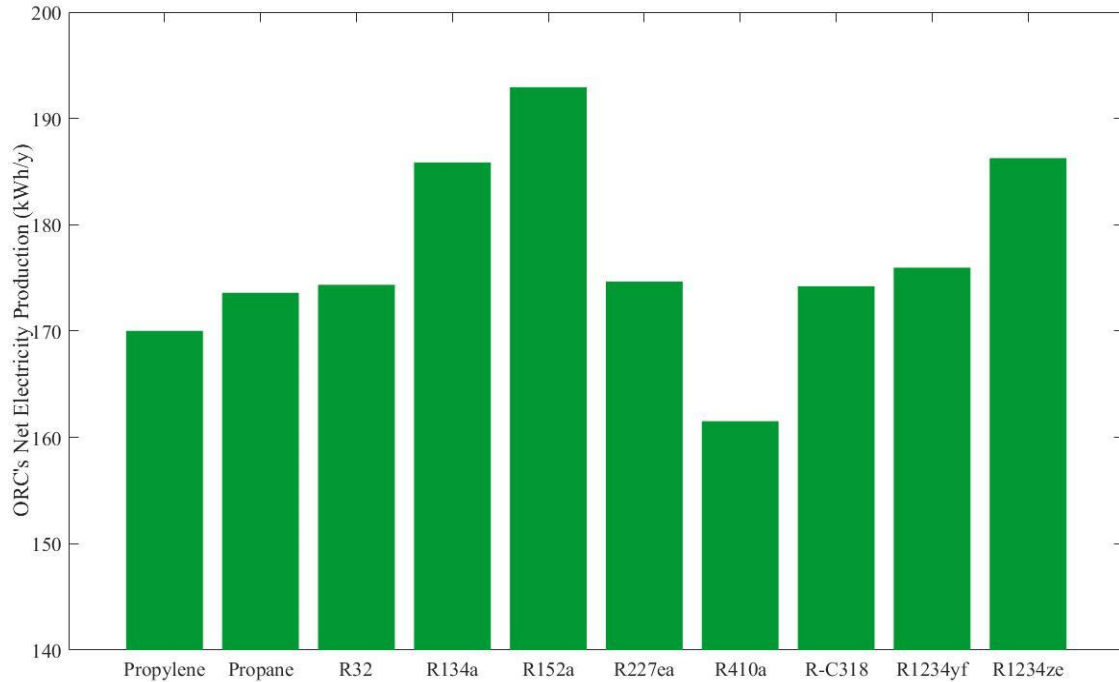


Figure 4.7 ORC's maximum net electricity production for the examined working fluids in Naples

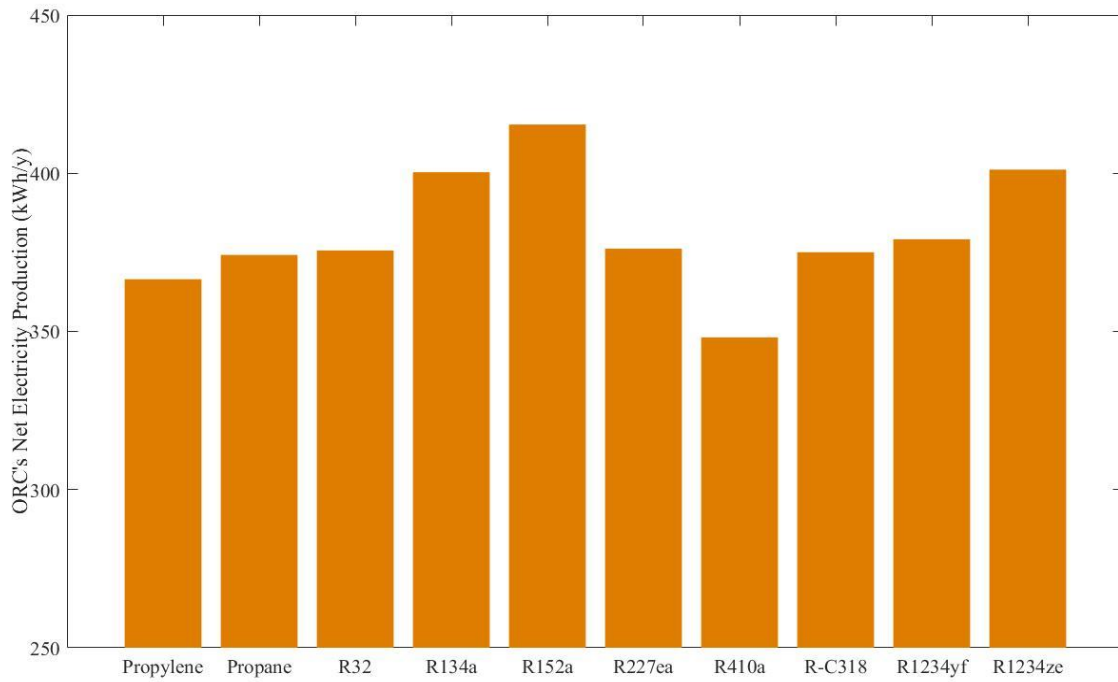


Figure 4.8 ORC's maximum net electricity production for the examined working fluids in Larnaca

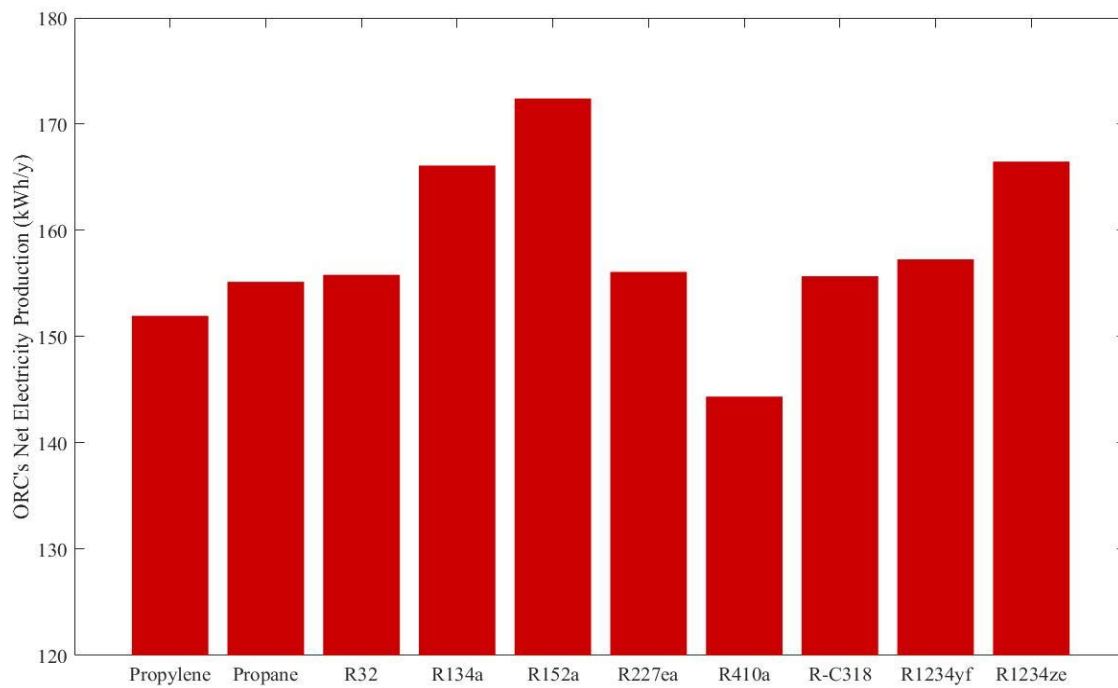


Figure 4.9 ORC's maximum net electricity production for the examined working fluids in Madrid

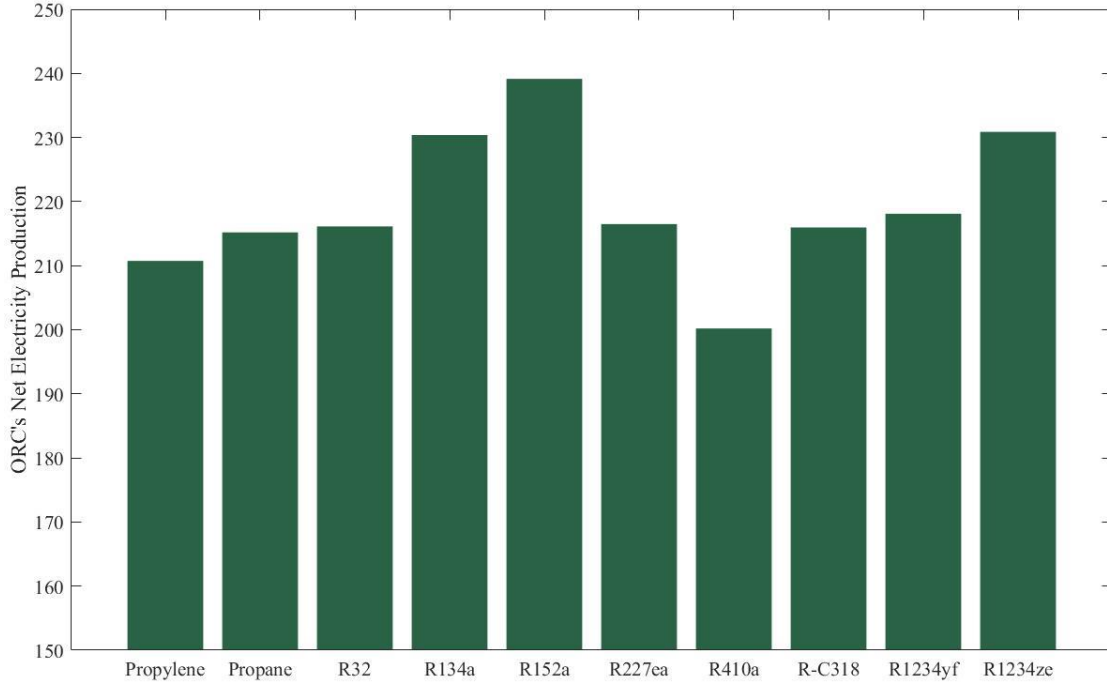


Figure 4.10 ORC's maximum net electricity production for the examined working fluids in Lisbon

The calculation of the exergetic and the net electric efficiency of the whole PVT-ORC system is of great importance. For this purpose, the following equations are used respectively:

$$\eta_{ex,sys} = \frac{E_{el,net,ORC} + E_{el,PV}}{Ex_{sol}} \quad (4.2)$$

$$\eta_{el,net,sys} = \frac{E_{el,net,ORC} + E_{el,PV}}{E_{sol}} \quad (4.3)$$

where $E_{el,net,ORC}$ is the annual net electricity production by the ORC, $E_{el,PV}$ is the annual electricity production by the PV modules and Ex_{sol} is the solar exergy calculated by the following equation:

$$Ex_{sol} = \sum_{i=1}^{i=8760} \left(1 - \frac{T_{amb}(i)}{T_{sol}} \right) * I_T(i) * A_{col} \quad (4.4)$$

where $T_{sol} = 5770K$ is the sun's temperature [79].

The annual solar energy E_{sol} is calculated as follows:

$$E_{sol} = \sum_{i=1}^{i=8760} I_T(i) * A_{col} \quad (4.5)$$

According to the calculations of subchapter 2.1, the annual electric production of the PV modules in each examined city is listed at Table 4.3 that follows.

Table 4.3 *Annual PV electricity production per square meter in each city*

City	Annual PV electricity production (kWh/m^2y)
Athens	335.717
Naples	292.809
Larnaca	380.388
Madrid	275.922
Lisbon	332.753

Thus, the exergetic and net electric efficiency of the system can be calculated. The calculations are decided to be made for the maximum number of PVT modules and the maximum volume of the storage tank as the production of the ORC is maximized.

Since, the most electricity is produced by the PV modules instead of the ORC, these efficiencies differ slightly for the different working fluids in each city. This is why, in Table 4.4 only the maximum and minimum values of these variables are shown as well as the refrigerants that achieve these efficiencies.

Table 4.4 *Maximum and minimum exergetic and net electric efficiencies of the system for each city*

Exergetic Efficiency				
City	Maximum (%)	Working Fluid	Minimum (%)	Working Fluid
Athens	20.598	R152a	20.479	R410a
Naples	20.293	R152a	20.207	R410a
Larnaca	20.820	R152a	20.678	R410a
Madrid	20.256	R152a	20.175	R410a
Lisbon	20.414	R152a	20.321	R410a
Net Electric Efficiency				
City	Maximum (%)	Working Fluid	Minimum (%)	Working Fluid
Athens	19.543	R152a	19.430	R410a
Naples	19.258	R152a	19.177	R410a
Larnaca	19.749	R152a	19.614	R410a
Madrid	19.229	R152a	19.152	R410a
Lisbon	19.378	R152a	19.288	R410a

As it was anticipated, R152a shows the maximum exergetic and net electric efficiency of the system for each city, as it shows the highest electric efficiency of the ORC cycle in off-design simulation. R410a shows the lowest efficiencies, as it is characterized by the lowest electric efficiency of the ORC cycle respectively. The values of the exergetic and net electric efficiency of the system are high because of the efficient energy conversion of the solar radiation by the PV panels as well as the utilization of the heat recovered by the thermal collectors through the evaporator of the ORC.

Chapter 5. Economic Analysis

Since the energetic and exergetic analysis of the system have been completed, it is essential to assess the economic viability of the application. For this purpose, three investment performance indexes are used: Levelized Cost of Energy (LCOE), Net Present Value (NPV) and Payback Period (PBP).

First step towards the economic assessment of the system is the calculation of its investment cost, which is equal to the sum of the cost of all of its components.

PVT Modules

According to DualSun [47] the cost of one PVT module is equal to $C_{PVT,mod} = 550$ €. Thus, depending on the scenario, the cost of the photovoltaic/thermal collectors is calculated from the following equation:

$$C_{PVT} = N_{PVT} * C_{PVT,mod} \quad (5.1)$$

Solar Storage Tank

For the estimation of the cost of the solar tank, an equation based on data fitting from OÜ Cerbos [80] is used:

$$C_{st} = 231.87 + 312.97 * V_{st} \quad (5.2)$$

Piping of the solar circuit

It was assumed that for the connection of the thermal collectors of the PVT modules with the solar storage tank and the ORC, the selection of 25 m of pipes with a Ø23 diameter would suffice. For the estimation of the cost of the piping, an equation proposed by Lecompte et al. [76] is used:

$$C_{pip,sol} = (0.891 + 0.21 * D_{pip}) * L_{pip} \quad (5.3)$$

with D_{pip} to be measured in mm.

The total investment cost of the system is equal to the sum of the cost of the PVT modules, the solar storage tank, the piping of the solar circuit and the ORC, which was elaborated at subchapter 3.4.

$$IC = C_{PVT} + C_{st} + C_{pip,sol} + C_{tot,ORC} \quad (5.4)$$

In Figure 5.1, a bar diagram of the investment cost for each examined working fluid is depicted for the case scenario of maximum number of PVT modules and minimum volume of solar storage tank, as this combination is proven to generally be the most economically viable depending on the performance indexes calculated. Due to its high cost, R-C318 is not a viable choice as a working fluid, and thus it is not presented in the results of the economic analysis.

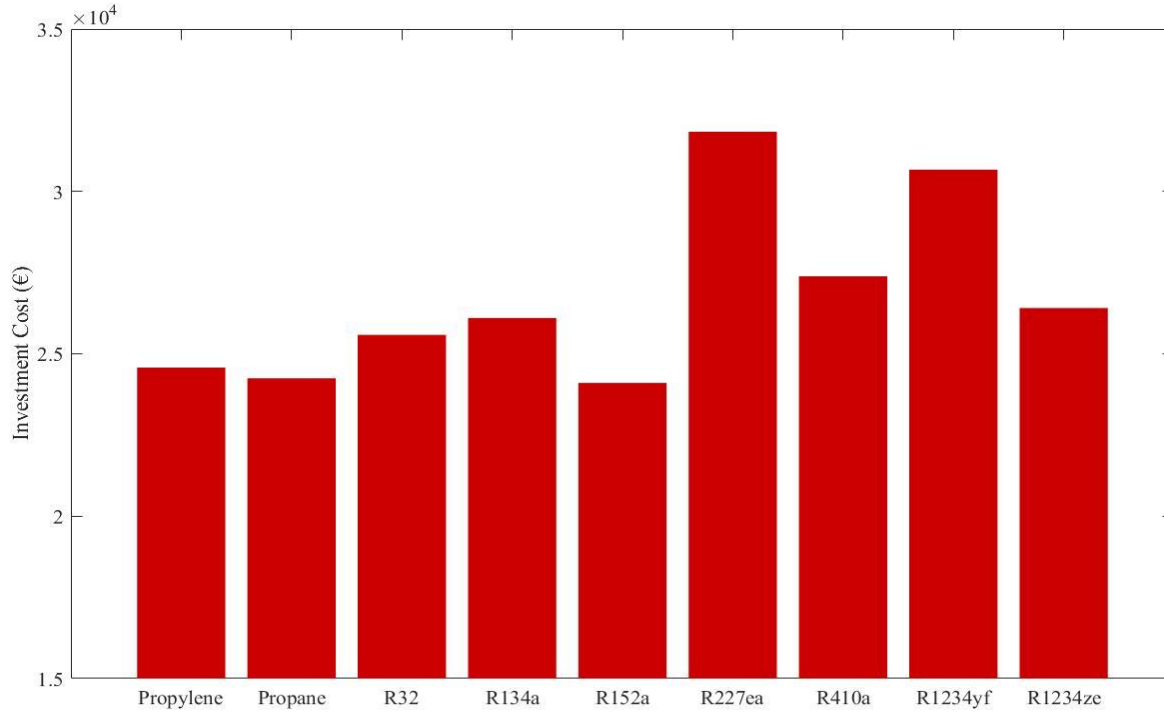


Figure 5.1 Investment Cost of the examined working fluids for the best case scenario

It is apparent, that as far as the investment cost is concerned, R152a, Propane and Propylene are the best choices while R227ea and R1234yf are the most expensive ones from the remaining working fluids. This conclusion was anticipated, as these fluids have the lowest and highest prices respectively, as it can be seen in Table 3.6. The total investment cost of all working fluids for the aforementioned combination of number of PVT modules and storage tank's volume is listed at Table 5.1:

Table 5.1 Investment Cost of the examined working fluids

Refrigerant	Investment Cost (€)
Propylene	24576.31
Propane	24247.05
R32	25581.62
R134a	26100.19
R152a	24104.55
R227ea	31838.26
R410a	27387.78
R-C318	81061.34
R1234yf	30670.86
R1234ze	26407.98

In Figure 5.2, a pie chart of the cost of each component is shown as a fraction of the total investment cost, when R152a is used as the working fluid of the cycle as it is proven to be the

most economically viable choice. Since, the cost of the PVT, the piping and the solar storage tank remain the same regardless of the used refrigerant, the percentages of the components depend on the market price of the working fluids. Thus, according to Table 3.6, the percentage of the ORC cycle will be the lowest in the case of Propane and the highest in the case of R227ea, if R-C318 is excluded.

In Figure 5.3, the same procedure is followed for the analysis of the cost of every component of the ORC when R152a is used. In the case of R152a, the most expensive component is the pump of the cycle, while the control hardware, the evaporator, the condenser and the expander have similar percentages. The cost of the fluid is pretty low in this case (equal to 4%) as the price of R152a is low. Nevertheless, for the rest of the examined refrigerants, except for Propylene and Propane, this percentage is much higher as their market price is pretty high and the volume of the working fluid inside the cycle is equal to $V_{st} = 45 \text{ lt}$.

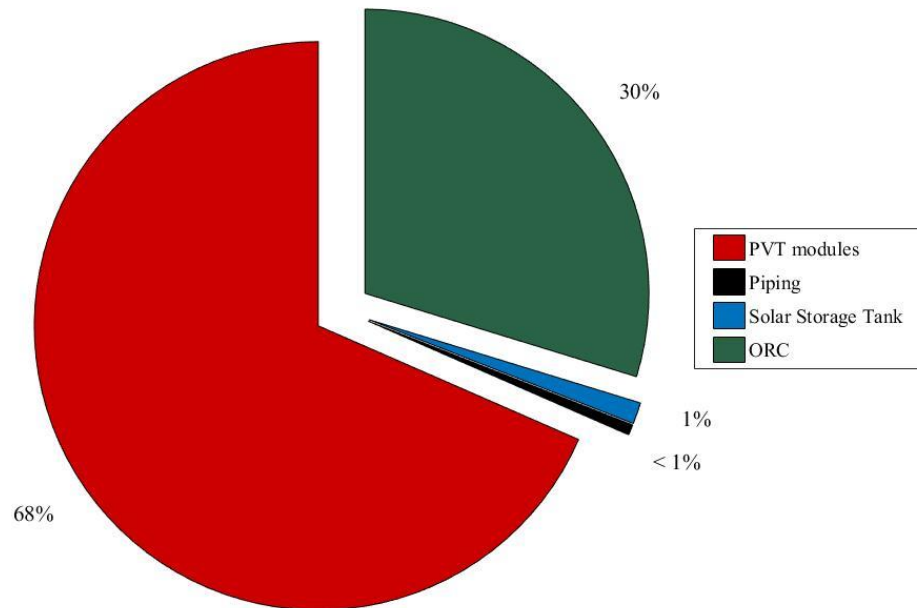


Figure 5.2 Analysis of the cost of each component of the system for the case of R152a

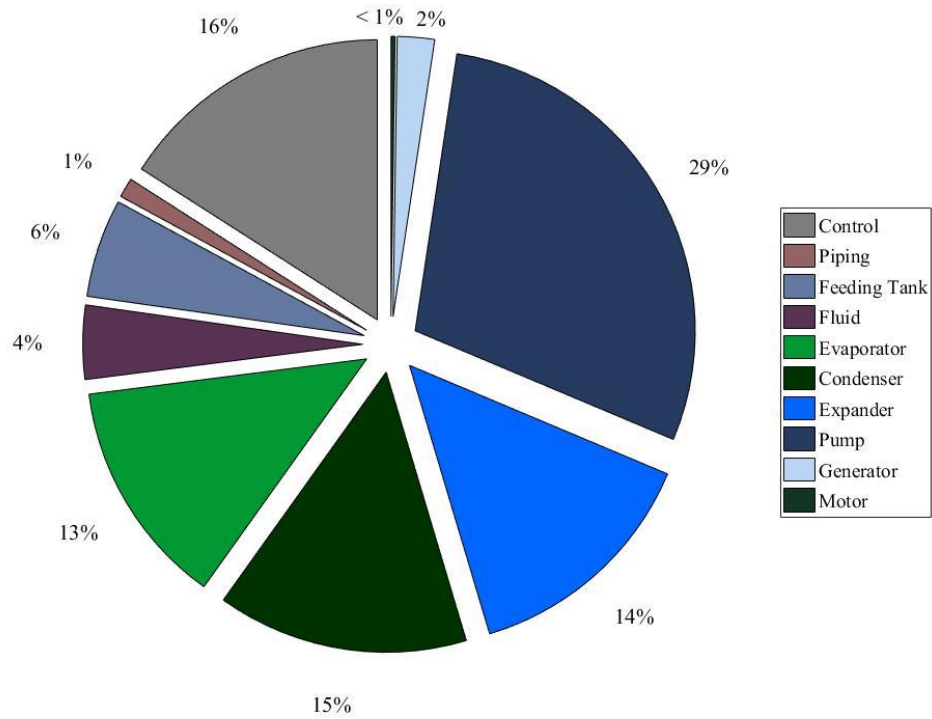


Figure 5.3 Analysis of the cost of each component of the ORC for the case of R152a

The next step towards the calculation of the aforementioned performance indexes is the estimation of the income of the application. For this purpose, at Table 5.2 the electricity prices of the second semester of 2018 for household and non-household consumers in the examined countries are listed, according to data acquired by Eurostat [81]. For the economic assessment of the system, the electricity prices of household consumers will be used as the study was made for the energy needs of a household.

Table 5.2 Electricity Prices in the examined countries on the second semester of 2018

City/Country	Household Price (€/kWh)	Non-Household Price (€/kWh)
Athens/Greece	0.1646	0.1059
Naples/Italy	0.2161	0.1434
Larnaca/Cyprus	0.2183	0.1811
Madrid/Spain	0.2477	0.1098
Lisbon/Portugal	0.2293	0.1170

5.1 Levelized Cost of Energy

Levelized Cost of Energy (LCOE) is a performance index used in energy applications which indicates the cost for the production of one electric kWh . LCOE is calculated through the next equation [82]:

$$LCOE = \frac{IC * R + OMC}{E_{el,net,tot}} \quad (5.5)$$

where IC is the investment cost, OMC is the annual operational and maintenance cost set to be equal to $OMC = 0.02 * IC$, $E_{el,net,tot}$ is the annual net electricity production by the PVT modules and the ORC and R is a coefficient calculated as follows:

$$R = \frac{i}{1 - (1 + i)^{-n}} \quad (5.6)$$

where $i = 6\%$ is the discount rate and $n = 20 \text{ years}$ is the expected lifetime of the investment.

In Figures 5.4 – 5.8 the minimum LCOE of all refrigerants in each examined city is depicted. In most cases, the lowest LCOE is achieved with the maximum collectors' surface studied ($A_{col} = 49.62 \text{ m}^2$) and the lowest volume of the storage tank ($V_{st} = 200 \text{ lt}$). In the city of Athens and Larnaca, the best combination for the minimization of LCOE is proven to acquire the maximum numbers of PVT modules and a storage tank's volume equal to $V_{st} = 300 \text{ lt}$ for R134a, R152a, R1234yf and R1234ze, as well as for R32 and R227ea only in Larnaca. Finally, for R-C318, which is not shown in figures due to its high value ($LCOE_{R-C318,Athens} = 0.5146 \text{ €/kWh}$), the minimum value of LCOE in Athens and Larnaca is achieved for the maximum number of PVT collectors and a solar storage tank with volume equal to $V_{st} = 500 \text{ lt}$.

The fact that the minimization of the LCOE demands the highest collectors' surface examined was expected, as the cost of the PV production per square meter of PV modules remains the same, while the production of the ORC is increased. Furthermore, small storage tanks are preferred as the increased production offered by an increase of their volume does not compensate for their cost raise.

As expected, R152a has the lowest value of LCOE with Propane and Propylene following as they have the best combination of price market and net electric efficiency, while R227ea and R1234yf have the highest values of LCOE due to their high market prices.

In Figures 5.4 – 5.8 the LCOE of standalone PV operation is shown in order to compare with the coupling of the PVT-ORC system. It is apparent, that this cost is much lower than those with the addition of the ORC. Thus, it can be concluded that the use of PVT modules as the hot stream for the evaporator of an ORC is not an economically viable solution given that it utilizes on waste heat of maximum temperature equal to $T_{hs,max} = 80^\circ\text{C}$ with an approximate net electrical efficiency $n_{el,net,ORC} \cong 6\%$.

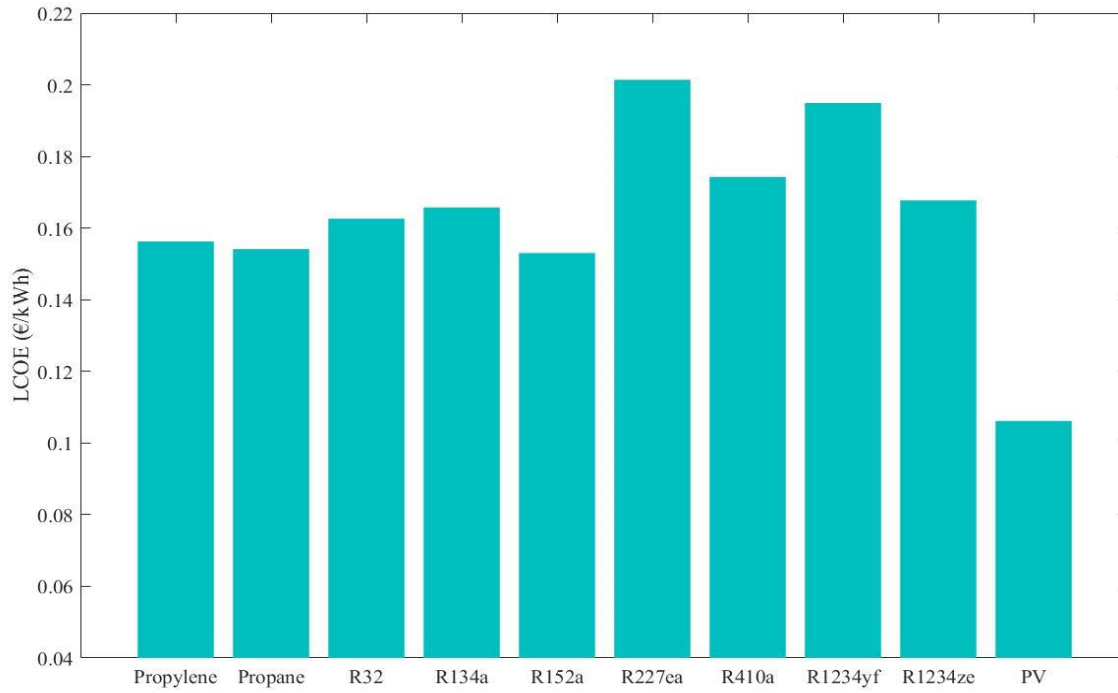


Figure 5.4 *LCOE of the examined working fluids and PV standalone operation in Athens*

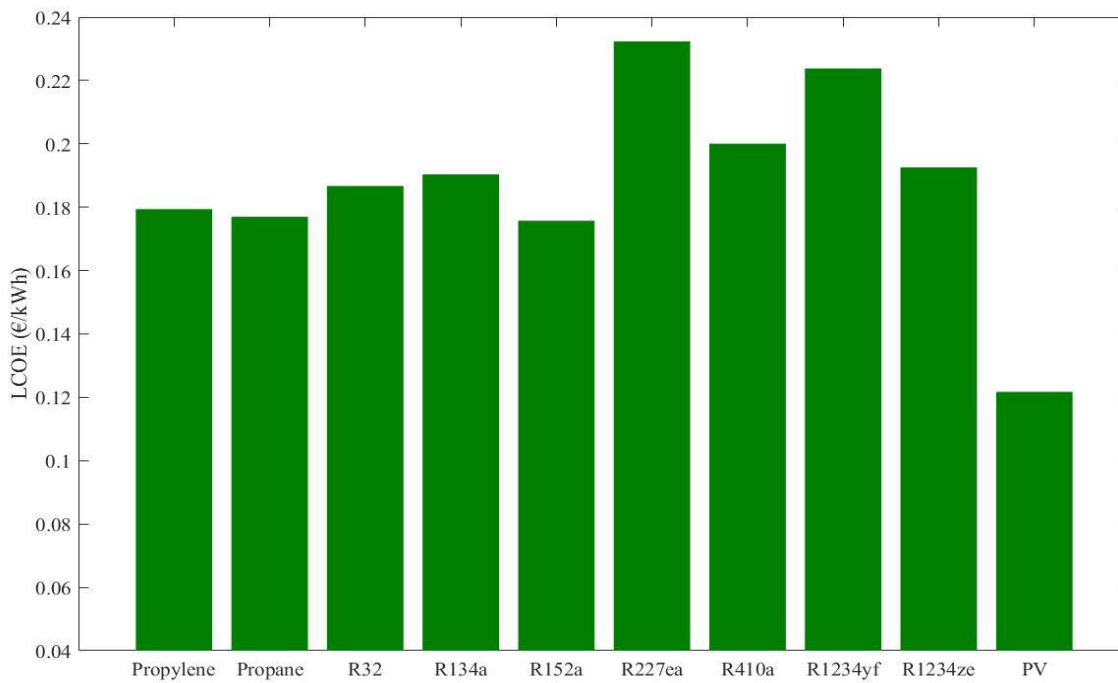


Figure 5.5 *LCOE of the examined working fluids and PV standalone operation in Naples*

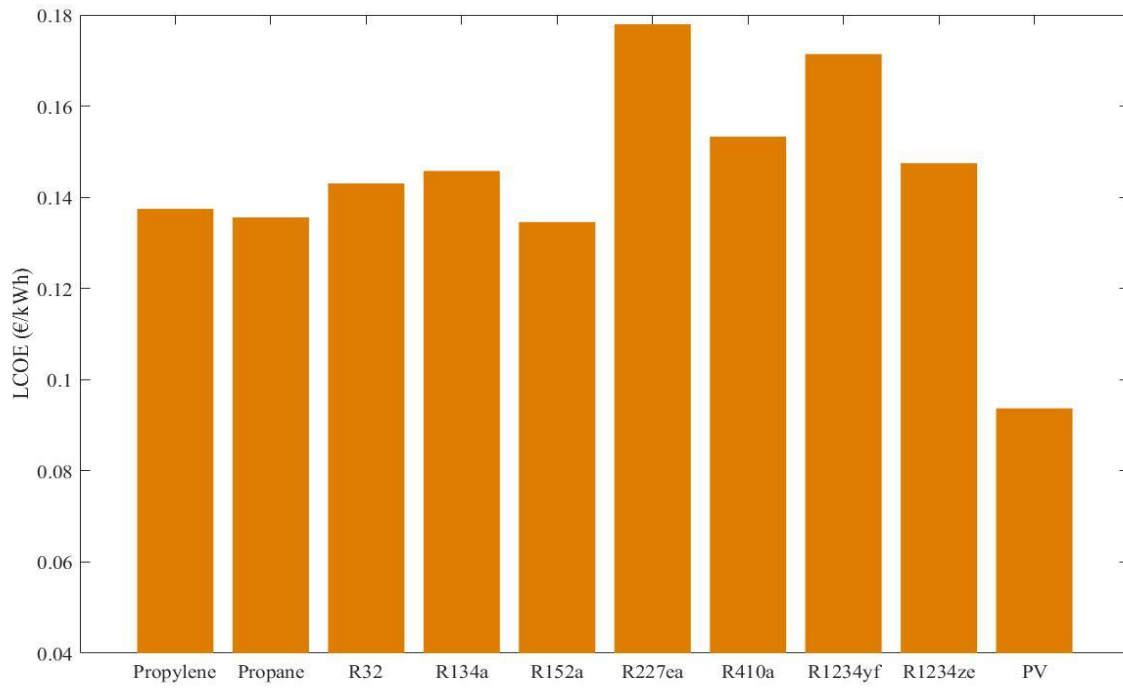


Figure 5.6 *LCOE of the examined working fluids and PV standalone operation in Larnaca*

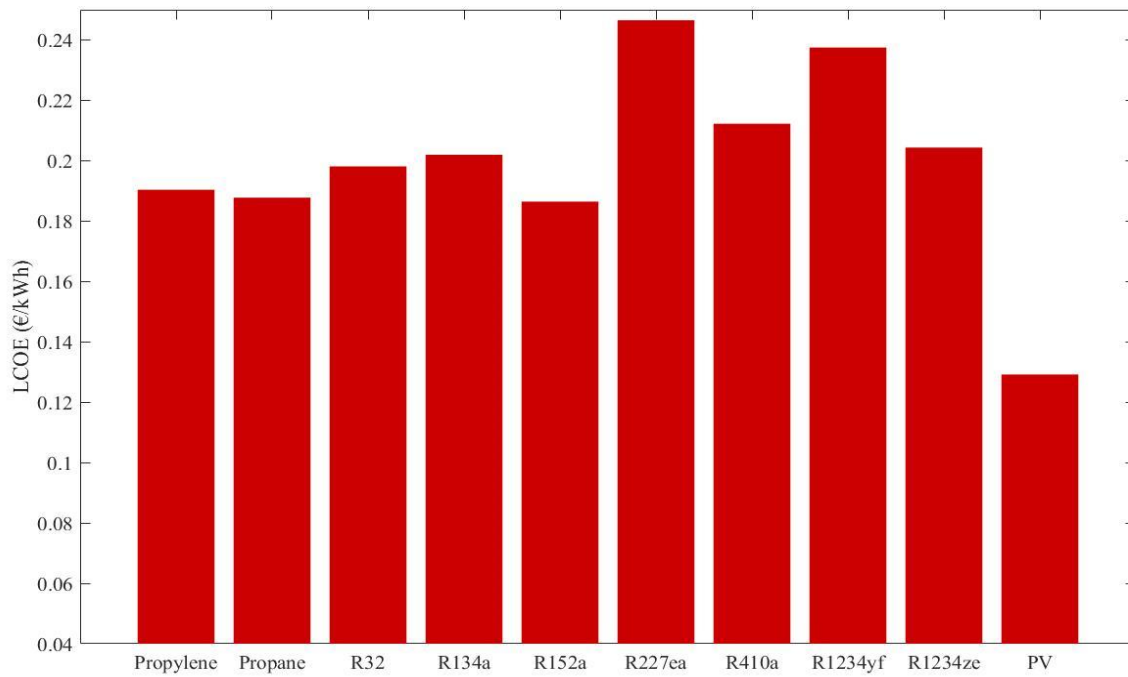


Figure 5.7 *LCOE of the examined working fluids and PV standalone operation in Madrid*

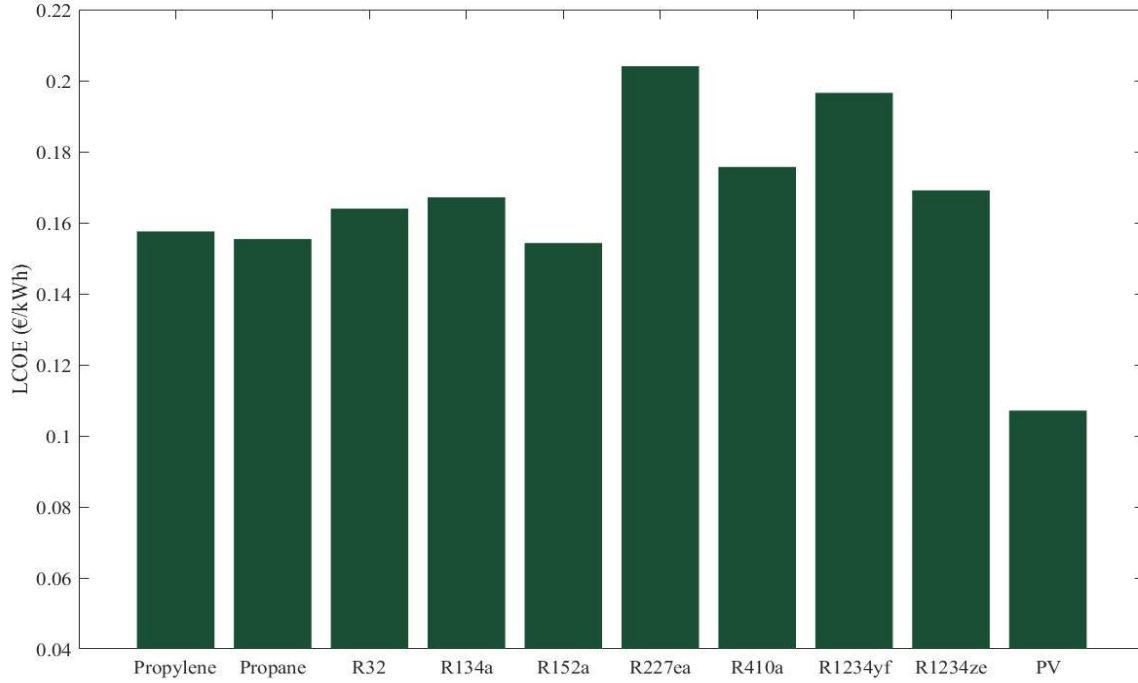


Figure 5.8 LCOE of the examined working fluids and PV standalone operation in Lisbon

As expected, Larnaca has the minimum LCOE value and Madrid the maximum, as the net electric production is the highest and the lowest in these two cities respectively.

5.2 Net Present Value

Net Present Value (NPV) is the difference between the present value of cash inflows and outflows over a period of time. As aforementioned, the expected lifetime of the system is set to be equal to $n = 20$ years and the discount rate equal to $i = 6\%$. The NPV is calculated using the following equation:

$$NPV = -IC + \sum_{n=1}^{n=20} (E_{el,net,tot} * pr_{el} - OMC) * (1 + i)^{-n} \quad (5.7)$$

where pr_{el} is the price of electricity for household consumers according to Table 5.2.

In Figures 5.9 – 5.13 the maximum NPV of all refrigerants in each examined city is depicted. In most cases, the highest NPV is achieved with the maximum collectors' surface studied ($A_{col} = 49.62 \text{ m}^2$) and the lowest volume of the storage tank ($V_{st} = 200 \text{ lt}$). In the city of Athens, the best combination for the maximization of NPV is proven to acquire the maximum number of PVT modules and a storage tank's volume equal to $V_{st} = 300 \text{ lt}$ for R134a, R152a and R1234ze.

In Larnaca, the best combination for all refrigerants is the maximum number of PVT modules and a solar storage tank with volume capacity equal to $V_{st} = 300 \text{ lt}$.

The fact that the maximization of the NPV demands the highest collectors' surface examined was expected, as the cost of the PV production per square meter of PV modules remains the same, while the production of the ORC is increased. Furthermore, small storage tanks are preferred as the increased production offered by an increase of their volume does not compensate for their cost raise.

As expected, R152a has the highest value of NPV with Propane and Propylene following as they have the best combination of price market and net electric efficiency, while R227ea and R1234yf have the lowest values of NPV due to their high market price. Moreover, negative NPV values signify that these systems are not economically viable based on their expected lifetime.

In Figures 5.9 – 5.13 the NPV of standalone PV operation is shown in order to compare with the coupling of the PVT-ORC system. It is apparent, that this value is much higher than those with the addition of the ORC. Thus, it can be concluded that the use of PVT modules as the hot stream for the evaporator of an ORC is not an economically viable solution given that it utilizes on waste heat of maximum temperature equal to $T_{hs,max} = 80^\circ\text{C}$ with an approximate net electrical efficiency $n_{el,net,ORC} \cong 6\%$.

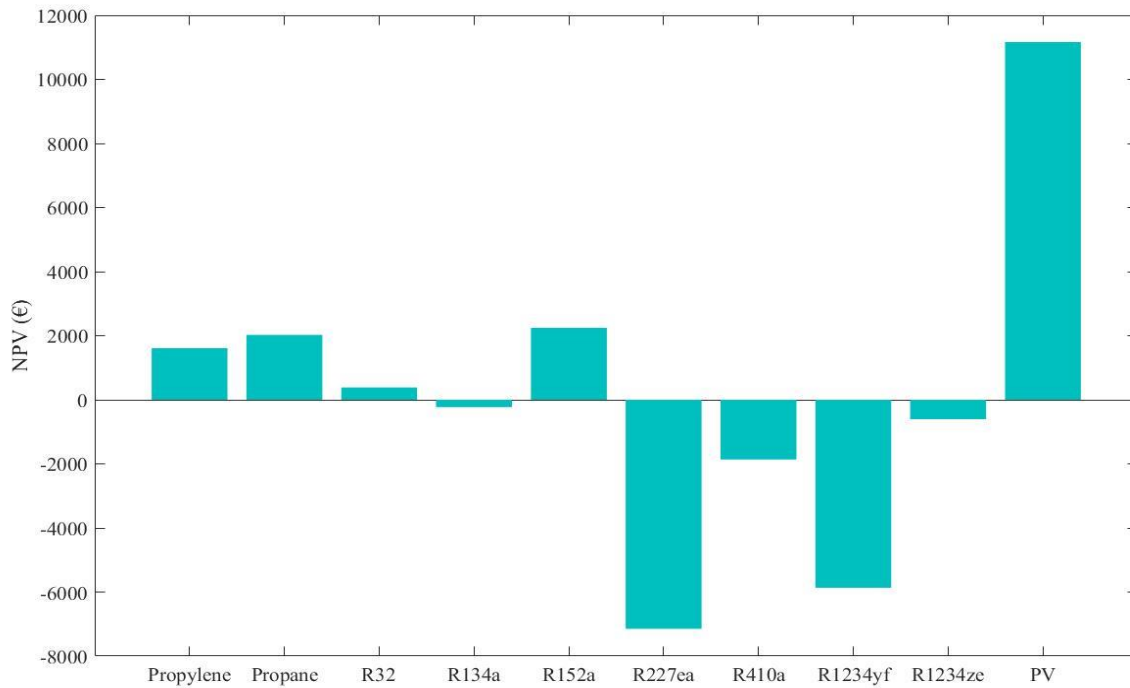


Figure 5.9 NPV of the examined working fluids and PV standalone operation in Athens

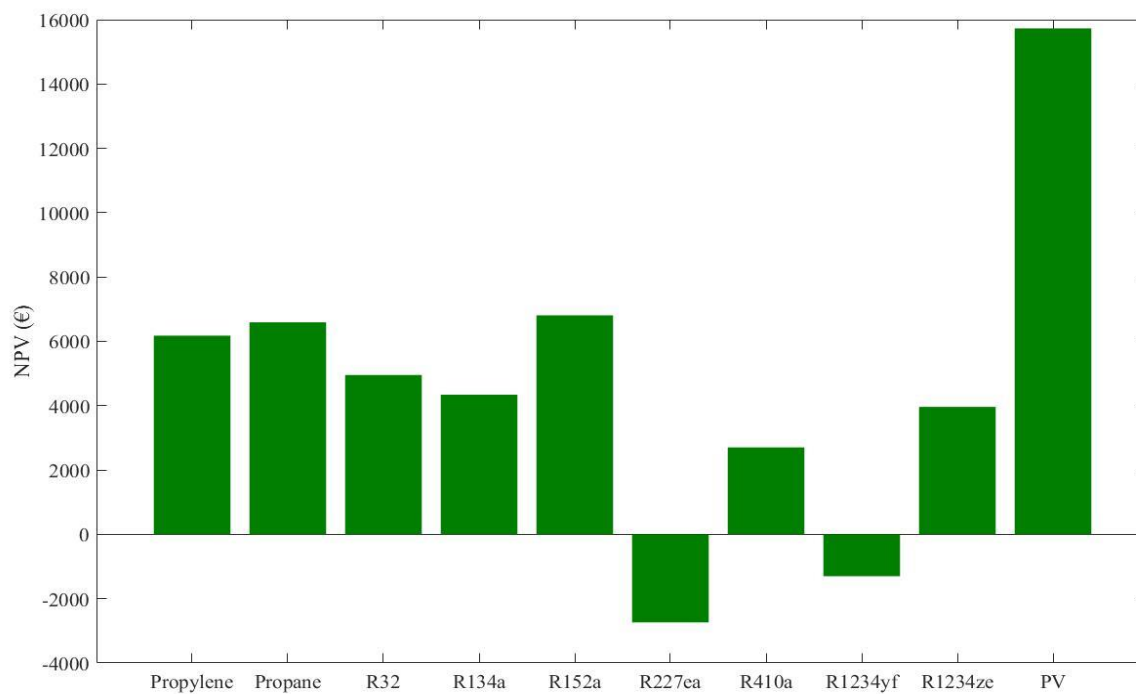


Figure 5.10 NPV of the examined working fluids and PV standalone operation in Naples

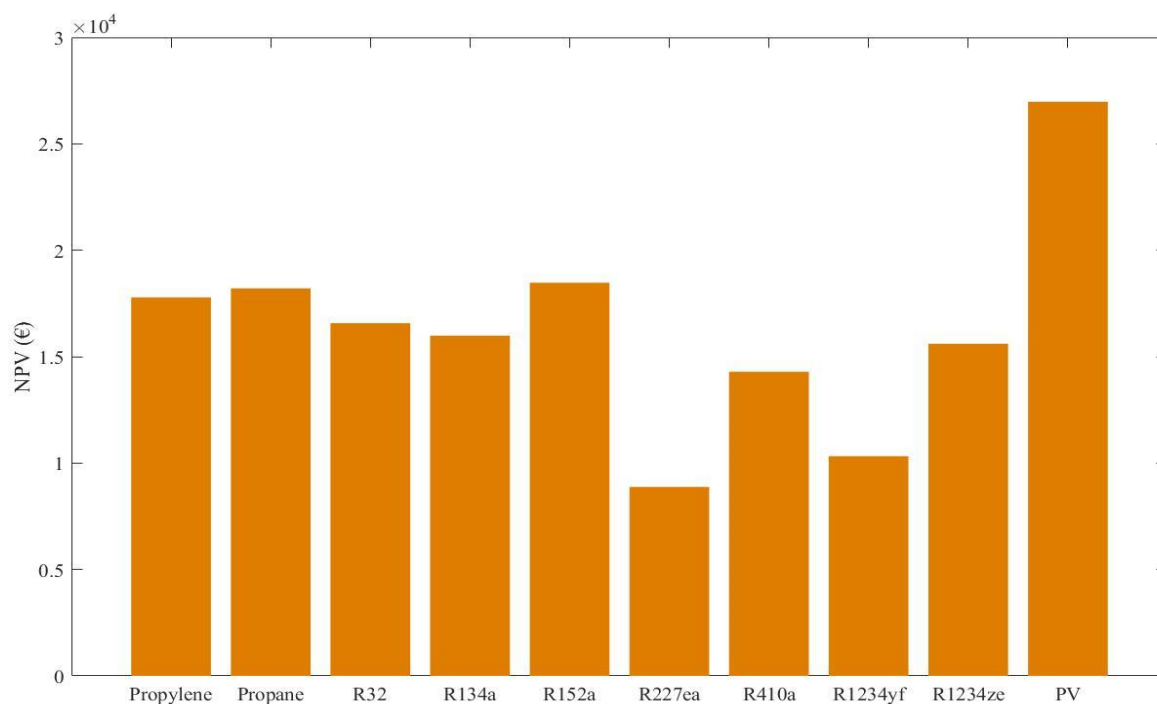


Figure 5.11 NPV of the examined working fluids and PV standalone operation in Larnaca

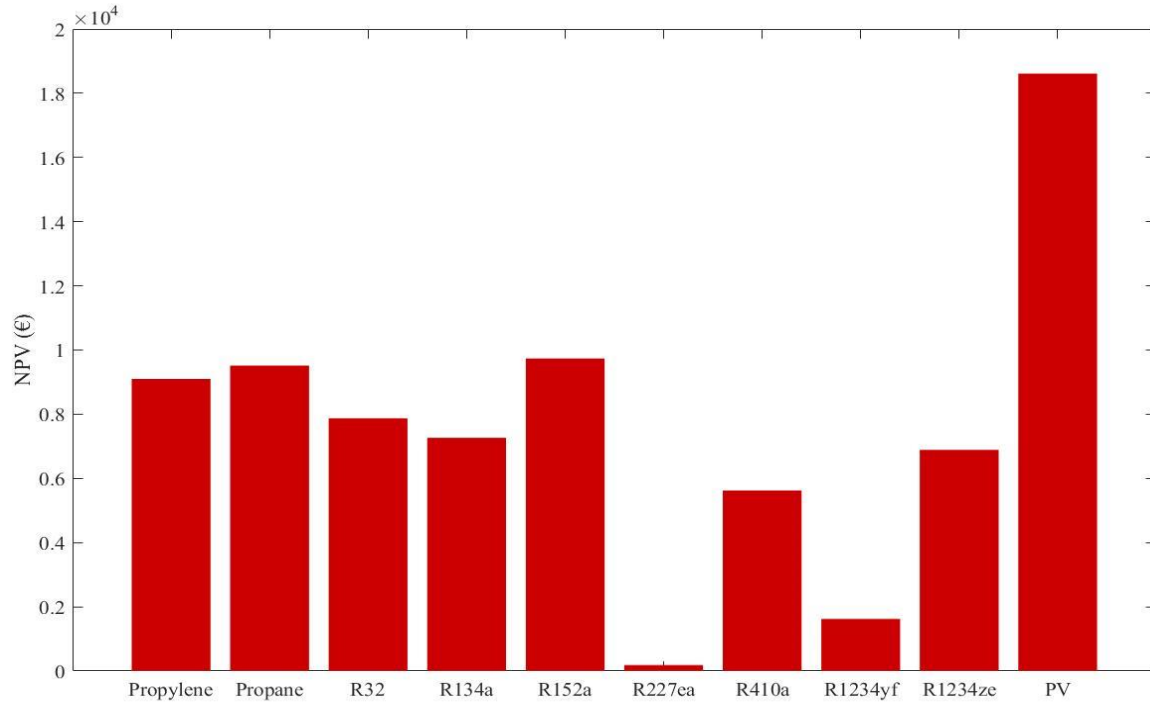


Figure 5.12 NPV of the examined working fluids and PV standalone operation in Madrid

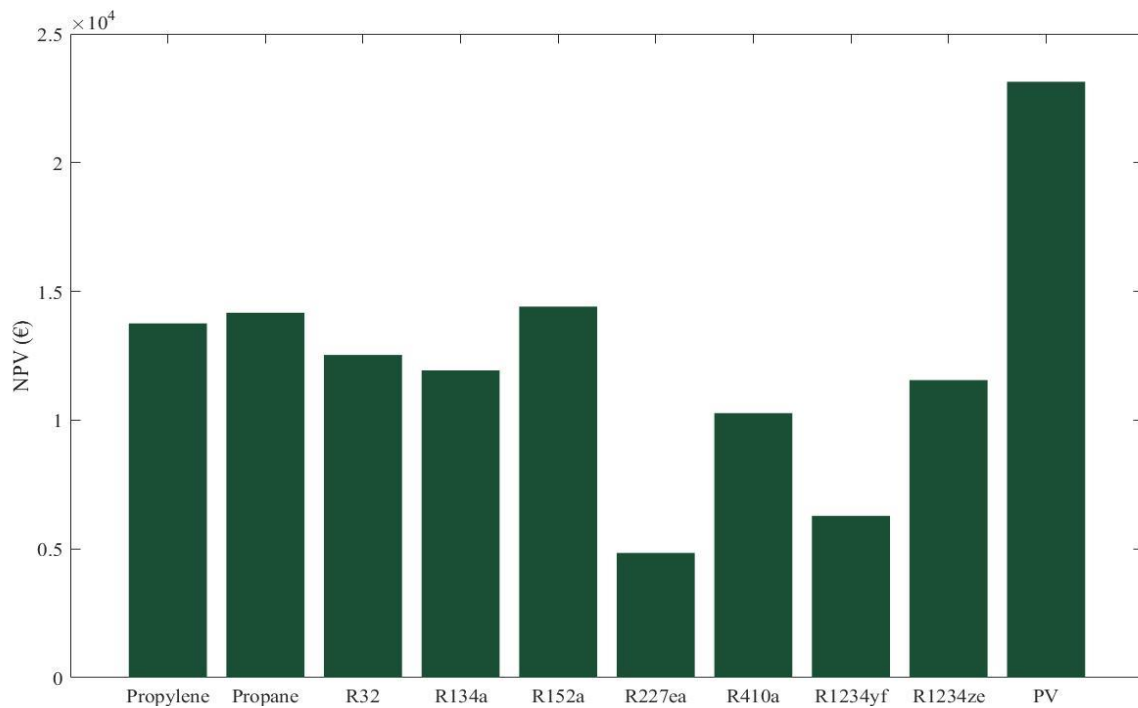


Figure 5.13 NPV of the examined working fluids and PV standalone operation in Lisbon

The highest NPV values are observed in Larnaca as the net electric production is the highest and the electricity price for the household consumers is high as well. On the other hand, the lowest NPV values are observed in Athens despite having the second highest electricity production, since it is the city with the lowest electricity price and thus the annual income of the system is pretty low compared to the rest of the locations.

In Figure 5.14 the NPV values of R152a are shown if the system is used for non-household applications and thus the electricity price is taken equal to the second column of Table 5.2. From this figure, it can be concluded that the price of the produced electricity is a main variable for the viability of the application and thus the selection of the location of the system should be examined thoroughly. Since, the ORC is powered by PVT modules, countries with high solar radiation all year round and high electricity prices are best suited for this application. This is the reason why Larnaca is the only location with a positive NPV value. Nevertheless, the electricity prices tend to change every semester, thus a precise calculation of the NPV is not feasible.

In Madrid, the highest NPV value, although still negative, is acquired with the minimum number of PVT modules and solar storage tank's volume capacity ($NPV_{min, Madrid} = -10336.4 \text{ €}$). Nevertheless, in Figure 5.14 the NPV value of the combination of Figure 5.12 is selected in order to compare the results.

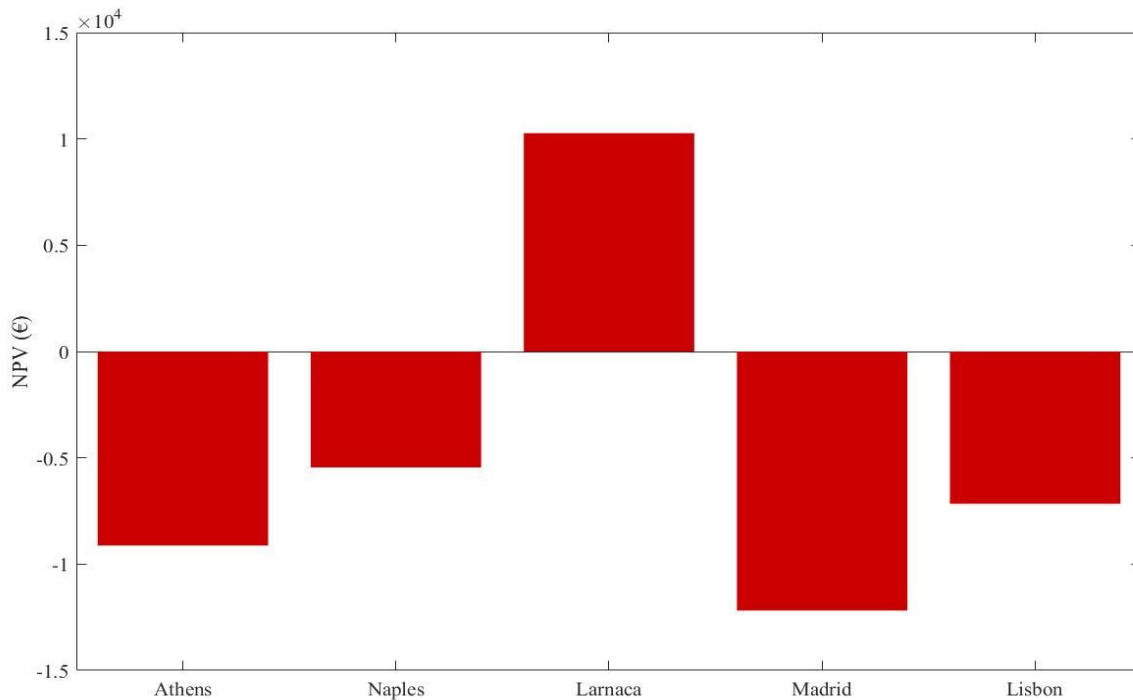


Figure 5.14 NPV of R152a in each examined city for non-household consumers

5.3 Payback Period

Payback Period (PBP) refers to the amount of time it is needed to recover the cost of an investment. As mentioned before, the expected lifetime of the system is set to be equal to $n = 20$ years and the discount rate equal to $i = 6\%$. Thus, if the PBP is greater than 20 years, the application is not economically sustainable for the expected lifetime. The PBP is calculated using the following equation:

$$0 = -IC + \sum_{n=1}^n (E_{el,net,tot} * pr_{el} - OMC) * (1 + i)^{-n} \quad (5.8)$$

where PBP is equal to the year n in which the net cash flow of the investment is null.

In Figures 5.15 – 5.19 the minimum PBP of all refrigerants in each examined city is depicted. In most cases, the lowest PBP is achieved with the maximum collectors' surface studied ($A_{col} = 49.62 \text{ m}^2$) and the lowest volume of the storage tank ($V_{st} = 200 \text{ lt}$). In the city of Athens, the best combination for the minimization of PBP is proven to acquire the maximum number of PVT modules and a storage tank's volume equal to $V_{st} = 300 \text{ lt}$ for R134a, R152a, R1234yf and R1234ze. In Larnaca, the best combination for all refrigerants, except for Propylene, is the maximum number of PVT modules and a solar storage tank with volume capacity equal to $V_{st} = 300 \text{ lt}$.

The fact that the minimization of the PBP demands the highest collectors' surface and the lowest storage tank capacity was expected as elaborated before.

As expected, R152a has the lowest value of PBP with Propane and Propylene following as they have the best combination of price market and net electric efficiency, while R227ea and R1234yf have the highest values of PBP due to their high market price.

In Figures 5.15 – 5.19 the PBP of standalone PV operation is shown in order to compare with the coupling of the PVT-ORC system. It is apparent, that this value is much lower than those with the addition of the ORC. Thus, it can be concluded that the use of PVT modules as the hot stream for the evaporator of an ORC is not an economically viable solution given that it utilizes on waste heat of maximum temperature equal to $T_{hs,max} = 80^\circ\text{C}$ with an approximate net electrical efficiency $n_{el,net,ORC} \cong 6\%$.

The PBP values show a similar trend with the NPV as they are mainly dependent on the electricity price of the consumers. Thus, the lowest PBP values are observed in Larnaca and the highest ones in Athens, as elaborated in subchapter 5.2.

In Figure 5.20 the PBP values of R152a are shown if the system is used for non-household applications and thus the electricity price is taken equal to the second column of Table 5.2. From this figure, it can be concluded that the price of the produced electricity is a main variable for the payback period of the application and thus the selection of the location of the system should be

examined thoroughly. In the case of Athens and Madrid, an upper limit of $PBP = 100$ years was decided as a higher PBP is not worth calculating.

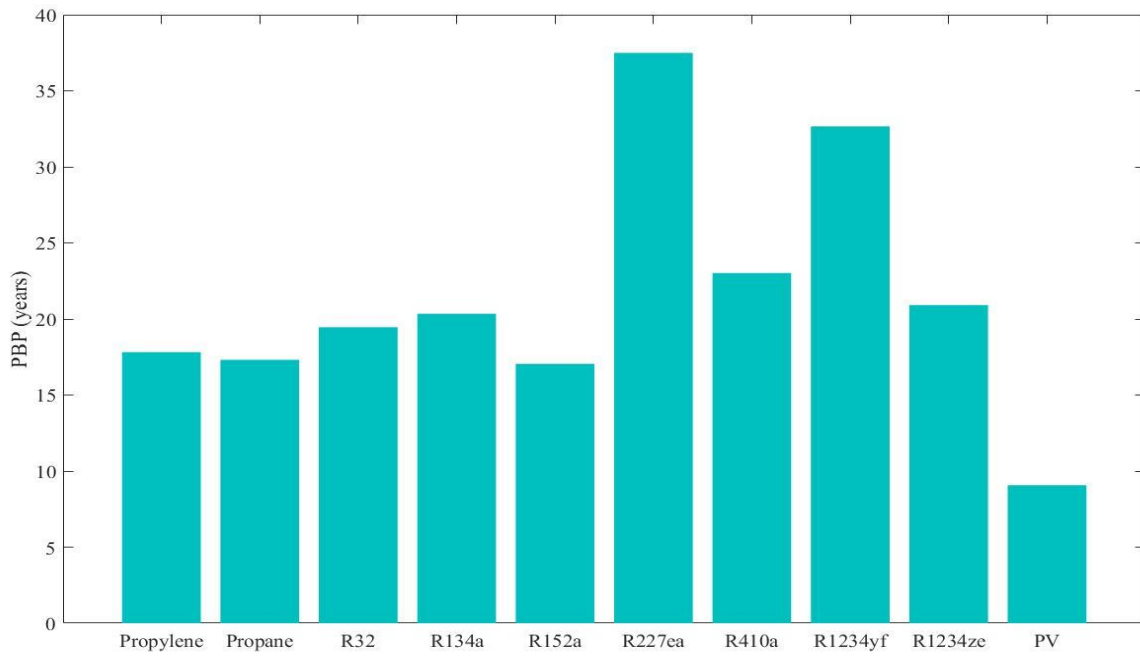


Figure 5.15 PBP of the examined working fluids and PV standalone operation in Athens

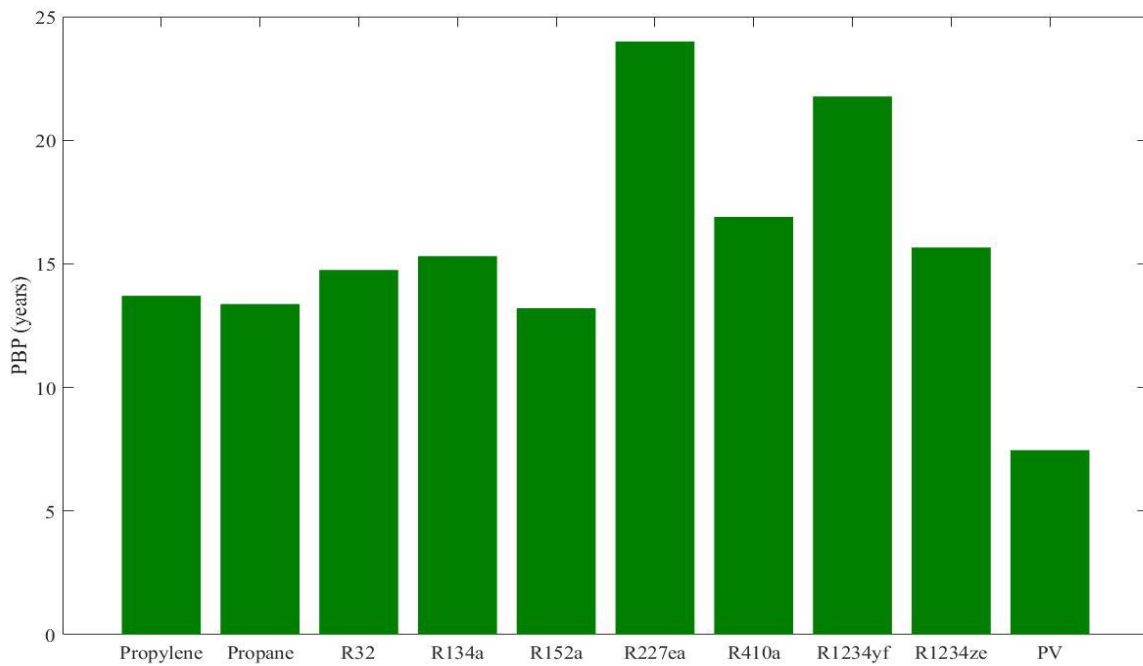


Figure 5.16 PBP of the examined working fluids and PV standalone operation in Naples

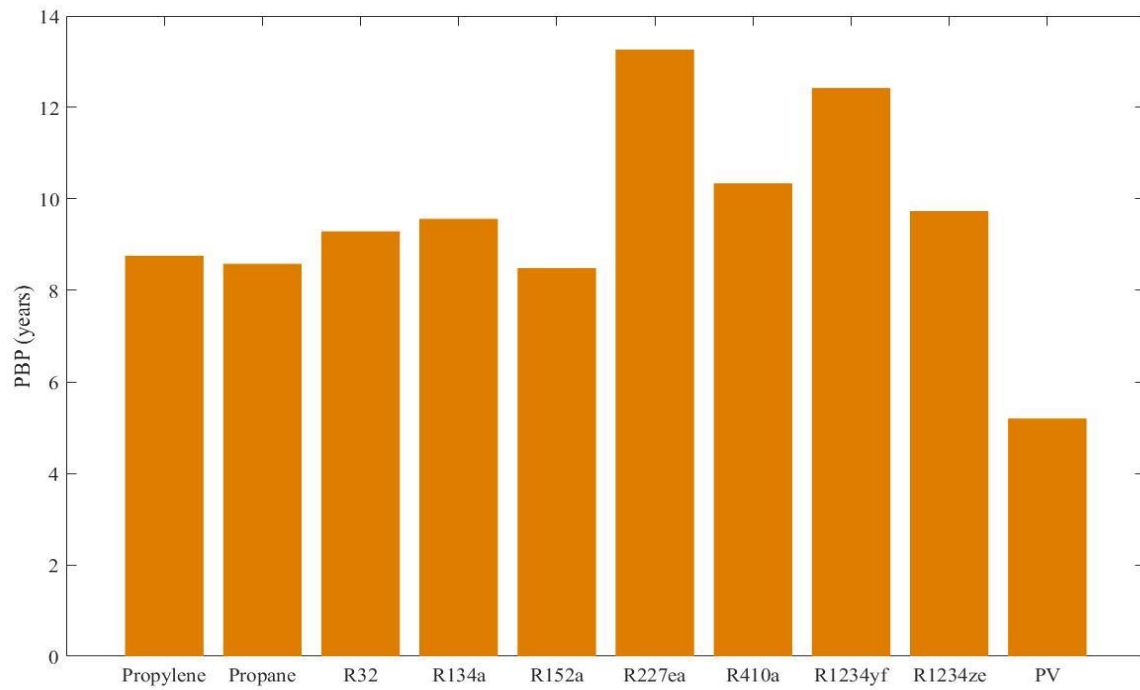


Figure 5.17 PBP of the examined working fluids and PV standalone operation in Larnaca

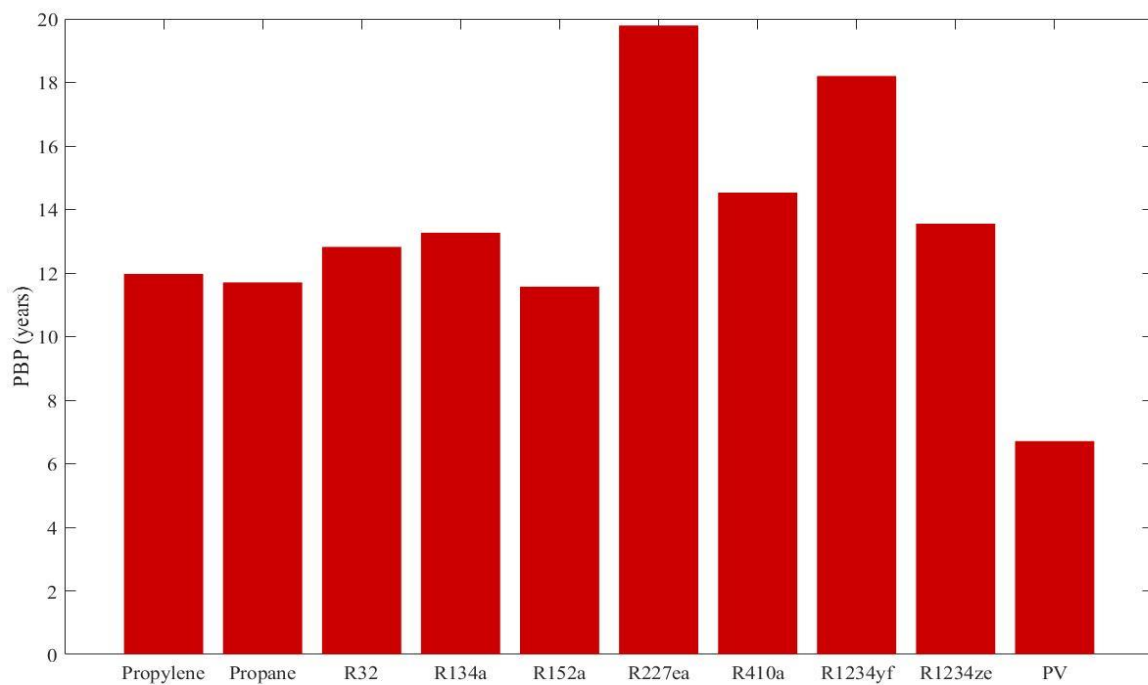


Figure 5.18 PBP of the examined working fluids and PV standalone operation in Madrid

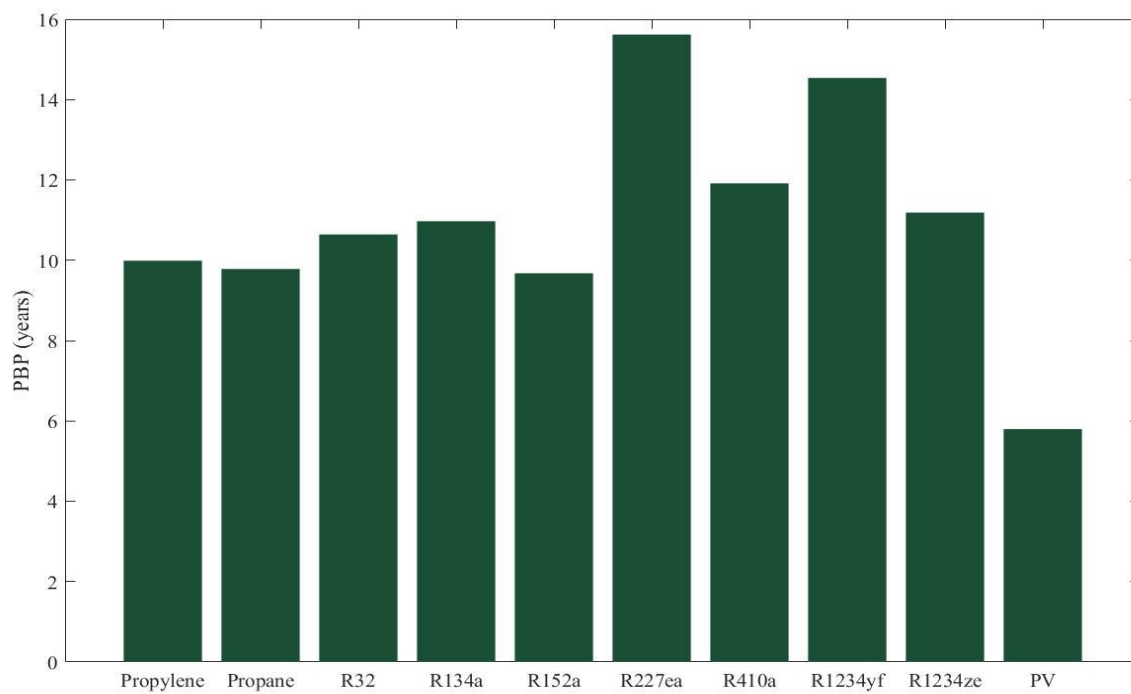


Figure 5.19 *PBP of the examined working fluids and PV standalone operation in Lisbon*

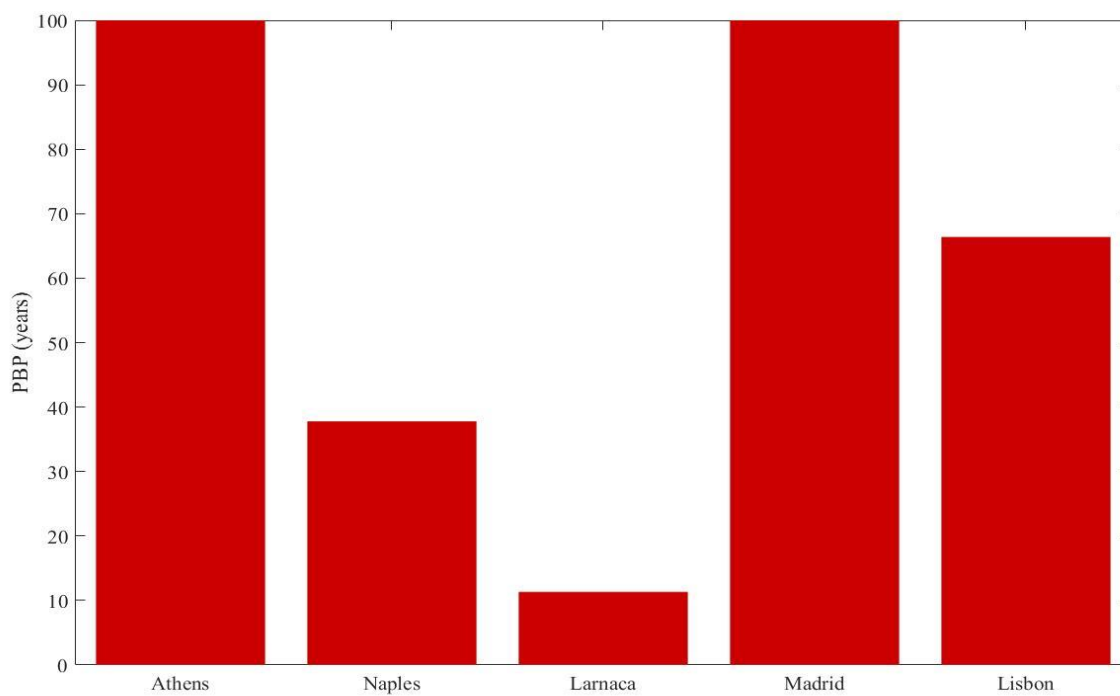


Figure 5.20 *PBP of R152a in each examined city for non-household consumers*

Chapter 6. Conclusion

In the present study the coupling of an ORC with PVT collectors is presented. A wide range of working fluids are examined as potential candidates of the cycle with a critical temperature around the maximum value of the thermal collectors $T_{hs,max} = 80^{\circ}\text{C}$.

The electric production of the PV modules is calculated for 5 different Mediterranean locations, which are Athens, Greece, Naples, Italy, Larnaca, Cyprus, Madrid, Spain and Lisbon, Portugal. For this purpose, annual meteorological data are used in order to calculate the cell temperature of the modules as well as their optimal tilt angle for maximizing the annual incline solar radiation. The highest annual PV electricity production is observed in the city of Larnaca with an annual energy production equal to $E_{el,net,PV} = 380.388 \text{ kWh/m}^2\text{y}$. Nevertheless, the efficiency of the thermal modules is pretty low and as a result the heat content of its working fluid is limited.

After the modeling of its components, the on-design simulation of the ORC is computed in order to maximize the net electric efficiency. The cost of the cycle for all examined working fluids is calculated based on the sizing of its components. As the heat source of the evaporator is not steady, the performance of the ORC in off-design conditions is essential to be thoroughly examined. The most promising working fluid, as far as its cost and efficiency is concerned, is R152a with a net electric efficiency in on-design conditions equal to $\eta_{net,el,ORC} = 6.931\%$ and in off-design conditions with $T_{hs,min} = 65^{\circ}\text{C}$ equal to $\eta_{net,el,ORC} = 5.223\%$. The cost of the cycle with R152a as the working fluid is estimated to be equal to $C_{tot,ORC} = 7167.06 \text{ €}$. The two examined hydrocarbons, Propylene and Propane, are the next most viable choices, but due to their flammability, extra safety measurements should be considered.

The annual net electricity production of the ORC mainly depends on the collectors' surface and the volume of the solar storage tank. The maximization of the ORC's production requires the highest number of PVT modules examined as well as the maximum volume capacity of the storage tank. The annual exergy and energy efficiency of the system are relatively high (in the city of Athens with R152a as the working fluid $\eta_{ex,sys} = 20.598\%$ and $\eta_{el,net,sys} = 19.543\%$) due to the high efficiency of the PV modules. This result is similar to the examined PVT-ORC configuration by Tourkov et al. [37], where with an evaporation temperature of $T_{evap} = 80^{\circ}\text{C}$, R11 as the working fluid and CdS PV cells, the energy efficiency of the system was equal to $\eta_{el,net,sys} \cong 24\%$. Furthermore, Rahbar et al. [39] examined the coupling of CPV/T-ORC system with water and nanofluid as its working fluid and the system efficiency was calculated equal to $\eta_{el,net,sys} = 17.79\%$ and $\eta_{el,net,sys} = 20.5\%$ respectively.

In order to evaluate the economic viability of the application, a few investment performance indexes are examined. For this purpose, the investment cost of the system is calculated. The most financially promising scenario requires the maximum number of PVT modules and one of the two smallest examined storage tanks. In the city of Athens, with R152a as the working fluid, the lowest Levelized Cost of Energy is equal to 0.153 €/kWh , the highest Net Present Value is equal to 2244.22 € and the minimum Payback Period is equal to 17.05 years , when the

electricity cost of the household consumers is equal to 0.1646 €/kWh. According to Kosmadakis et al. [38] the respective performance indexes for a CPV-ORC system are equal to $LCOE = 0.113 \text{ €/kWh}$, $NPV \cong 4280 \text{ €}$ and $PBP = 14 \text{ years}$ when the electricity cost of the consumers is equal to 0.15 €/kWh and the expected lifetime of the system is set to be 20 years. In the above study, R245fa was the examined working fluid and the on-design thermal efficiency of the cycle was equal to $\eta_{th,ORC} = 10.742\%$ while in this diploma thesis the thermal efficiency of the cycle in the case of R152a is equal to $\eta_{th,ORC} = 8.817\%$. Thus, the results of both studies are similar, although the PVT-ORC system appears to be a less profitable technology.

The performance indexes are calculated in the case of standalone PVT operation. In the city of Athens, their values are estimated to be equal to $LCOE = 0.1062 \text{ €/kWh}$, $NPV \cong 11164 \text{ €}$ and $PBP = 9.07 \text{ years}$. These values are a lot more promising than the case of the coupling of PVT-ORC with R152a as the working fluid. This difference indicates that the utilization of the heat produced by the thermal collectors by an ORC, in order to increase the electricity production, is not economically sustainable. Thus, the use of this heat content as hot water for the household is preferred instead of the increased electricity production by the ORC.

This study could be further investigated in the future in the following ways:

- More locations can be examined outside of the Mediterranean region with less solar irradiance but higher electricity prices.
- A solar tracking system can be added on the PVT modules in order to increase the annual energy yield.
- Instead of water/glycol mix as the working fluid of the thermal collectors, a nanofluid based system may lead into more promising results.
- Concentrating PVT systems may result into higher electricity production as the cycle's temperature and pressure limits will be increased.
- The examined collectors' surface can be increased in order to examine the ORC's electricity production in the case of industries. Nonetheless, in this case the electricity price of non-household consumers should be applied.
- A sensitivity analysis regarding the cost of the ORC components, the PVT modules, the market price of the working fluids as well as the electricity price should be conducted.

References

1. IEA, *Global Energy & CO 2 Status Report 2017*. 2018.
2. Mathioudakis, K., *Operation of Gas and Steam Turbines*. 2007, Athens.
3. Vundela Siva Reddy, S.K.T., Subhash Chandra Kaushik, N. L. Panwar, *An Approach to Analyse Energy and Exergy Analysis of Thermal Power Plants: A Review*. Smart Grid and Renewable Energy, 2010.
4. Tchanche, B.F., G. Lambrinos, A. Frangoudakis, G. Papadakis, *Low-grade heat conversion into power using organic Rankine cycles - A review of various applications*. Renewable and Sustainable Energy Reviews, 2011. **15**(8): p. 3963-3979.
5. K. Braimakis, T.C.R., A.D. Leontaritis, S. Karellas, *Comparison of Environmentally Friendly Working Fluids for Organic Rankine Cycles*, in *Advances in New Heat Transfer Fluids*, A.A. Minea, Editor. 2017. p. 377-426.
6. Quoilin, S., M. V. D. Broek, S. N. Declaye, P. Dewallef, and V. Lemort, *Techno-economic survey of Organic Rankine Cycle (ORC) systems*. Renewable and Sustainable Energy Reviews, 2013. **22**: p. 168-186.
7. Quoilin, S., S. Declaye, B. F. Tchanche, and V. Lemort, *Thermo-economic optimization of waste heat recovery Organic Rankine Cycles*. Applied Thermal Engineering 2011. **31**(14-15): p. 2885-2893.
8. IEA, *Solar heat worldwide International Energy Agency Solar Heating & Cooling Programme*. 2016.
9. IEA, *Technology Roadmap-Solar photovoltaic energy*. 2010.
10. G.K., S., *Solar Power Generation by PV (Photovoltaic) Technology: A Review*. Energy, 2013. **53**: p. 1-13.
11. Sopian K., Y.K., Liu HT, Kakaç S., Verizoglu TN, *Performance analysis of photovoltaic thermal air heaters*. Energy Conversion and Management, 1996. **37**(11): p. 1657-1670.
12. Ullah, K.R., R. Saidur, H. W. Ping, R. K. Akikur, N. H. Shuvo, *A Review of Solar Thermal Refrigeration and Cooling Methods*. Renewable and Sustainable Energy Reviews, 2013. **24**: p. 499-513.
13. SynergyEnviroEngineers. Available from: <http://www.synergyenviron.com/resources/solar-photovoltaic-systems>.
14. Tyagi V. V., N.A.A.R., Jeyraj A. L. Selvaraj, *Progress in Solar PV Technology: Research and Achievement*. Renewable and Sustainable Energy Reviews, 2013. **20**(Supplement C): p. 443-461.
15. Deb, S.K., *Recent Developments in High Efficiency Photovoltaic Cells*. Renewable Energy, 1998. **15**(1-4): p. 467-472.
16. El Chaar, L., L. A. Iamont, N. El Zein, *Review of Photovoltaic Technologies*. Renewable and Sustainable Energy Reviews, 2011. **15**(5): p. 2165-2175.
17. Goetzberger Adolf, C.H., Hans-Werner Schock, *Photovoltaic Materials, History, Status and Outlook*. Materials Science and Engineering: R Reports, 2003. **40**(1): p. 1-46.
18. Gorter T., A.H.M.E.R., *A Comparison of 15 Polymers for Application in Photovoltaic Modules in PV-Powered Boats*. Applied Energy, 2012. **92**(Supplement C): p. 286-297.
19. Gong Jiawei, K.S., Qiquan Qiao, Zhengping Zhou, *Review on Dye-Sensitized Solar Cells (DSSCs): Advanced Techniques and Research Trends*. Renewable and Sustainable Energy Reviews, 2017. **68**(Part 1): p. 234-246.

20. Lamnatou C., C.D., *Photovoltaic/Thermal (PVT) Systems: A Review with Emphasis on Environmental Issues*. Renewable Energy, 2017. **105**(Supplement C): p. 270-287.
21. Brahim Taoufik, A.J., *Economical Assessment and Applications of Photovoltaic/Thermal Hybrid Solar Technology: A Review*. Solar Energy, 2017. **153**(Supplement C): p. 540-561.
22. Zondag, H., *The yield of different combined PV-thermal collector designs*. Solar Energy, 2003. **74**(253-269).
23. Parida B., I.S., Goic R., *A review of solar photovoltaic technologies*. Renewable and Sustainable Energy Reviews, 2011. **15**(1625-1636).
24. Michael J., I.S., Goic R., *Flat plate solar photovoltaic-thermal (PV/T) systems: a reference guide*. Renewable and Sustainable Energy Reviews, 2015. **51**: p. 62-88.
25. Ceylan Ilhan, G.A.E., Ergün Alper, Tabak Abdulsamed, *Performance analysis of a concentrated photovoltaic and thermal system*. Renewable Energy, 2016. **72**: p. 79-87.
26. Jinshun Wu, X.Z., Jingchun Shen, Yupeng Wu, Karen Connelly, Tong Yang, Llewellyn Tang, Manxuan Xiao, Yixuan Wei, Ke Jiang, Chao Chen, Peng Xu, Hong Wang, *A review of thermal absorbers and their integration methods for the combined solar photovoltaic/thermal (PV/T) modules*. Renewable and Sustainable Energy Reviews, 2017. **75**: p. 839-854.
27. Chow TT, H.W., Ji J., *Hybrid photovoltaic-thermosyphon water heating system for residential application*. Solar Energy, 2006. **80**: p. 298-306.
28. Zhou Jinzhi, Z.X., Ma Xiaoli, et al., *Experimental investigation of a solar driven direct-expansion heat pump system employing the novel PV/micro-channels-evaporator modules*. Applied Energy, 2016. **178**: p. 484-495.
29. Zhang Xingxing, Z.X., Shen Jingchun, Hu Xi, Liu Xuezhi, Xu Jihuan, *Design, fabrication and experimental study of a solar photovoltaic/loop-heat-pipe based heat pump system*. Solar Energy, 2013. **97**: p. 551-568.
30. Jin GL., I.A., Chean YK, Daghigh R., Ruslan H., Mat S, et al, *Evaluation of single-pass photovoltaic-thermal air collector with rectangle tunnel absorber*. American Journal of Applied Sciences, 2010. **7**(2): p. 277-282.
31. Chow TT, P.G., Fong KF, Lin Z., Chan ALS, Ji J., *Energy and exergy analysis of photovoltaic-thermal collector with and without glass cover*. Applied Energy, 2009. **86**: p. 310-316.
32. Jing D., H.Y., Liu M., Wei J., Guo L., *Preparation of highly dispersed nanofluid and CFD study of its utilization in a concentrating PV/T system*. Solar Energy, 2015. **112**: p. 30-40.
33. Ghadiri M., S.M., Pasandixleh-fard M., Moghadam A.J., *Experimental investigation of a PVT system performance using nano ferrofluids*. Energy Conversion and Management, 2015. **103**: p. 468-476.
34. Chow TT, H.W., Ji J., *An experimental study of facade-integrated photovoltaic/water heating system*. Applied Thermal Engineering, 2007. **27**(1): p. 37-45.
35. Athienitis AK, B.J., O'Neill B., Faille J., *A prototype photovoltaic/thermal system integrated with transpired collector*. Solar Energy, 2011. **85**: p. 139-153.
36. Pedro M. L. P. Magalhães, J.F.A.M., António L. M. Joyce, *Comparative analysis of overheating prevention and stagnation handling measures for photovoltaic-thermal (PV-T) systems*. Energy Procedia, 2016. **91**: p. 346-355.
37. Konstantin Tourkov, L.S., *Performance evaluation of a PVT/ORC (photovoltaic thermal/organic Rankine cycle) system with optimization of the ORC and evaluation of several PV (photovoltaic) materials*. Energy, 2015. **82**: p. 839-849.

38. G. Kosmadakis, D.M., G. Papadakis, *Simulation and economic analysis of a CPV/thermal system coupled with an Organic Rankine cycle for increased power generation*. Solar Energy, 2010. **85**: p. 308-324.
39. Kiyarash Rahbar, A.R., Hamed Khatam Bolouri Sangjoei, Nima Razmjoo, *Heat recovery of nano-fluid based concentrating Photovoltaic Thermal (CPV/T) Collector with Organic Rankine Cycle*. Energy Conversion and Management, 2019. **179**: p. 373-396.
40. Agustín M. Delgado-Torres , L.G.-R., *Analysis and optimization of the low-temperature solar organic Rankine cycle (ORC)*. Energy Conversion and Management, 2009. **51**: p. 2846-2856.
41. Michaël Marion, I.V., Anne-Lise Tiffonnet, *Study and optimization of a solar subcritical organic Rankine cycle*. Renewable Energy, 2012. **48**: p. 100-109.
42. Wang, J., L. Zhao, and X. Wang, *A comparative study of pure and zeotropic mixtures in low-temperature solar Rankine cycle*. Applied Energy, 2010. **87**(11): p. 3366-3373.
43. Habbati Bellia, R.Y., Moulay Fatima, *A detailed modeling of photovoltaic module using MATLAB*. NRIAG Journal of Astronomy and Geophysics, 2014. **3**: p. 53-61.
44. Faïman, D., *Assessing the outdoor operating temperature of photovoltaic modules*. Progress in Photovoltaics: Research and Applications, 2008. **16**(4): p. 307-315.
45. Elena Barykina, A.H., *Modeling of photovoltaic module temperature using Faïman model: Sensitivity analysis for different climates*. Solar Energy, 2017. **146**: p. 401-416.
46. Bouraiou A., H.M., Chaker A., Sadok M., Mostefaoui M., Lachtar S., *Modeling and Simulation of Photovoltaic Module and Array Based on One and Two Diode Model Using Matlab/Simulink*. Energy Procedia, 2015. **74**: p. 864-877.
47. DualSun. Available from: <https://academy.dualsun.com/wp-content/uploads/DualSun-EN-Datasheet-Spring.pdf>.
48. Roumpedakis, T., *Techno-economic investigations of a solar driven ORC-sorption system for combined cooling, heating and power*. 2018, TU Delft.
49. Ter-Gazarian, A., *Energy Storage for Power Systems*. Institution of Engineering and Technology, 2011.
50. Wischhusen, S., *An enhanced discretization method for storage tank models within energy systems*, in *Proc. of the 5-th International Modelica Conference*. 2006.
51. Bellos, E., Tzivanidis, C., Symeou, C., and Antonopoulos, K.A., *Energetic, exergetic and financial evaluation of a solar driven absorption chiller – A dynamic approach*. Energy Conversion and Management, 2017. **137**: p. 34-48.
52. Furbo, J.F.a.S., *Thermal stratification in a hot water tank established by heat loss from the tank*. Solar Energy, 2012. **86**(11): p. 3460-3469.
53. Rahman A., S.A.D., Fumo N., *Performance modeling and parametric study of a stratified water thermal storage tank*. Applied Thermal Engineering, 2016. **100**: p. 668-679.
54. S.G., D.V.D.a.K., *Correlating evaporation heat transfer coefficient of refrigerant R-134a in a plate heat exchanger.*, in *Engineering Foundation Conference on Pool and Flow Boiling*. 2000: Alaska.
55. Focke W.W., Z.J., Olivier I., *The effect of the corrugation inclination angle on the thermohydraulic performance of plate heat exchangers*. International Journal of Heat and Mass Transfer, 1985. **28**(8): p. 1469-1479.
56. Y.Y.Yan, T.F.L., *Evaporation Heat Transfer and Pressure Drop of Refrigerant R-134a in a Plate Heat Exchanger*. Journal of Heat Transfer, 1999. **121**(1): p. 118-127.

57. Lin, Y.Y.H.a.T.F., *Saturated flow boiling heat transfer and pressure drop of refrigerant R-410A in a vertical plate heat exchanger*. International Journal of Heat and Mass Transfer, 2002. **45**(5): p. 1033-1044.
58. Thonon B., B.A., *Condensation of Pure and Mixture of Hydrocarbons in a Compact Heat Exchanger: Experiments and Modelling*. Heat Transfer Engineering, 2002. **23**(6): p. 3-17.
59. Yan Y.Y., L.H.C.a.L.T.F., *Condensation heat transfer and pressure drop of refrigerant R-134a in a plate heat exchanger*. International Journal of Heat and Mass Transfer, 1999. **42**(6): p. 993-1006.
60. Laval, A.; Available from: <http://www.industrial-gp.ro/media/1534418/ac30eq--ach30eq.pdf>.
61. Lemort V., D.S., Quoilin S., *Experimental characterization of a hermetic scroll expander for use in a micro-scale Rankine cycle*. Proceedings of the Institution of Mechanical Engineers, Part A: Journal of Power and Energy, 2012. **226**(1): p. 126-136.
62. Dumont O., D.R., Lemort V., *Experimental investigation of four volumetric expanders*. Energy Procedia, 2017. **129**: p. 859-866.
63. Ziviani D., G.S., Lecompte S., Groll E.A., Braun J.E., Horton W.T., van den Broek M., De Paepe M., *Characterizing the performance of a single-screw expander in a small-scale organic Rankine cycle for waste heat recovery*. Applied Energy, 2016. **181**(155-170).
64. Laval, A. CB30 Technical characteristics. Available from: <https://www.alfalaval.com/globalassets/documents/microsites/heating-and-cooling-hub/pd-leaflets/cb30.pdf>.
65. Engineering, W.; Available from: <http://www.hydra-cell.com/product/D10-hydracell-pump.html>.
66. Cost of Propylene. Available from: <https://www.gas-uk.co.uk/rent-free-gas-cylinders/refrigerant-gases>.
67. Cost of Propane. Available from: <https://www.boconline.co.uk/shop/en/uk/gas-a-z/propane/propane-cylinder>.
68. Cost of R32. Available from: <http://www.eurorefrigerant.com/15-r32-refrigerant-gas-cylinders-daikin-panasonic>.
69. Cost of R152a. Available from: <http://www.igsd.org/wp-content/uploads/2016/07/SL-MAC-18-July-as-Delivered1.pdf>.
70. BoconOnline. Available from: <https://www.boconline.co.uk/en/index.html>.
71. Cost of R410a. Available from: <http://www.eurorefrigerant.com/7-r410a-r410-refrigerant-gas-cylinders>.
72. Cost of R-C318. Available from: <http://www.synquestlabs.com/product/id/23250.html>.
73. Cost of R1234yf. Available from: <http://www.eurorefrigerant.com/17-r1234yf-refrigerant-gas-cylinders-honeywell>.
74. Cost of R1234ze. Available from: https://ec.europa.eu/clima/sites/clima/files/f-gas/legislation/docs/aerosols_foams_en.pdf.
75. Zilmet. Available from: <https://zilmet.it/en/>.
76. Lecompte, S., Huisseune, H., van den Broek, M., De Schampheleire, S., and De Paepe, M., *Part load based thermo-economic optimization of the Organic Rankine Cycle (ORC) applied to a combined heat and power (CHP) system*. Applied Energy, 2013. **111**: p. 871-881.
77. Boyaghchi, F.A., and Heidarnajad, P., *Thermoeconomic assessment and multi objective optimization of a solar micro CCHP based on Organic Rankine Cycle for domestic application*. Energy Conversion and Management, 2015. **97**: p. 224-234.

78. Email, A.; Available from: https://www.austria-email.com/fileadmin/content-en/Products/Buffer_Tanks/Pufferspeicher_240_810_engl.pdf.
79. Kalogirou, S.A., Karellas, S., Braimakis, K., Stanciu, C., and Badescu, V., *Exergy analysis of solar thermal collectors and processes*. Progress in Energy and Combustion Science, 2016. **56**: p. 106-137.
80. Cerbos, O. *Storage Tanks*. 2018; Available from: <https://www.cerbos.ee/en/20-storage-tanks>.
81. Eurostat. *Electricity Price Statistics*. 2018; Available from: https://ec.europa.eu/eurostat/statistics-explained/index.php/Electricity_price_statistics.
82. Zervos, A., *Renewable Energy*. 2014, Athens: National Technical University of Athens.